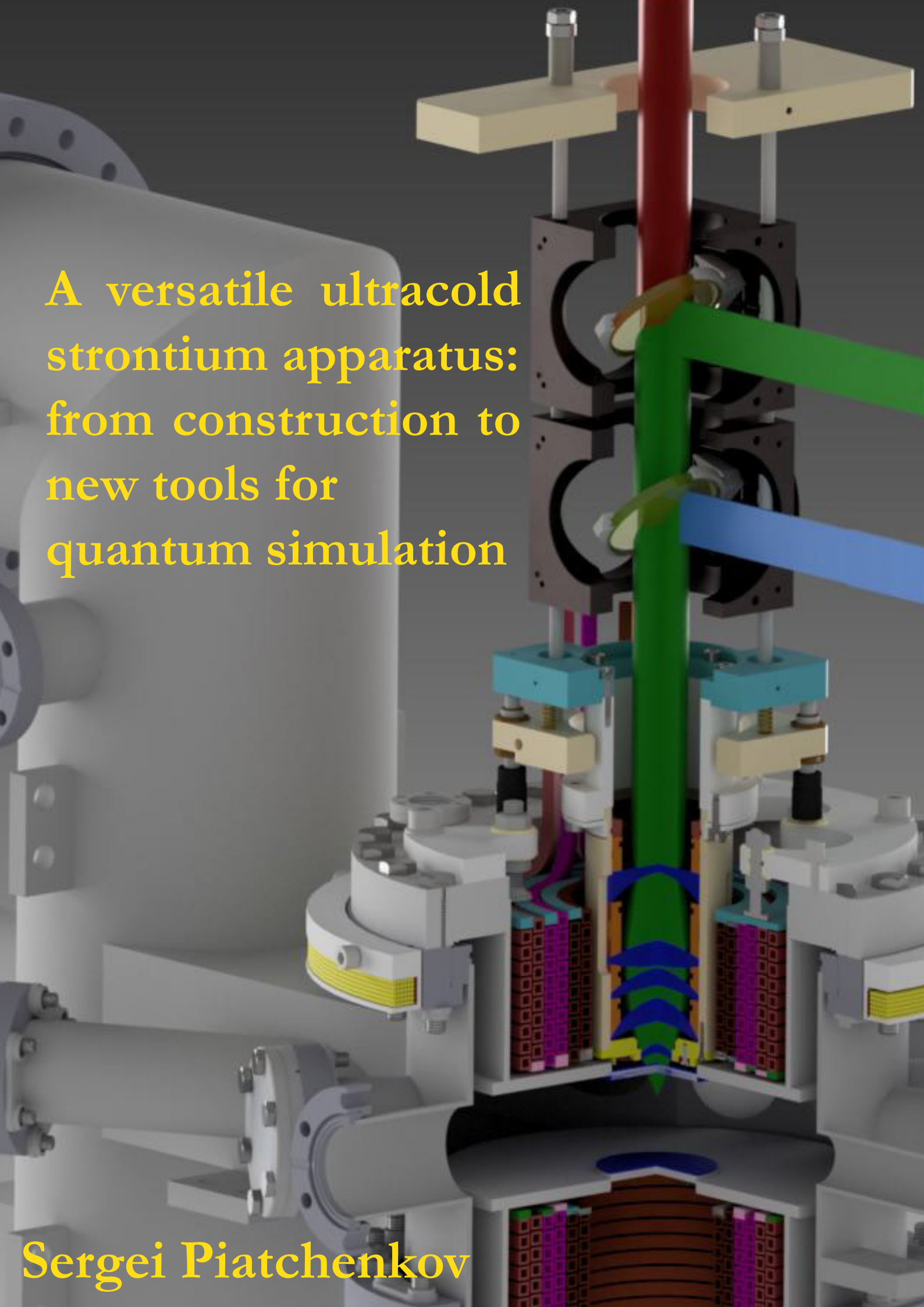


A versatile ultracold strontium apparatus:  
from construction to  
new tools for  
quantum simulation

Sergei Piatchenkov



---

**A versatile ultracold strontium apparatus:  
from construction to new tools for quantum  
simulation**

---

ACADEMISCH PROEFSCHRIFT

ter verkrijging van de graad van doctor  
aan de Universiteit van Amsterdam  
op gezag van de Rector Magnificus  
prof. dr. ir. K. I. J. Maex

ten overstaan van een door het College voor Promoties ingestelde  
commissie, in het openbaar te verdedigen in de Agnietenkapel  
op donderdag 4 juni 2020, te 14:00 uur

door

**Sergei Piatchenkov**

geboren te Smolensk

**Promotiecommissie:**

Promotor:	prof. dr. F. E. Schreck	Universiteit van Amsterdam
Co-promotor:	dr. G. Siviloglou	Universiteit van Amsterdam
Overige leden:	dr. N. Poli	University of Florence
	prof. dr. K. J. Boller	University of Twente
	prof. dr. M. S. Golden	Universiteit van Amsterdam
	dr. C. J. M. Coulais	Universiteit van Amsterdam
	prof. dr. H. B. van Linden	
	van den Heuvel	Universiteit van Amsterdam

Faculteit der Natuurwetenschappen, Wiskunde en Informatica (FNWI)

© 2019 Sergei Piatchenkov.

The author can be reached at:  
pjatchenkov@gmail.com

The research reported in this thesis was carried out at the Van der Waals-Zeeman Institute, Institute of Physics, University of Amsterdam. This work was financially supported by the European Research Council (ERC) under Project No. 615117 QuantStro, by the Netherlands Organisation for Scientific Research (NWO) through Gravitation grant No. 024.003.037, Quantum Software Consortium.

# Contents

<b>1</b>	<b>Introduction</b>	<b>1</b>
<b>2</b>	<b>Experimental setup</b>	<b>6</b>
2.1	Vacuum system . . . . .	6
2.1.1	Source section . . . . .	7
2.1.2	UHV section . . . . .	15
2.1.3	Slower viewport . . . . .	21
2.2	Attaining the UHV regime . . . . .	23
2.2.1	Vacuum pumps . . . . .	24
2.2.2	Sources of gas particles in a vacuum system . . . . .	28
2.2.3	Baking of the new strontium apparatus . . . . .	32
2.3	Laser systems . . . . .	38
2.3.1	Blue laser system . . . . .	39
2.3.2	Green laser system . . . . .	46
2.3.3	Red laser system . . . . .	49
2.3.4	Infrared laser system . . . . .	53
2.4	Magnetic field control . . . . .	54
<b>3</b>	<b>Obtaining quantum degenerate gases</b>	<b>62</b>
3.1	Transverse cooling . . . . .	62
3.2	Zeeman slowing . . . . .	64
3.3	Magneto-optical traps . . . . .	65
3.3.1	Blue MOT . . . . .	65
3.3.2	Red MOT . . . . .	67
3.3.3	Fermionic rMOT . . . . .	73
3.4	Dipole trap . . . . .	77
3.5	Bose-Einstein condensation of $^{84}\text{Sr}$ . . . . .	82
3.6	Degenerate Fermi gas of $^{87}\text{Sr}$ . . . . .	86

<b>4</b>	<b>The frequency of the <math>^1S_0 - ^3P_2</math> transition in <math>^{87}\text{Sr}</math></b>	<b>91</b>
4.1	Introduction . . . . .	91
4.2	Experimental details . . . . .	93
4.2.1	$^1S_0 - ^3P_2$ spectroscopy laser setup . . . . .	93
4.2.2	Iodine spectroscopy setup . . . . .	93
4.2.3	Strontium sample preparation and spectroscopy principle . . . . .	95
4.3	Determination of the $^1S_0 - ^3P_2$ transition frequency . . . . .	96
4.3.1	Coarse, indirect determination . . . . .	96
4.3.2	Precise, direct determination . . . . .	98
4.3.3	Error analysis . . . . .	102
4.4	Conclusion . . . . .	104
<b>5</b>	<b>Towards quantum gas microscopy</b>	<b>105</b>
<b>6</b>	<b>Outlook</b>	<b>114</b>
<b>7</b>	<b>Summary</b>	<b>117</b>
	<b>Samenvatting</b>	<b>120</b>
	<b>List of publications</b>	<b>121</b>
	<b>Acknowledgments</b>	<b>124</b>
	<b>Bibliography</b>	<b>125</b>

*To my parents,  
Valentina and Vasiliy*



# Chapter 1

## Introduction

Over the last 25 years ultracold quantum gases became an outstanding platform to investigate a broad spectrum of questions about quantum physics, ranging from atomic, molecular and optical physics to solid-state physics, nuclear physics and astrophysics, to name but a few. One of the most important choices to make before constructing a new quantum gas experiment is the selection of an atomic species or mixture of species, the unique properties of which will determine the variety of open questions one can address. The list of species brought to quantum degeneracy is constantly growing, enriching the experimental toolbox with new opportunities.

Strontium joined the family of atoms cooled down to quantum degeneracy with the achievement of the first strontium BECs in 2009 [1, 2] and degenerate Fermi gases in 2010 [3, 4]. Strontium stands out from other elements cooled to degeneracy by several important features, which are highly valuable for applications, such as clocks or atom interferometers, and for implementing a variety of intriguing theoretical proposals [5]. It is an alkaline-earth element with two valence electrons and four stable isotopes: bosonic  $^{84}\text{Sr}$ ,  $^{86}\text{Sr}$ ,  $^{88}\text{Sr}$  and fermionic  $^{87}\text{Sr}$ . The bosonic isotopes do not have a nuclear spin, leading to a simplified energy level structure, while the fermionic isotope has the largest nuclear spin among the alkaline-earth elements,  $I = 9/2$ , leading to richer structure due to hyperfine splitting of each level.

The presence of two electrons in the outer electronic shell results in the differentiation of energy levels into singlets and triplets. Transitions from the ground state ( $^1S_0$ ) to the first excited singlet or triplet state ( $^1P_1$  or  $^3P_{0,1,2}$ ) have contrasting properties, therefore they enable different approaches to atom manipulation, especially to cooling and trapping. The  $^1S_0 - ^1P_1$  transition has a linewidth of 32 MHz, leading to a maximally achievable deceleration of  $\sim 10^5 \times g$ , well suited for transverse cooling, Zeeman slowing, capturing atoms in a magneto-optical trap and cooling

to about 1 mK [6]. By contrast the  $^1S_0 - ^3P_1$  intercombination transition between a singlet and a triplet state has a linewidth of 7.4 kHz, leading to a maximal deceleration of only  $\sim 16 \times g$ , which is insufficient to slow atoms emanating from an oven, but is sufficient to cool a milli-Kelvin cloud of atoms to the micro-Kelvin regime. This final temperature is on the order of the very low Doppler temperature,  $T_{\text{Doppler}} = 180 \text{ nK}$  [7]. Furthermore the  $^1S_0 - ^3P_{0,2}$  intercombination transitions have linewidths of  $\sim 1 \text{ MHz}$  for fermionic Sr and even less for bosonic Sr. Very early on strontium caught the attention of researchers from the metrology community due to its  $^1S_0 - ^3P_0$  transition with ultranarrow linewidth and small Zeeman shift, highly appreciated features when building precise frequency standards. Using ultranarrow transitions became also one of the promising elements to implement proposals from the rapidly growing field of quantum simulation [8].

The idea of quantum simulation is to mimic the Hamiltonian of a complicated, hard to control or analyze quantum system using an easily-controlled analogous physical system [9–11]. Simulations particularly interesting to our group are related to questions in condensed matter physics that are difficult to solve with classical approaches. The benefits of using a platform of ultracold atoms for simulations come from several crucial capabilities, for example to reproduce the lattice environment that electrons experience in the solid state [12]; to achieve the regime of strong interactions with Feshbach resonances [13], Rydberg states [14] or dipolar interactions [15]; to generate artificial gauge fields, imitating the influence of external magnetic and electric fields on charged particles [16, 17], and even to operate at the level of a single atom [18, 19]. Peculiar many-body phenomena can be studied with ultracold atoms, for instance  $SU(N)$  magnetism, allowing to reach  $N$  as large as 10 [20, 21]; Kondo physics, exploiting internal state dependent optical lattices [22] or the quantum Hall effect, using optical flux lattices to create the required magnetic field [23, 24].

Ultracold gases are also a promising platform to realize protocols for quantum computation [25–27]. Quantum computation is a research field merging scientific achievements with technological breakthroughs to enable a new type of computation, which can significantly outperform even the most powerful classical competitors for specific types of problems. An important benefit of ultracold atoms for this task is scalability. It is possible to create large arrays with more than a hundred individually localized atoms, to individually control and detect these atoms using high-NA microscope objectives and to engineer quantum states with high precision.

The unique properties of strontium allow it to become a promising species for

---

quantum simulations and computations. To pursue these intriguing directions new experimental ultracold Sr systems are constantly being built. In recent years we witnessed the construction of several new apparatuses to tackle a broad spectrum of physical problems, among them the goal to reach a continuous atom laser [28]; superradiant lasers [29]; control over individual atoms in optical tweezers [30–32]; a new generation of optical clocks [33]; many-body quantum physics in optical lattices [34]; atomtronics [35]; optical flux lattices [35] and more.

The main effort of this thesis is to construct a new ultracold Sr apparatus, with the primary goal to investigate questions in the field of quantum simulation. We narrowed our focus to several ambitious objectives, establishing a long-term strategy for our experiment.

The first objective is quantum gas microscopy [36–39], a recently developed technology characterized by sub-micron resolution allowing to image single sites of an optical lattice and to optically address individual atoms. Most of the microscopes developed so far work with alkali elements. A lot of activity is ongoing worldwide to extend this technique to other elements and even to molecules, which will bring new opportunities for research. Related to quantum gas microscopy is research exploiting optical tweezers, tightly focused laser beams that can form arrays of traps containing a single atom each. The recent successful implementation of this approach with alkaline-earth-metal-like atoms extended the range of experimental instruments, enriching the ultracold atom toolbox [30–32, 40]. In the short period since the creation of optical tweezers with strontium, they have proven to be a valuable tool for quantum-enhanced metrology [41, 42]. These new platforms provide a middle ground to build clocks, in between the high accuracy, low signal-to-noise ion clocks and the "low" accuracy, high signal-to-noise lattice clocks.

The second objective appealing to us is to immerse ultracold atoms in synthetic gauge fields. This objective merges concepts from optics, ultracold gases and condensed matter physics [43]. The complicated and interesting physics of the fractional quantum Hall effect is in reach to be reproduced using ultracold gases [24]. One example of interest to us are optical flux lattices [23, 44]. These lattices are generated by a specially tailored configuration of laser beams with properly chosen frequency detunings and polarizations to induce specific, spatially dependent atom-light couplings. The created optical flux lattice leads to an energy band structure that is characterized by a non-trivial topology of the bands. The concept of synthetic fields can be extended with the idea of synthetic dimensions. For example a four-dimensional lattice can be created, where three dimensions are defined by

an optical lattice in real space, while the fourth dimension, in the form of a finite sized lattice, is formed using the spin degree of freedom [45–47]. Also in this 4D lattice a synthetic gauge field can be produced by coupling the magnetic substates of the  $^{87}\text{Sr}$  ground states using Raman beams with carefully chosen parameters and geometry. This idea might allow to study quantum Hall physics in four-dimensions, targeting the exploration of new exotic topological phases and phenomena [48, 49].

The third objective interesting to us is to engineer long-range interactions by exciting atoms to states with large principal quantum number: Rydberg states. One of the promising platforms to implement quantum simulation and computation is based on the combination of an array of optical tweezers, filled with one atom each, and the ability to excite those atoms to Rydberg states. Rydberg atoms have unique properties significantly different from atoms in the ground state [50] and the one advantage we are interested in is their strong and long-range interaction, which can be more than ten orders of magnitude larger compared to the interaction between ground-state atoms [51]. An important concept related to these strong interactions is the dipole blockade, which enables the realization of quantum gates [51], the study of quantum magnetism [52], the construction of single-photon sources [53, 54], etc. The platform of optical tweezers stands out by several beneficial features, for instance the ability to generate an array of single atoms of arbitrary geometry [18, 55], sorting of atoms to produce defect free arrays [56, 57] or to assemble individual molecules [58]. The combination of optical tweezers and Rydberg atoms has proven to be useful to engineer Hamiltonians related to condensed matter systems [56, 59], to study non-trivial topological states of quantum many-body systems [60, 61], to prepare Rydberg-atom qubits [62, 63] and more.

We will stay tuned to new theoretical proposals and the great achievements of other experimental groups and adjust our research trajectory accordingly, in order to adopt the insights of other researchers and to study the most important unsolved problems accessible with our new apparatus.

### **Thesis outline**

The main effort of this thesis is aimed at designing, assembling and operating a new-generation apparatus that produces degenerate quantum gases of strontium. The primary requirement for the new apparatus is to be a versatile and conveniently extendable system to address novel challenges in the field of quantum simulation. In chapters 2 and 3 I describe the details and subtleties of the construction process: design and assembly of the vacuum system; procedures undertaken to attain

---

the ultra-high vacuum regime; construction of the laser systems needed to produce degenerate quantum gases and techniques used during the experimental cycle to bring the thermal atoms to quantum degeneracy.

After finishing assembling and characterizing the new apparatus, the next challenge is to develop novel techniques to facilitate achieving the objectives outlined above. The first innovative technique is to use the ultranarrow  $^1S_0 - ^3P_2$  transition of strontium, connecting the ground state to one of the excited state in the  $^3P_{0,1,2}$  manifold (described in chapter 4). The interest in this transition is related to its exceptional properties, namely its narrow linewidth at the mHz level and the electronic magnetic moment of the  $^3P_2$  state, leading to easily split magnetic sublevels. The frequency of the transition was measured for the fermionic isotope, which has a nuclear spin leading to rich hyperfine structure and to opening the transition linewidth to the mHz level by hyperfine mixing. By contrast, bosonic Sr, which does not have a nuclear spin, allows only very weak magnetic quadrupole transitions between  $^1S_0$  and  $^3P_2$  and additional methods are needed to increase the linewidth, such as applying an external magnetic field [64, 65]. The optical setup we assembled to address the  $^1S_0 - ^3P_2$  transition is expected to be a valuable tool for nuclear spin manipulation, for inducing state selective energy shifts, and eventually for an optical flux lattice realized with  $^{87}\text{Sr}$ .

The second technological ingredient we developed is a microscope objective (described in chapter 5), the key element of quantum gas microscopy. The microscope objective is tailored to fit into our apparatus and satisfies the requirements of the envisioned experiments. The crucial characteristics are a relatively high numerical aperture of 0.44, a long working distance of 18 mm and an optical correction for the glass plate of our vacuum viewport. The objective is constructed with off-the-shelf lenses and manufactured with in-house facilities using a simple stacking design, which makes the developed objective an easily fabricated research tool. The measured resolution is  $0.63\ \mu\text{m}$  at the wavelength of the broad blue transition (461 nm), which is the most suitable for fluorescence imaging. The performance of the objective is nearly diffraction limited at a wavelength of 532 nm, which is used to create optical tweezers.

# Chapter 2

## Experimental setup

The main focus of this thesis lies in the field of ultracold quantum gases. In this field clouds of neutral atoms are the primary object of study. They form rich physical systems, which provides opportunity to address a broad spectrum of fundamental problems. Obtaining an ultracold atomic cloud is the first milestone on the path towards exploring frontiers in the field of quantum gases. We prepare quantum gases of the alkaline-earth element strontium in a newly build machine with state-of-the-art performance. The new machine is a versatile apparatus, which combines the ability to accommodate promising existing ideas and the possibility to be upgraded to work with novel intriguing challenges. This chapter describes the design, assembly, operation and characterization of the new strontium apparatus. In the following sections I describe the steps on the route towards creating the quantum gas: building a vacuum system and achieving ultra-high vacuum (UHV), designing and constructing the laser systems and setting up additional optics and electromagnetic field coils.

### 2.1 Vacuum system

The vacuum system was designed and assembled during my thesis with the goal of performing experiments with ultracold strontium. Designing a vacuum system is the beginning of the road towards the creation of a quantum gas. We tried to construct a stable and robust system, incorporating expertise and knowledge of the successful experiments in the field of ultracold gases. The requirements for the experimental machine might vary significantly depending on the pursued goals, but modifications to an existing vacuum system are usually very involved if they are feasible at all. Therefore we tried to foresee potential upgrades and to assemble

a versatile vacuum system, adaptable to new challenges.

The vacuum system of our new apparatus consists of three sections: source, ultra-high vacuum and slower window (Fig 2.1). The sections are connected to each other with gate valves,<sup>1</sup> which allow to isolate specific sections from the rest of the vacuum system. This ability is important in order to refill strontium, to find and fix leaks, or to adapt the system to a new research goal without breaking the vacuum in the whole system. Each section is equipped with an angle valve,<sup>2</sup> so it can be connected to a pump station and pumped down separately. In the following subsections I describe details of the design and the assembly of the vacuum system.

### 2.1.1 Source section

Strontium is a soft metal with low vapor-pressure at room temperature. In order to obtain a sufficient atomic flux, the fraction of atoms in the gaseous phase has to be significantly increased. This is achieved by heating up the metallic chunks of strontium to a high temperature in order to sublimate individual atoms (Figure 2.2). This is an amusing twist: the first step on our way to produce an ultracold gas of atoms is to heat them.

The chunks of strontium are heated in an oven, which is part of the source section of the vacuum chamber. A hot gas of randomly moving Sr atoms is created and some of these atoms escape the oven in a collimated beam. In the following paragraphs I describe the source assembly and its main components: oven, transverse cooling section and differential pumping section (Figure 2.3).<sup>3</sup>

The oven heats chunks of strontium to sublimate atoms and collimates these randomly moving atoms into a high-intensity atomic beam with a low angular distribution. It is composed of reservoir, nozzle, heating assembly and insulation assembly (Figure 2.4).

The reservoir is a container for pieces of strontium. It is a straight steel tube with DN40CF flanges on both ends. One flange is used to fill the oven with strontium and closed by a blank during operation. The flange on the other side of the steel tube is connected to a flange with a nozzle.

The purpose of the nozzle is to reduce the solid angle of the atomic beam coming from the reservoir [71, 72]. This reduction helps to improve the fraction of atoms

---

<sup>1</sup>VAT 48132-CE44, all-metal valve with a pneumatic actuator.

<sup>2</sup>VAT 54132-GE02, all-metal valve with a manual actuator.

<sup>3</sup>The ion pump on the side of the tee is removed to get a clear view.

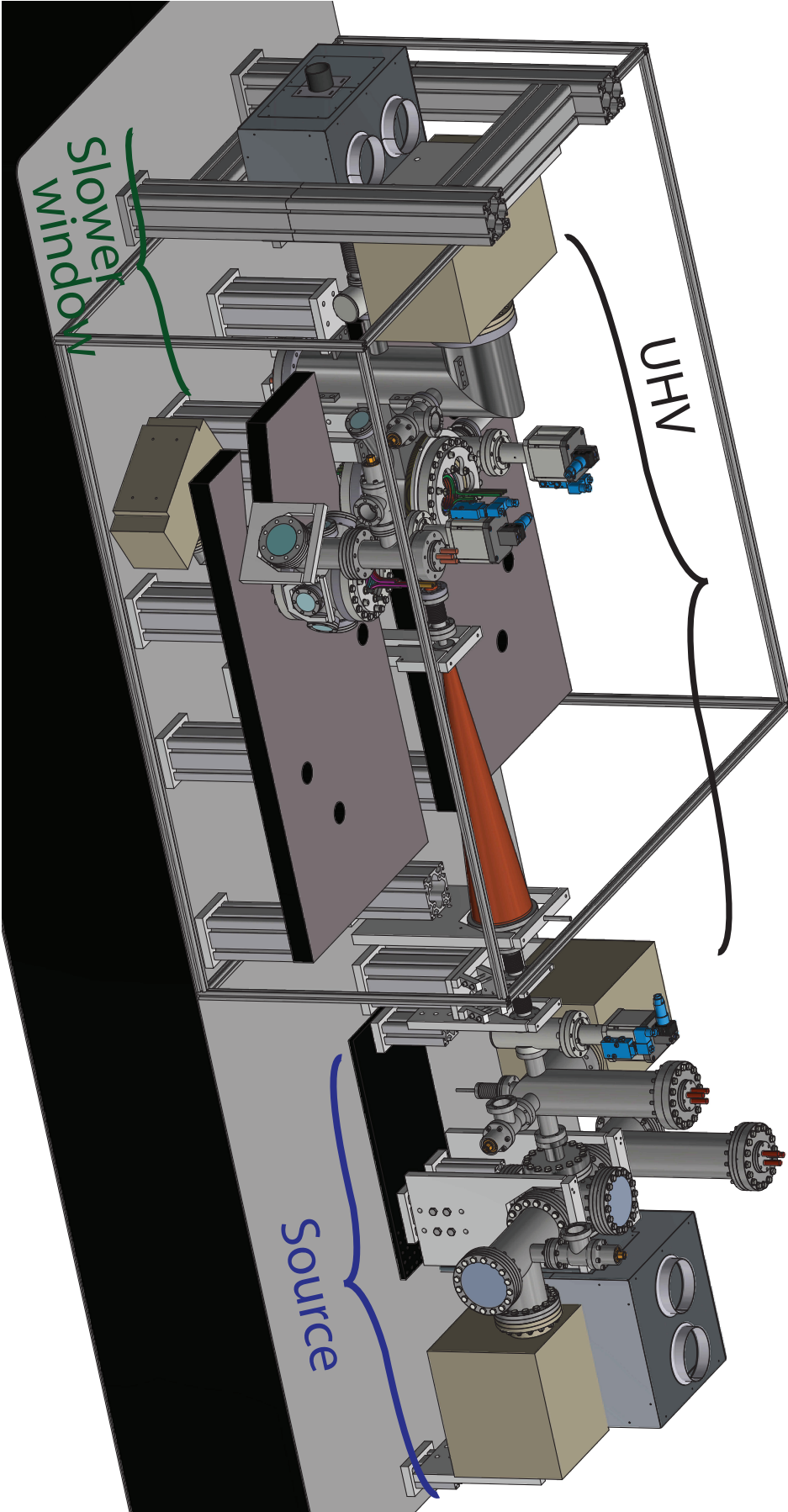
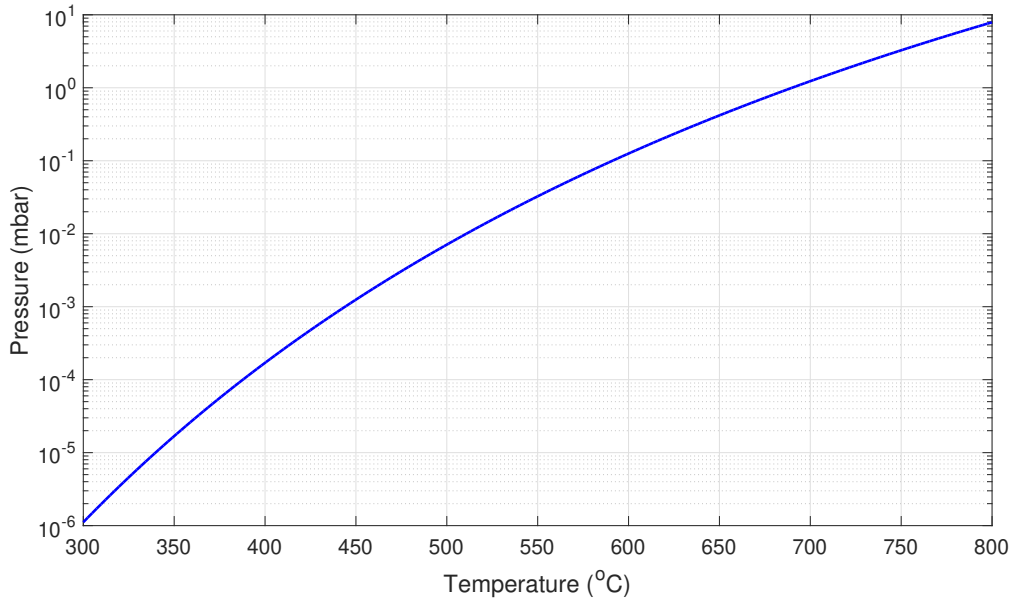


Figure 2.1: Vacuum system of the new apparatus. Labels on the drawing outline the three main sections: source, UHV and slower window.



**Figure 2.2: Vapor pressure of strontium as a function of temperature.** The plot is based on the equation:  $\log_{10}P = 8.750 - \frac{8427}{T}$  where  $T$  is temperature in Kelvin and  $P$  is pressure in mbar [66]. This equation agrees with [67, 68] and references in [66], although there are deviating Sr vapor pressure curves in literature as mentioned in [69, 70].

in the beam that reach the UHV section. The nozzle consists of an array of microtubes, which is placed in a custom made orifice cut through a double-sided DN40CF flange. If a Sr atom in the reservoir flies into the nozzle and has a velocity aligned with a microtube's axis, it can pass through the tube without collisions with the tube's wall. If an atom collides with the wall, it gets other chances of contributing to the collimated atomic beam, either directly after detaching from the wall and flying into the correct direction or after multiple scattering events with walls. Microtubes are arranged in a hexagonal lattice pattern in the triangular part of the orifice. The outside diameter of a microtube is  $210 \pm 7 \mu\text{m}$ , the wall thickness is  $51 \mu\text{m}$  and the length is  $8 \text{ mm}$ .<sup>4</sup> It is important to assemble the microtube array without gaps, because a large gap becomes the dominate source of atoms from the nozzle with broader angular distribution. The orifice holding the tubes was machined with a tolerance of  $200 \mu\text{m}$  to prevent structural disorder in the lattice pattern. This small tolerance is especially important for the apex of the triangle, because it allows to correctly place a single microtube at the bottom and to avoid dislocations of tubes (Figure 2.4 top). The front side of the nozzle is sealed by a cap with round output

<sup>4</sup>Cadence, Stainless Steel Hypodermic Tube, T-33 RW. Tubes were purchased with a length of about  $1.5 \text{ m}$ , then they were wire cut to the desired length.

aperture to shape the atomic beam. About 800 tubes are used to fill the orifice and about 450 tubes are located within clearance of the output aperture (Figure 2.4 top). Two wedges and a locking screw are used to fix the microtubes tightly in the flange.

The oven was designed to provide effective heating of the reservoir and the nozzle, while keeping the neighboring parts at room temperature. For heating we use nine thermocoax heating elements.<sup>5</sup> Using several elements provides independent control of the temperatures of different parts of the oven. The nozzle is kept at the highest temperature to prevent recondensing strontium in the microtube array. Accumulation of strontium might clog the microtubes. The clogged microtubes would act as uncollimated strontium source, which has a broad angular distribution, thereby reducing the efficiency of strontium usage. The blank flange side of the reservoir is the coldest spot of the oven in order to accumulate strontium there. The temperatures of the various oven parts is adjusted slowly with smooth changes over the whole assembly in order to prevent the creation of leaks. To monitor the heating process, eleven type K thermocouples are placed along the assembly.<sup>6</sup> Nickel gaskets are used to connect the oven flanges to lower the corrosion at high temperature and thereby reduce the risk of opening leaks.

The atomic flux can be varied by changing the temperature of the oven. At higher temperatures the atomic flux is increased, but it might cause premature depletion of the reservoir, so we avoid temperatures above 600 °C. The additional effect of the higher temperature is an increase of the average velocity of atoms coming out of the oven. It influences the fraction of atoms addressed in the deceleration process, since only atoms with velocities up to a specific finite value can be slowed. To conserve valuable strontium in the oven reservoir, the temperature of the oven could be reduced when the machine is not operating, for example most nights. However we do not lower the temperature daily out of fear of creating leaks in the oven assembly and we maintain the temperature constant. We have been operating for three years without noticeable changes of the atomic flux. To prevent heating of the vacuum cross connected to the oven, the nozzle flange is followed by an 85 mm long DN40CF to DN100CF reducer. The length of the reducer is also sufficient to pro-

---

<sup>5</sup>Thermocoax ZEZI10/50-50-50/2xCM10/KZ0510/0,5m. This resistance heating element is composed of a metal sheath, filled with refractory powder and a single current-carrying central wire. The wire has a high resistance central section, providing heating, and low resistance end sections, staying cold during the operation. The outer diameter of the heating element is 1 mm and the length of the non-heated ends is 50 cm. We use two types of elements, differing by the lengths of the hot, middle section, which is either 25 or 50 cm.

<sup>6</sup>Omega, TJ2-CAXL-IM60U-600; Transition joint probe with an ungrounded junction.

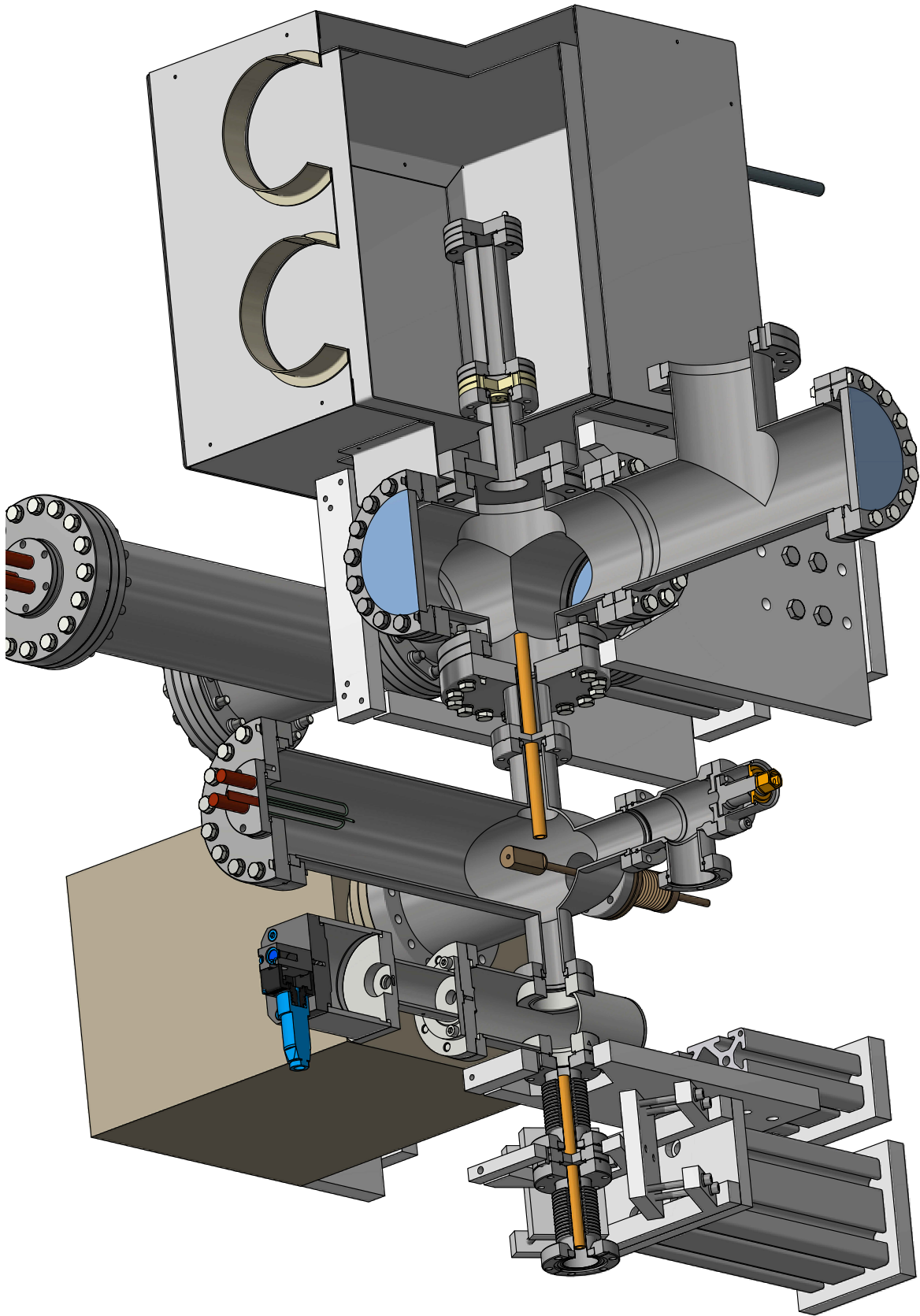
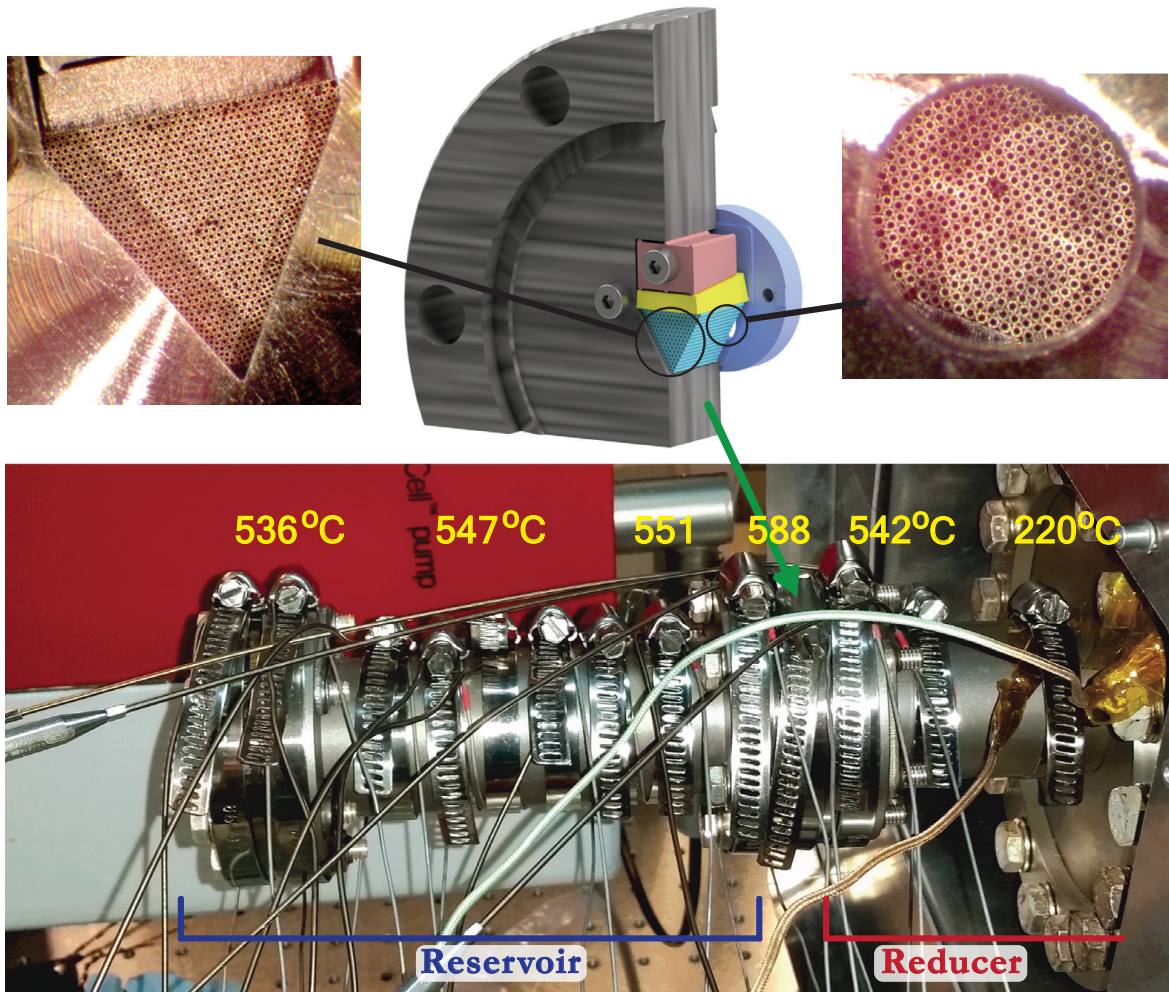


Figure 2.3: Source section of the vacuum system, shown in three quarter cutaway view.



**Figure 2.4: Oven assembly.** **Top:** Oven nozzle flange. The photos show the microtube array seen from the reservoir side (left) and the side from which the atomic beam effuses (right). **Bottom:** Oven with heating elements and thermocouples. Metallic chunks of strontium are contained in the reservoir, which is a steel vacuum tube, connected to the oven nozzle flange (green arrow). Yellow numbers indicate the temperatures of the specific sections along the oven assembly.

protect the windows in the transverse cooling (TC) section from being covered with strontium.

Strontium is a metal with silvery white color. When exposed to air it is quickly oxidized into a white powder. Hence filling of the reservoir with strontium should be done quickly, with minimum exposure to atmospheric gases.<sup>7</sup> To mitigate the detrimental effects of the atmospheric gases we improvised an isolated environment, created by transparent plastic film enclosing the oven assembly and filling the

<sup>7</sup>The reservoir is filled with 25 g of strontium (Alfa Aesar; strontium, distilled dendritic pieces, 99.95% (metals basis)).

prepared volume with nitrogen at a slight overpressure. Metallic chunks of strontium are delivered in a glass ampoule filled with argon. We tried to minimize the time between breaking the ampoule in the prepared protective atmosphere and lowering the pressure in the vacuum system, after having placed the strontium chunks into the oven reservoir. Despite the implemented precautions a slight oxidization of the strontium chunks was observed, especially noticeable on the small pieces. After placing strontium in the reservoir, the blank flange was attached to the back part of the oven and then the filling procedure is finished by pumping down the source section. In the future, when the Sr in the oven is depleted and needs to be refilled, the source section can be separated from the UHV section by a gate valve. In this way the vacuum in the UHV section is preserved and only the oven section needs to be baked again.

The insulation assembly around the oven allows energy efficient heating to the high temperatures ( $\sim 550^\circ\text{C}$ ). The assembly prevents heating parts that should remain at room temperature and inhibits the heating of air around the oven, which would lead to convective air currents, disturbing the passage of laser beams. The insulation assembly is composed of two aluminum boxes, an inner and an outer one, and an insulation material in the inner box. The inner box is built around the oven assembly and the reducer (Figure 2.3). The insulation material<sup>8</sup> inside it significantly reduces heat transfer. The outer box is at a distance of about 2 cm from the inner one with a minimal number of contacting parts between boxes. Room temperature air is blown through the gap between the boxes to cool them down and maintain the outer box close to room temperature ( $\sim 50^\circ\text{C}$ ). We do not observe a negative influence of the oven on nearby optics.

The oven is connected to the TC section, where the divergence of the atomic beam is reduced. We use molasses cooling on the blue  $^1S_0 - ^1P_1$  transition (32 MHz linewidth, 461 nm wavelength) in order to reduce the transversal velocity of the atomic beam. The molasses laser beams are sent transversally onto the atomic beam from two orthogonal directions and they are retroreflected. The beams pass through four DN100CF viewports,<sup>9</sup> see Figure 3.1.

We aim for a pressure below  $10^{-11}$  mbar in the main chamber to have a lifetime of the atomic cloud of at least on the level of several seconds. One of the major source of residual gases in our machine is the oven, which does not only emit the desired atomic beam of Sr atoms, but also outgasses undesired atoms and molecules in ran-

---

<sup>8</sup>Morgan SUPERWOOL<sup>®</sup> thermal ceramics.

<sup>9</sup>Zero length viewports, made from fused silica with anti-reflection coating for 461 nm.

dom directions. This effect is evident from the increase in pressure in the source section when operating the oven. Differential pumping tubes are installed between the oven and the UHV section in order to prevent a substantial amount of background gases from reaching the UHV section, while at the same time allowing the Sr beam to pass. A differential pumping tube works together with a vacuum pump to create a pressure difference between the two sections connected by the tube. To determine the attainable pressure ratio a simple model can be used. The first section (source section) is assumed to have a source of background gases, keeping it at a constant pressure  $p_{\text{oven}}$ . The second section has a vacuum pump with pumping speed  $S$ . The two chambers are connected by the differential pumping tube, which has a the conductivity  $C$ . The pressure ratio between two sections can be estimated to be [73]

$$\frac{p_{\text{oven}}}{p_{\text{UHV}}} = 1 + \frac{S}{C}.$$

The conductance of a tube with a length  $l$  much larger than its diameter  $d$  is proportional to  $d^3/l$  in the molecular flow regime [73, 74].<sup>10</sup>

We use two consecutive sets of differential pumping tubes. The first tube is welded to a reducer and placed in the cross of the TC section. Its length is 190 mm and its inner diameter is 9 mm. The second tube is welded to a DN40CF flange and placed after the gate valve of the source section. Its length is 160 mm and its inner diameter is 7 mm. For the tubes and pumps in our system the  $S/C$  factor is about  $10^3$ . For both differential pumping tubes in series we estimate that the pressure ratio between the source section and the UHV section is more than  $10^3$ . Also the Zeeman slower can be considered as a differential pumping tube because of its low conductance.

Another characterization of the differential pumping was inadvertently recorded when leaks opened in the UHV section after two years of operating the machine. This time the pressure in the UHV section increased almost by a thousand times and reached values close to  $\sim 10^{-7}$  mbar as estimated from ion pump currents. The pressure in the source section did not change noticeably and stayed at  $10^{-9}$  mbar. This unfortunate incident showed that with the chosen pumps and dimensions of the differential pumping tubes the ratio of pressure between the UHV and the source sections can be at least two orders of magnitude.

To efficiently load atoms into a trap, the atomic beam from the oven should be

---

<sup>10</sup>In the molecular flow regime the motion of individual particles is determined by collisions with the walls of the vacuum system, whereas collisions between different particles happen at much lower rate.

overlapped with the center of the main chamber. Atoms from the oven are firstly collimated by the nozzle, then radially cooled in the TC section and finally pass through the differential pumping tubes and the Zeeman slower. Vacuum system apertures along the line of atomic motion should be accurately aligned to avoid clipping the atomic beam. During the assembly of the vacuum system a laser beam was sent through the center of the main chamber to the center of the oven to help with this alignment. When baking the vacuum system, vacuum parts might move and change the alignment, therefore we enable the possibility to adjust the position of apertures shaping the atomic beam. Final optimization of those positions can be done on the operating machine by slightly tweaking the placement and orientation of parts to maximize the number of atoms in the magneto-optical trap (MOT, see section 3.3). The main chamber in the UHV section is rigidly fixed to the optical table and it defines the position of the MOT. The source section is mounted on a breadboard, which allows to move both the nozzle and the first differential pumping tube. The second differential pumping tube and the ZS are connected to bellows on each side. Bellows provide the flexibility needed to slightly move the assembled vacuum parts. They also reduce mechanical stress between parts, which are rigidly connected to the table, especially important during the high temperature bake (about 300 °C, see section 2.2.3). After the bakes only the second tube was adjusted with a system of set screws (Figure 2.3). The possibility to align other apertures for the atomic beam has not been used during the work for this thesis.

After the MOT is loaded, atoms flying from the oven to the main chamber become rather detrimental than useful. They collide with atoms in the MOTs or dipole trap, causing ejection of atoms from the traps. Furthermore non-trapped atoms fly to the slower window section and might form a metallic layer on the slower viewport. To remove these two adverse effects we use an atomic beam shutter assembly, placed on the bottom flange in the cross after the TC section (Figure 2.3). The main part of the assembly is a wobble stick<sup>11</sup> with an aluminum cylinder on top. The wobble stick is driven by a servo motor to shutter off the atomic beam during every experimental run after loading of the MOT is finished.

### 2.1.2 UHV section

The UHV section is the part of the vacuum system where atoms from the source section are slowed down and then confined in a trap. It was designed to be versatile

---

<sup>11</sup>Nor-Cal Products, WBL-275.

and suitable for different experimental challenges. At the same time we tried to keep construction simple and robust (Figure 2.5).

From the source section the atomic beam enters the Zeeman slower (ZS). The purpose of the ZS is to slow atoms below the maximum velocity that the MOT can capture. The main elements of the slower are two coils in the "spin flip" configuration. The first, longer coil is wound onto a custom made vacuum tube. The slower tube is water cooled: it is made from two concentric pipes, welded to two disks with water connectors (Figure 2.6). Water can flow between the pipes, cooling the tube and the coil. Additionally this design helps to avoid heat transfer from the coil to the other parts of the vacuum system, which might lead to excessive outgassing. Furthermore cycling the vacuum parts temperature up when using the ZS coil and down during the switch off time could lead to stress in the vacuum seals, creating leaks. The second, shorter part of Zeeman slower consists of two coils, which are wound on the long arm of the main chamber.

The atoms slowed by the ZS fly to the main chamber, where they are captured in the MOT. The main chamber is a custom made stainless steel vacuum chamber with a design adapted for creating degenerate quantum gases (Figure 2.7). It is designed to provide sufficient optical access to atoms and host experimental equipment: electromagnetic coils, a microscope objective and an RF antenna. For the main chamber we used zero-length fused silica viewports.<sup>12</sup>

The reentrant window is a custom made viewport, which penetrates into the chamber. This design allows to place equipment for the experiment inside the tube of the window, therefore this equipment is located close to the atoms despite being outside the vacuum system. This design is especially beneficial for electromagnetic coils and optical systems. The design of electromagnetic coils can be more compact and the electric power required to create a desired magnetic field in the trap region is smaller in comparison to coils that are farther away from the atoms. The reentrant window also helps to place a high resolution imaging system, e.g. our microscope objective, close to the atoms.

Radio Frequency (RF) fields are broadly used tools in experiments with ultracold gases and they might find implementation in our research. For creating such a field, an RF antenna is installed close to the trap location inside the vacuum system. The antenna consists of a single turn of an oxygen-free, high conductivity (OFHC) copper wire in a rectangular shape. For transferring an electrical signal into the

---

<sup>12</sup>The viewports have anti-reflection coatings from both sides with a reflectance per surface of less than 1% in a range from 461 nm to 1064 nm.

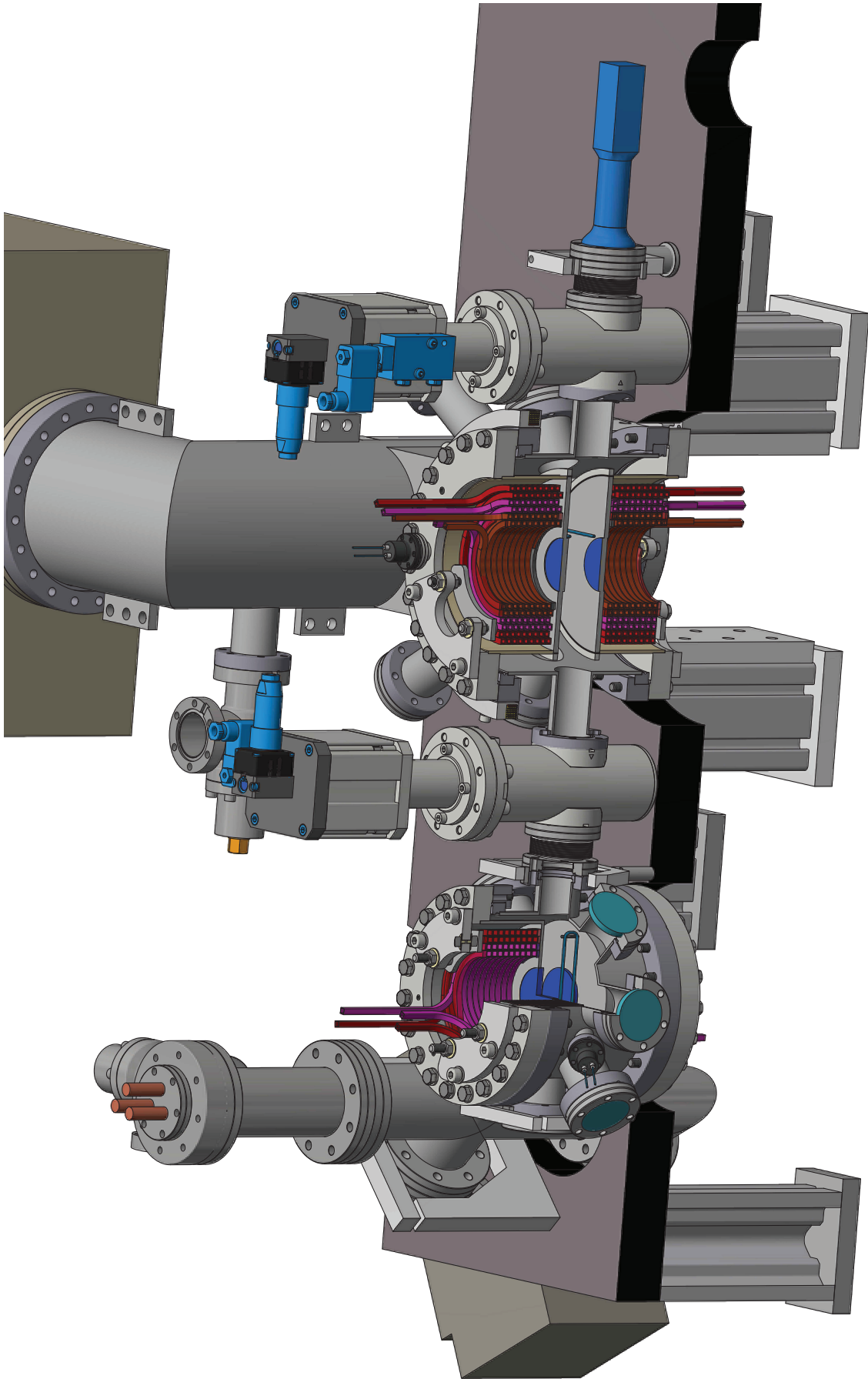
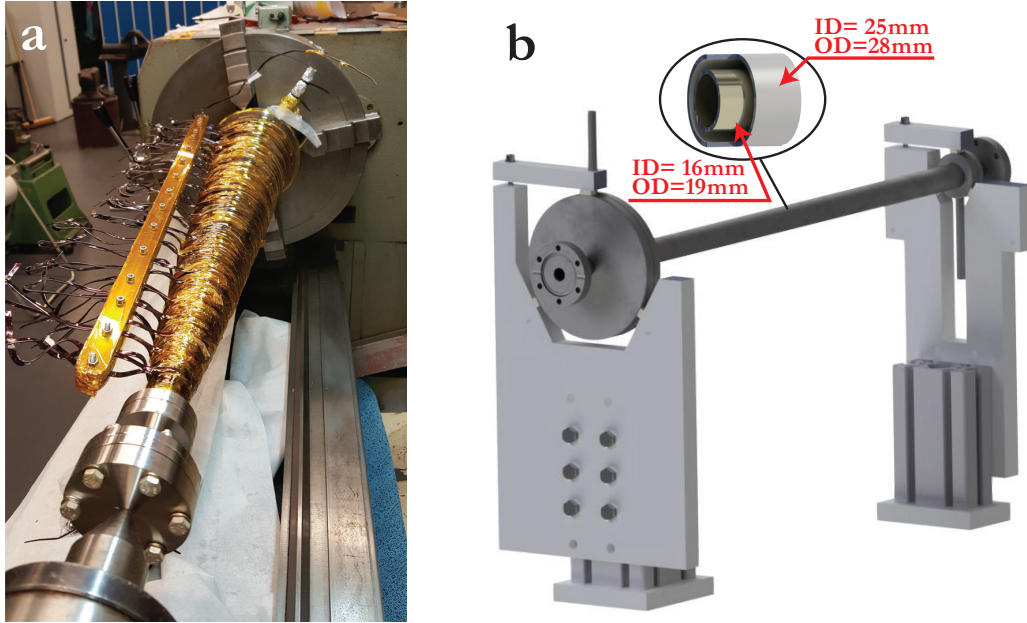


Figure 2.5: Part of the UHV section of the vacuum system, shown in a cut through main and science chambers.



**Figure 2.6: Long coil of the Zeeman slower.** **a**, Photo of the winding process of the long coil. To wind the coil the slower tube was fixed in a lathe, which was turning the tube and pulling a wire from a roll. We controlled the number of turns and checked the smoothness of the winding to avoid gaps. **b**, Slower tube without a coil, clamped by holders to the optical table. The total length of the tube is 788 mm. The top right corners of the holders are removed to provide a clear view.

vacuum system, the wire is soldered to a DN16CF feedthrough, located on the top of the reentrant window. The antenna is mounted to the protrusions on the top window with connectors made from Macor. Macor is a vacuum compatible glass ceramic, readily machined and with low electrical conductivity. Macor beads are used to prevent shortening of the copper wire to the steel chamber.

### Science chamber

New theoretical proposals in the field of ultracold gases often address intriguing and profound physical problems. While being exciting ideas, they might be technically challenging to implement in the experiment. The primary subject of our research are ultracold atomic clouds, which are initially located in the main chamber. Most of the optical access to the chamber is taken up by laser beams that are needed to produce degenerate gases. A further restriction to the research possibilities in the main chamber comes from the fact that the area around it is crowded with optical elements required to guide and shape those beams. Adding new elements close to the main chamber might be troublesome.

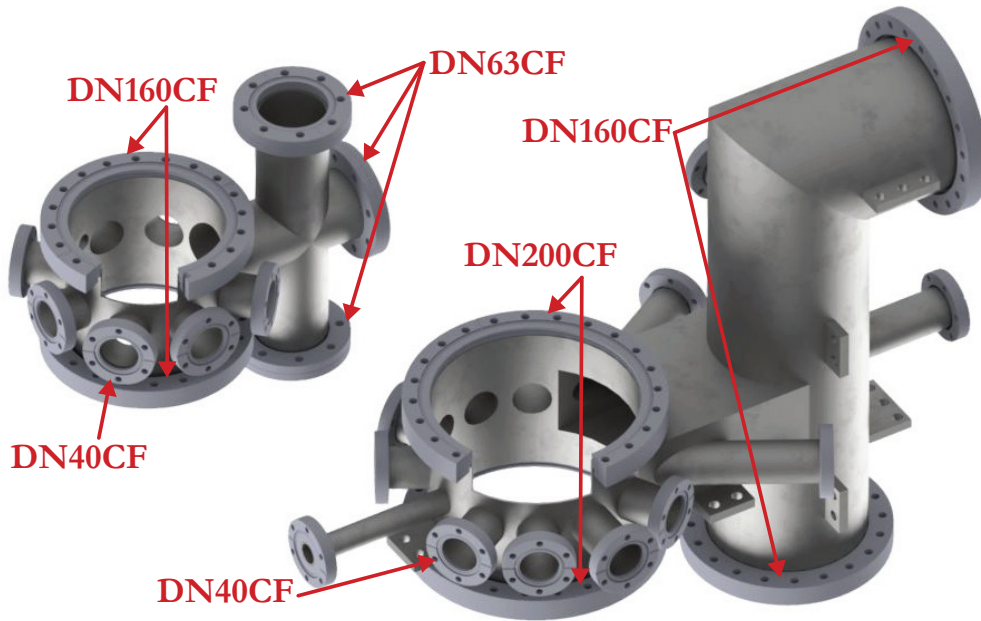


**Figure 2.7: Main and science chambers.** The main chamber is shown on the right side and the science chamber on the left side of the figure. Chambers are shown with a cut on the front facet to give a better view.

To get space for new research avenues another custom made stainless steel "science" chamber is added to the vacuum system. It is connected to an arm of the main chamber through a gate valve and welded bellows. The design of the science chamber is reminiscent of the main one, but it is smaller (Figure 2.7). Similarly to the main chamber, an RF antenna is attached to the top reentrant window. The antenna has the same rectangular shape and it is again made from OFHC copper. For electrical connection the wire is soldered to a DN16CF feedthrough, which is placed on the side of the chamber. For the science chamber we used the same fused silica viewports as for the main chamber. Trapped atoms in the main chamber can be moved to the science chamber by using for instance an optical transport with focus-tunable lenses [75].

### Glass cell

In some experiments with ultracold gases a glass cell is used instead of a stainless steel chamber. A glass cell has beneficial features, which are advantageous for certain applications. It has typically a smaller size than a steel chamber, so equipment for the experiment can be placed closer to the ultracold atoms. As I mentioned in the previous subsection a small distance to the atoms is especially important for a high

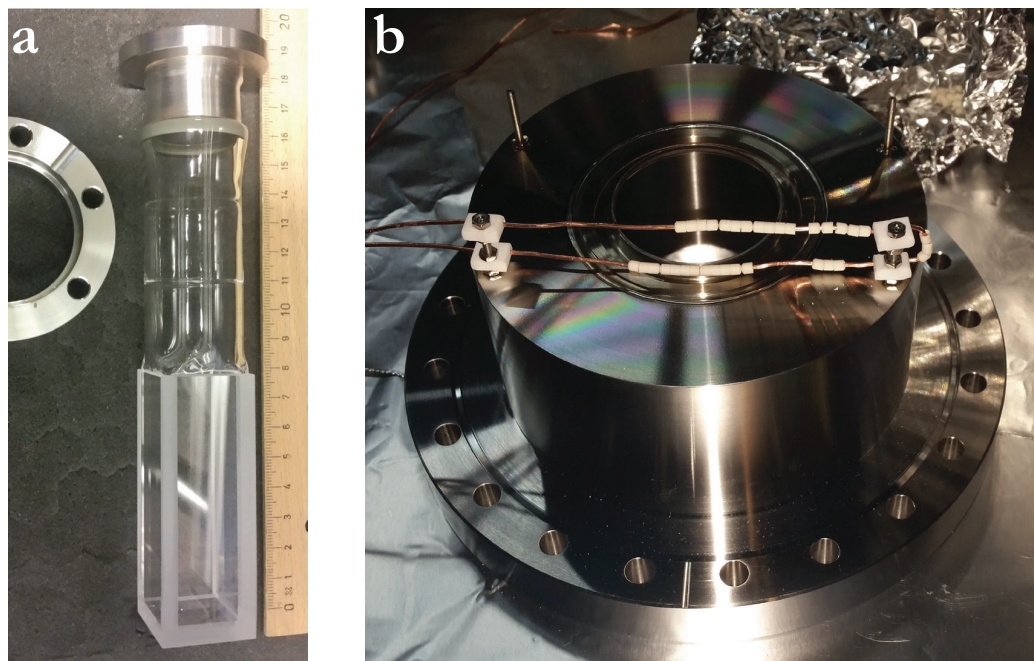


**Figure 2.8:** **a**, Glass cell before installation on the vacuum system. **b**, Top reentrant window for the science chamber with mounted RF antenna.

resolution imaging system, since it allows to use a microscope objective with high numerical aperture. Furthermore electromagnetic coils can be made smaller in size and require less power to create a required magnetic field. Using glass is beneficial for fast changes of a magnetic field since the eddy currents induced in metal vacuum chambers are avoided. A glass cell also provides more optical access to atoms, for example allows to irradiate the atoms with laser beams from many different directions, as required for the implementation of some artificial gauge fields. Using a glass cell also has its disadvantages and difficulties. Glass is a fragile material, so precautions are necessary when mounting equipment or working near the cell. The fragility of glass makes it also challenging to work with glass cells that have more than one connection to the steel parts of the vacuum chamber. Even limiting the number of connections to two comes with complications: the connections need to be on opposite ends of the glass cell, such that forces created during evacuation are strictly parallel to the glass-to-metal connection, and special mounting procedures need to be fulfilled [76]. Generally the price for manufacturing a glass cell is higher than for a stainless steel chamber.

The glass cell is added to the vacuum system to make the apparatus more versatile and flexible in exploring new frontiers (Figure 2.8). It is attached to an arm of the main chamber through a gate valve and welded bellows. The glass cell has a rect-

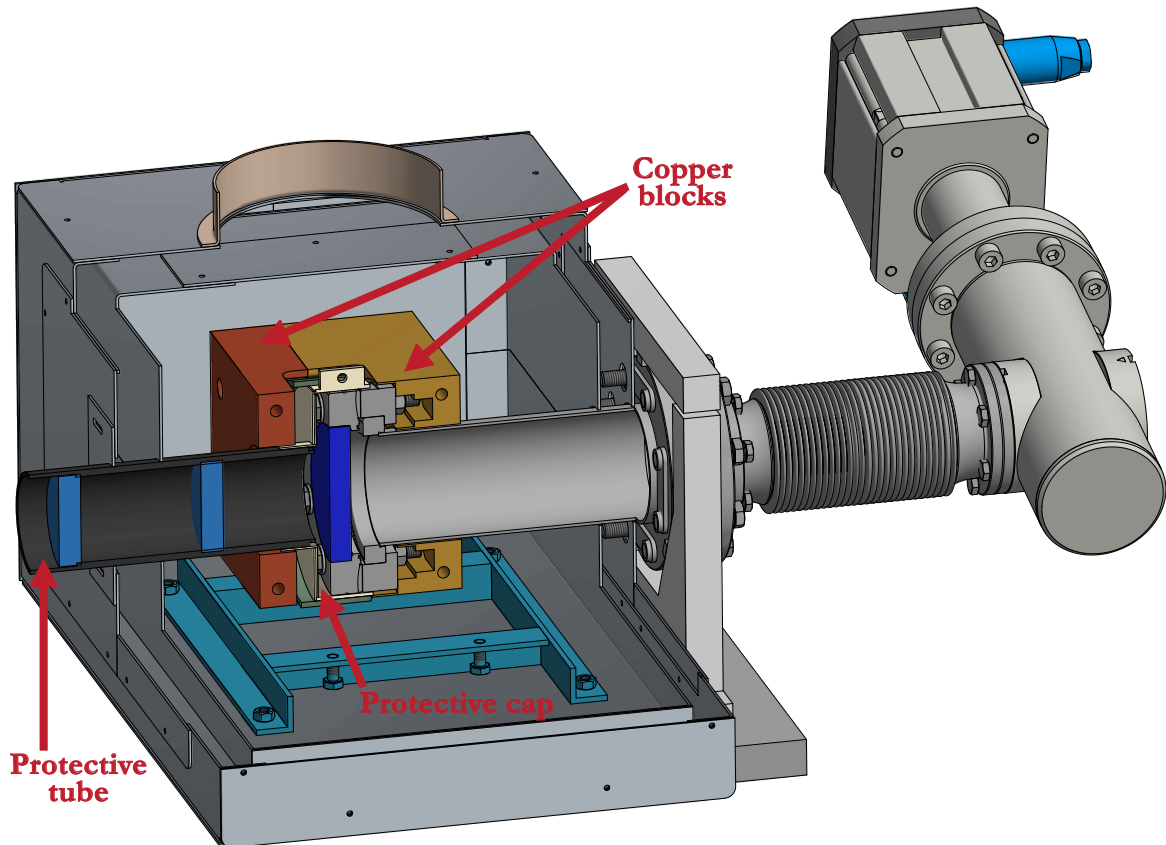


Figure 2.9: Slower viewport section, shown in a cutaway view.

angular form (80 mm×30 mm×30 mm) with a 100 mm long glass to metal connection to a DN40CF flange.<sup>13</sup> Welded bellows are used for protection from vibrations produced by the gate valve during opening or closing and also to avoid mechanical stress between connected parts. Atoms can be transported to the cell in a similar way as to the science chamber.

### 2.1.3 Slower viewport

Slowing the atoms in the oven's atomic beam is an important element of the experimental cycle with one of the key components being a laser beam counter-propagating to the atomic beam. This laser beam enters into the vacuum system through the viewport assembly in the slower viewport section. This section is located after the main chamber, along the path of the atomic beam. It is composed of the slower viewport, bellows, a heating assembly and an insulation assembly (Figure 2.9).

Atoms, coming from the oven, have velocities in a broad range. Only the slow

<sup>13</sup>The rectangular glass part is made by Hellma. The thickness of the glass is 5 mm and it is not coated. The glass-to-metal connection is made by Precision Glassblowing Inc.

part of the velocity distribution of the chosen isotope can be efficiently decelerated and captured in the MOT. Fast atoms from the distribution, other isotopes and molecules pass through the main chamber and reach the slower viewport section. These atoms and molecules settle on the walls of the vacuum system or directly on the viewport. Strontium is a reactive metal and depositing a layer of it might damage the glass. A Sr metal film would make the viewport less transparent or even reflective to laser light [77]. Therefore we need to prevent the Sr atoms to permanently stick to or even react with the window. We use a sapphire viewport, because sapphire is more resistant to an aggressive environment.<sup>14</sup> Sapphire is a hard, scratch resistant material, suited for high temperature applications. To increase the probability that Sr atoms reaching the window leave its surface, the viewport is heated to 150 °C. As heating element we use a mica insulated band heater,<sup>15</sup> which is powered by a variable autotransformer.

When heating vacuum parts containing glass elements, the temperature should be changed slowly to prevent cracking and opening of leaks. The recommended maximum heating rate for the sapphire viewport is 3 °C per minute. In our experiment the slower viewport is constantly kept at high temperature to reduce the risk of creating leaks during temperature changes, although the atomic beam is typically shuttered off at night using the atomic beam shutter. In case of a power supply failure the temperature could go down rapidly. Massive copper blocks are placed around the viewport to inhibit abrupt cooling, playing the role of heat capacitors. These copper blocks are heated by the viewport heating band to 120 °C without being in direct thermal contact with it.

The insulation assembly is placed around the viewport to avoid heating of neighboring parts. The design of the insulation assembly is reminiscent of the one used for the source section: inner and outer boxes, insulation inside the inner box and air cooling between the two boxes. Two additional requirements are specific to this insulation assembly. The first is that the viewport has to be protected from insulation material to avoid deposits on the transparent part or scratching its surface. The second is that optical access to the viewport is necessary for the Zeeman slowing laser beam. To provide sufficient isolation and guarantee optical access, the viewport is covered with an aluminum cap, which cosily sits between the copper blocks

---

<sup>14</sup>We used a DN63CF sapphire viewport from Torr Scientific Ltd, part number VPZ64SBBAR-LN, with an anti-reflective coating in the 450 nm and 800 nm range.

<sup>15</sup>Omega, Mica Insulated Band Heater; Model Number: MBH00236.

(Figure 2.9). An aluminum tube with two windows along its length<sup>16</sup> is attached to the viewport cap to keep the Zeeman slower beam path clear from the insulation material.

It might happen that with time part of the viewport becomes coated with strontium, despite all our efforts to prevent it. The atomic beam is collimated and most probably strontium would cover only a segment of the transparent part. In this case the viewport can be moved slightly, so that the laser beam goes through an uncoated part. To get the flexibility needed to adjust the position of the viewport, the whole slower viewport section is assembled on a board and it is connected to the main chamber through bellows. To reduce the amount of Sr reaching the viewport the atomic beam shutter opens only for MOT loading, otherwise it is closed. After three years of operation we have not found traces of strontium on the viewport. This lets us conclude that our precautions and methods work properly.

## 2.2 Attaining the UHV regime

In experiments with ultracold quantum gases, the lifetime of atoms in a trap is a critical parameter. It can limit the reasonable duration of MOT loading or evaporative cooling, thereby limiting the number of ultracold atoms, or can reduce the reliability of single atom detection. In most experiments a long lifetime of trapped atoms is highly desirable, but typically there are a number of restraining factors, such as heating by trap shaking or scattering of photons, molecule formation by three-body collisions, or, the topic of this section, loss by collisions between low temperature trapped atoms with room temperature background gases in the vacuum system. In these collisions, a slowly moving atom in the trap is kicked by a fast background gas atom or molecule. This event dramatically increases the momentum of the trapped atom and gives it enough kinetic energy to leave the trap. This loss mechanism is always present in ultracold atom experiments and considerable efforts are aimed at reducing its influence to an insignificant level. To mitigate the impact, the amount of background gases should be minimized, meaning that the ultra-high vacuum (UHV) regime needs to be reached, with the desirable pressure being below  $10^{-11}$  mbar. The UHV provides a near perfect isolation of the atomic ensemble from the environment and limits the collision rate between trapped atoms and residual gases in the system.

---

<sup>16</sup>Thorlabs, Part Number: WG12012-A. This is a high precision window, made from N-BK7, with antireflection coating in the range 350 - 700 nm.

Achieving UHV is an important step, taken after assembling the vacuum system. It is a challenging task, which involves several consistent stages of cleaning, pumping and baking. In this section, I describe the details and subtleties of achieving UHV in the new strontium apparatus.

### 2.2.1 Vacuum pumps

In experiments with quantum gases, reaching the UHV regime is a complicated problem, which has to be overcome for successful research. One of the steps on the route to deep vacuum is pumping down the system. The specific features of this step depend on the desirable final pressure and the vacuum pumps at the researcher's disposition. In this subsection I shortly introduce the basic working principles of the pumps used in our system and their purposes in the experiment.

The process of achieving the UHV regime starts from evacuating the vacuum system from atmospheric pressure to values below  $10^{-7}$  mbar. To attain this level, we use pump stations, which consist of a combination of a roughing pump (RP) and a high vacuum pump (HVP). Typically the RP brings the pressure from atmosphere to values below a few mbar. At this point it is possible for a HVP to take over and bring the pressure further down. Usually the HVP requires a low pressure at its outlet, so the RP provides a support during the whole pumping process. Therefore the intake manifold of the RP is connected to the outlet of the HVP and the intake of the HVP is connected to the vacuum system. We have four pump stations,<sup>17</sup> two were used to pump down the main apparatus and a third one was used for auxiliary bakes of parts that were installed inside the vacuum chamber. For rough pumping the pump stations are equipped with either a diaphragm pump or a rotary vane pump. To reach high vacuum we used turbomolecular pumps. In the following I explain some details of pumps used to attain the UHV regime in our vacuum system.

---

<sup>17</sup>**The first two pump stations** are composed of a diaphragm pump (Vacubrand MZ 2 NT), with a pumping speed of  $2.1 \text{ m}^3/\text{h}$  and an attainable final pressure of  $\sim 7$  mbar, in combination with a turbomolecular pump (Pfeiffer Vacuum TPU 062H), with a volume flow rate for  $\text{N}_2$  of  $56 \text{ l/s}$  and an attainable final pressure after baking below  $10^{-9}$  mbar.

**The third pump station** uses a diaphragm pump (Vacubrand MD 4T), with a pumping speed of  $3.3 \text{ m}^3/\text{h}$  and an attainable final pressure of  $\sim 2$  mbar, in combination with a turbomolecular pump (Pfeiffer Vacuum TPU 062H).

**The fourth pump station** is the most powerful one: the roughing pump is a rotary vane pump (Pfeiffer Vacuum DUO10), with a pumping speed of  $10 \text{ m}^3/\text{h}$  and a final pressure of  $\sim 10^{-2}$  mbar, in combination with a turbomolecular pump (Pfeiffer Vacuum TMU 260), with a volume flow rate for  $\text{N}_2$  of  $210 \text{ l/s}$  and an attainable final pressure after baking below  $10^{-10}$  mbar.

A diaphragm pump is a dry pump, which does not rely on lubricating agents for pumping. It is used to generate the low vacuum needed to start up the turbomolecular pump (Figure 2.10a). A simple single-stage pump consists of a small suction chamber, enclosed by a flexible diaphragm, moving up and down, and a system of valves, guaranteeing unidirectional gas flow. The working cycle consists of two strokes. In the first stroke the pump takes up gas from the vacuum system via an inlet valve. In the second stroke the pumped gas is compressed and ejected through an outlet valve. The diaphragm pump is a reliable and simple to use pump with decent pumping speed typically below  $10 \text{ m}^3/\text{h}$  and an ultimate pressure above  $0.1 \text{ mbar}$  [73].

An alternative to a diaphragm pump is an oil-sealed rotary vane pump (Figure 2.10c). This pump consists of a cylindrical working chamber, an eccentrically positioned rotor, inlet and outlet, and radially movable vanes, mounted on the rotor. Vanes divide the space between the rotor and the chamber's wall into separate regions with variable volumes. When the rotor turns, one vane passes the inlet valve, from which moment on gas is sucked into the input section, which is increasing in volume until the other vane passes the inlet. The gas that has been sucked in is compressed until the pressure is sufficient to open the outlet valve against atmospheric pressure. A low vapor pressure fluid is used to seal gaps between vanes and the internal wall of the pump's chamber. Proper sealing is necessary for a decent separation between the suction and compression sections. The fluid also lubricates moving surfaces and cleans working parts, it protects metallic parts from corrosion and equalizes temperature by transferring heat. A rotary vane pump is a reliable pump, which provides an exceptional pumping speed, typically in a wide range of  $3 - 1600 \text{ m}^3/\text{h}$  and reaches a final pressure in a range of  $10^{-2} - 20 \text{ mbar}$  [73].

After reaching rough vacuum, the second stage of the pumping process is aimed at lowering the pressure below  $10^{-7} \text{ mbar}$ . To attain such a low pressure we use turbomolecular pumps as high vacuum pumps in our stations (Figure 2.10b). The design of the turbomolecular pump is analogous to the design of a turbine. Essentially, it is a stack of blades alternating between two types: quickly turning rotating blades and mirror-symmetrical stationary blades. Gas atoms or molecules, approaching the inlet, collide with blades and momentum is transferred to the particles in each collision. Numerous kicks produce a directed movement of particles to the outlet, where they are pumped out of the vacuum system by the RP. Pumps, used in our stations are specified to attain pressures below  $10^{-9} \text{ mbar}$  after baking. A turbomolecular pump is commonly used for the second stage of the pumping

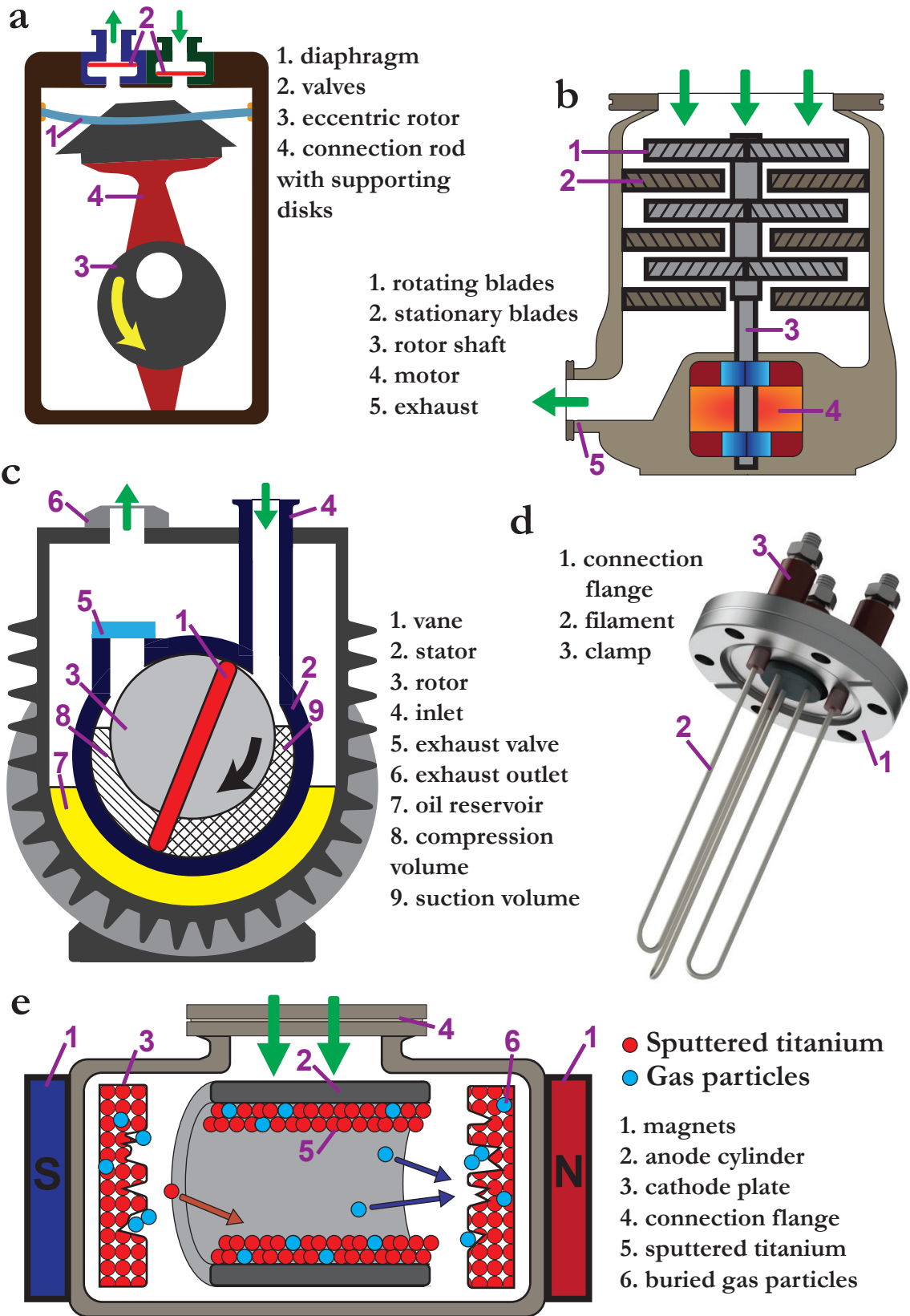


Figure 2.10: Schematics of vacuum pumps used to attain the UHV regime. a, Diaphragm pump. b, Turbomolecular pump. c, Rotary vane pump. d, Titanium sublimation pump. e, Ion pump.

process. It is a robust pump, which together with a powerful backing pump can achieve a sufficiently low ultimate pressure for UHV pumps to take over.

The final stage of the pumping process is bringing the pressure below  $10^{-10}$  mbar and maintaining it permanently at this level. To reach such deep vacuum getter pumps, in particular titanium sublimation pumps (TiSub) and ion pumps, are most commonly used in experiments with ultracold atoms. The working principle of these pumps relies on binding gas molecules in the vacuum system to a surface or in a bulk of a getter. Getter pumps are specified to work in a broad range of pressures, typically starting from  $10^{-3}$  mbar or even higher. However, lower initial pressure is preferable to prolong the lifetime of the pump and also to attain the UHV regime faster. After reaching UHV getter pumps can sustain vacuum in a closed vacuum system, so the pump stations can be disconnected from the vacuum system after closing the angle valves.

A TiSub is a simple getter pump, often used to achieve extremely deep vacuum (Figure 2.10d). A TiSub works by sublimating titanium, which is deposited in a thin layer on the adjacent interior walls. This titanium layer is a surface getter: it binds gas molecules to its surface by making compounds or it traps particles that diffuse into the bulk of the layer. For maximum pumping speed the titanium layer should be deposited on as large an area as possible. Therefore our TiSub pumps are connected to long, wide pipes to provide sufficient space for creating a large titanium layer. In addition, these pipes provide a high conductance connection to the remainder of the vacuum system. Furthermore the long pipe prevents exposure of viewports and ion pumps to the sublimated titanium, avoiding the coating of viewports and the electric shortening of ion pumps. To sublimate titanium we directly heat a filament by passing a high current ( $\sim 50$  A and  $\sim 5$  V) through it for about 2 min. It takes a long time for a newly deposited titanium layer to saturate. To maintain the UHV regime in our system, we run TiSubs once per several months to coat the saturated titanium layer with a fresh layer. We have four TiSubs in our vacuum system: two in the TC section, one close to the main chamber and one close to the science chamber.<sup>18</sup>

An ion pump is another getter pump, regularly used for UHV applications (Figure 2.10e). The working principle of this pump is based on ionizing gas particles, which then impinge on a surface and cause sputtering of a getter. The pumping speed depends on the nature of gas molecules or atoms in the vacuum system, the materials of the electrodes and the geometry of the pump. The main parts of the ion

---

<sup>18</sup>Vacgen ST22, with three filaments from TiMo alloy; 2 mm diameter; length 203 mm or 110 mm.

pump are two electrodes, cathode and anode, and external magnets. Usually the anode is an assembly of stainless steel tubes and the cathode consists of two titanium plates on both sides of the anode. A voltage of 7 kV is applied between cathode and anode. Magnets create a magnetic field along the axis of the anode tubes in the range of 1000-2000 G. The combination of electric and magnetic field makes electrons emitted from the cathode move on a helical trajectory, preventing them from reaching the anode in a straight path. On its way to the anode the electron has ample opportunity to collide with gas atoms and molecules and ionize them, producing positive ions and secondary electrons. Ionization is the main mechanism of pumping. It produces ions that are accelerated to high kinetic energy by the electric field. The mass-to-charge ratio of positive ions is larger than the one of electrons and therefore their trajectories are more straight. These ions collide with the cathode and stick to its surface by creating compounds or by burying themselves deeply into the bulk upon impact. The impinging ions release secondary electrons, which reinforce ionization. When ions collide with the cathode, cathode material (usually titanium or titanium and tantalum) is sputtered and deposited on the neighboring surfaces. Covered surfaces become a getter for gas molecules, similarly to the titanium layer created by a TiSub. Freshly sputtered cathode material can catch neutral particles or ions and bury them in the getter layer, which is continuously renewed by sputtering. At low pressure, below  $10^{-5}$  mbar, the current of the ion pump can be converted into pressure, hence the ion pump can be used as a vacuum gauge. In our vacuum system we have four ion pumps: two in the source section, one close to the main chamber and one close to the science chamber. To avoid limiting pumping speed by low conductance, these ion pumps are connected to the vacuum system by short pipes with big cross sections.<sup>19</sup>

### 2.2.2 Sources of gas particles in a vacuum system

Even in vacuum systems without real or virtual leaks, there are always background gas particles, which limit the ultimately achievable pressure. To efficiently reduce the amount of residual gasses and get into the UHV regime, it is necessary to understand the sources of particles in the vacuum system and methodically mitigate their influence. This subsection is devoted to a description of the main sources of background gases [73, 74, 78]: vaporization, diffusion, desorption and permeation

---

<sup>19</sup>RVIP-55-ST-M, RVIP-150-ST-M, RVIP-300-ST-M, with nominal pumping speed for nitrogen of 50 l/s, 125 l/s, 240 l/s. The ultimately attainable pressure is below  $10^{-11}$  mbar.

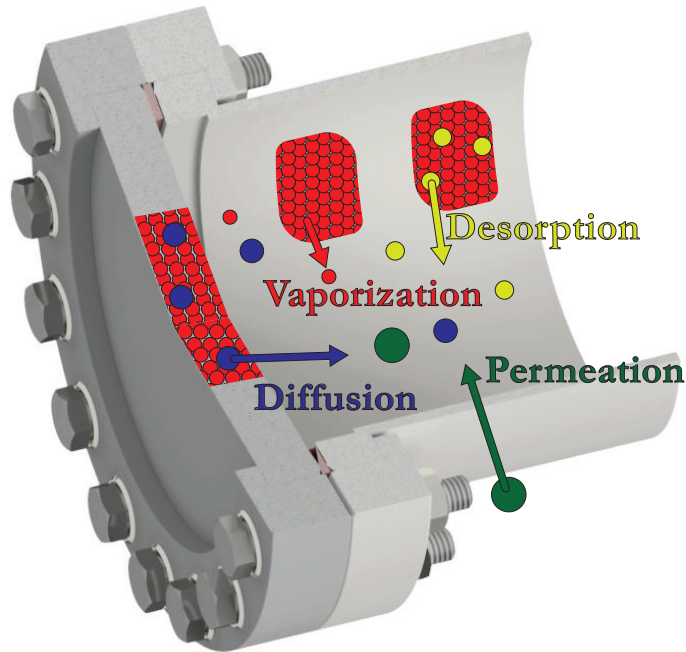


Figure 2.11: Sources of background gases in a vacuum system.

(Figure 2.11).

Vaporization is the temperature stimulated release of particles from a material. A particle can leave a surface if it acquires greater thermal energy than the binding energy to the bulk. Once equilibrium is reached, the rate of particles leaving the surface is balanced by the rate of particles coming back. When designing a vacuum system, materials chosen to build it should have negligible vapor pressure.

Diffusion describes the transport of impurity particles from the bulk to the interior surface of the vacuum chamber. Once particles are on the surface they can desorb. For most impurities, desorption is a faster process than diffusion. Desorbed particles are constantly removed from the vacuum chamber by pumps and an impurity concentration gradient is established in the bulk. Layers closer to the surface contain fewer impurities than deeper layers. This concentration gradient leads to an effective flow of impurities to the surface. For commonly used materials, diffusion of dissolved gases from the bulk is a long process. It can be a limiting factor in the achievable pressure for many years. Our vacuum system is mostly made from stainless steel and during the fabrication process a substantial amount of hydrogen is dissolved in the bulk of the steel. If preventive procedures are not undertaken, hydrogen is typically the primary background gas in a steel vacuum system. One well-known method to efficiently deplete hydrogen and other impurities from the bulk is baking of the steel parts under vacuum. The depletion efficiency relies on

the exponential growth of the diffusion constant with temperature, so even modest heating ( $\sim 300^\circ\text{C}$ ) for several weeks will lead to a significant depletion, resulting in an orders of magnitude lower pressure in the vacuum system after cooling to room temperature.

The third source of background gases is desorption of gas particles from the inner surface of the vacuum system. These gas particles can be adsorbed on the surface during construction, maintenance, or accidents that spring leaks by exposing the inner surfaces to atmosphere. The rate of desorption depends on several parameters, the most significant being the type of contaminant, the condition of the surface and its temperature. Particles that are weakly-bound to the surface (desorption energy  $< 70$  kJ/mol) have low residence time on the surface and effectively desorb even at room temperature. Tightly-bound particles (desorption energy  $> 100$  kJ/mol) have a very low probability to be detached and form a negligible source of background gases. However, compounds with intermediate binding energy (desorption energy  $\sim 70 - 100$  kJ/mol) have significant outgassing rates and can cause a noticeable amount of residual gases. To efficiently detach impurities of this type, external energy is needed. The typical way to provide energy for detaching is thermal (baking), although there are alternative methods: electron or ion-stimulated desorption, stimulated chemical reactions, photodesorption and others. Increasing the temperature by heating changes the rate of desorption significantly. For instance, one of the common contaminants in a vacuum system is water, which is nearly unavoidably deposited on the interior surfaces when exposing the vacuum system to air. The desorption energy of water from stainless steel and aluminum is between 80 kJ/mol and 104 kJ/mol. Thus the desorption rate of a water monolayer is small at room temperature, but it is increased remarkably during bakeout, such that baking to  $\sim 160^\circ\text{C}$  for a week is usually enough to remove it.

Another mechanism, causing an increase of pressure in the vacuum system, is permeation. External gas from the outside environment penetrate through the chamber walls into the vacuum. This process happens in three steps: adsorption of particles on the outer walls at high ambient pressure, diffusion through the bulk and then desorption from the interior wall. Steady-state permeation can be considered an unavoidable leak of particles into the vacuum system. Generally, permeation depends on the material of the wall and its thickness, on the surface area and the difference in pressure between inside and outside. The solubility on the outer surface does not depend strongly on temperature, but the diffusion through the bulk and the following desorption are increased drastically with temperature. Hence,

the total rate of permeation is increased at higher temperature. In comparison to other sources, permeation gives an important contribution to pressure only for thin stainless steel walls or glasses, for example through a glass cell or a viewport. An infamous example is helium, which permeates glasses easily because of the smallness of He atoms.

The described sources could delay or even prevent achieving the desirable pressure in the vacuum system. Rigorous consideration of these sources are needed when designing and assembling the system. Over many years of developing vacuum technology, several methods and procedures were established to address the difficulty of lowering pressure in vacuum systems. This topic is broadly addressed in various fields of science and industry, such as manufacturing (production of semiconductors, displays, power stations, etc.), scientific research (ultracold atoms and ions, particle accelerators, detectors of gravitational waves, etc.) and many other applications. While going through extensive literature, one should realise that there is no unique comprehensive technique that guarantees success in vacuum endeavors [79]. Each vacuum system is special in its own manner and requirements depend on its specific application. While working on our apparatus, we tried to collect knowledge from different sources and relied on the expertise developed in our lab.

The lower the required vacuum pressure is, the more thorough one has to be with the preparations of the vacuum system [80]. These preparations start with manufacturing parts of the vacuum system according to UHV standards: avoiding trapped volumes and pits, cracks on the surface, swarf aggregated into the material, etc. Then comes the cleaning of the interior walls of the vacuum system components according to general recommendations for UHV systems [81]. We used a simple technique of cleaning with chemicals, sometimes in combination with ultrasonic bathing for small parts.<sup>20</sup> It is recommended for the final phase of rigorous surface cleaning to bake the vacuum elements. The details of the baking procedure are discussed in the following section.

After the surface is purified from contaminations, outgassing from the bulk can limit the ultimate pressure. One of the effective and broadly used techniques to overcome diffusion of impurities from the bulk is baking. A high temperature bake ( $\sim 300^\circ\text{C}$  and higher) accelerates the depletion process and shortens the time to achieve the ultimate pressure. To achieve the UHV regime, two different types of

---

<sup>20</sup>There are other cleaning techniques, broadly used in vacuum engineering, such as physical cleaning (bead blasting, grinding, polishing, etc.), special methods (passivation, glow discharge) and others.

bakes can be chosen [81]. The first type is a bake under vacuum, where the assembled system is pumped down to low pressure and then baked at high temperature. The second type is baking at air under atmospheric pressure and it relies on creating an oxide layer on the surface, which becomes a barrier and does not allow impurities to leave the bulk. The answer to the question, which type gives the smallest outgassing rate afterwards is not clear in literature. We chose a vacuum bake for our apparatus, because we have experience with this type of bake and also we have the necessary equipment and facilities in the lab.

The temperature of the bake defines the desorption rate from the material, and therefore it sets the time required for the entire cleaning procedure. Typically the vacuum system has elements that define the upper limit for the maximum temperature, for instance elements with a glass to metal connection, such as viewports or glass cell.

### 2.2.3 Baking of the new strontium apparatus

To achieve extremely low pressure, the vacuum system should be assembled according to the demanding rules established to build UHV systems. After finishing the assembling process, it is important to verify the leak tightness and vacuum quality of the newly constructed system. To lower the danger of vacuum element malfunctions, the vacuum system is designed to be as simple as possible since each vacuum flange has a risk of failure and each component inside the vacuum bears a risk of outgassing or virtual leaks. Separating the system into different sections by gate valves helps with debugging and repairing if that is required. To examine the reliability of the vacuum system, we thoroughly searched for leaks directly after assembling and also after each bake. To locate leaks we used a residual gas analyzer (RGA), which was placed on each pump station.<sup>21</sup>

The depletion rate of dissolved hydrogen and other impurities from the bulk depends drastically on temperature. In our vacuum system the maximum temperature of the bake is limited to values below 200 °C by viewports and the glass cell. Due to this limitation we decided to execute the baking process in two steps. In the first step, we used stainless steel blanks instead of elements with glass. This change allows to raise the maximum temperature of the bake to 300 °C, with the main goal to efficiently deplete impurities from the bulk. In the second step, we finished as-

---

<sup>21</sup>For pumping the vacuum system during bakes, we use pump stations. Each station is equipped with an RGA, either an SRS 100 or a PrismaPlus QMG220.

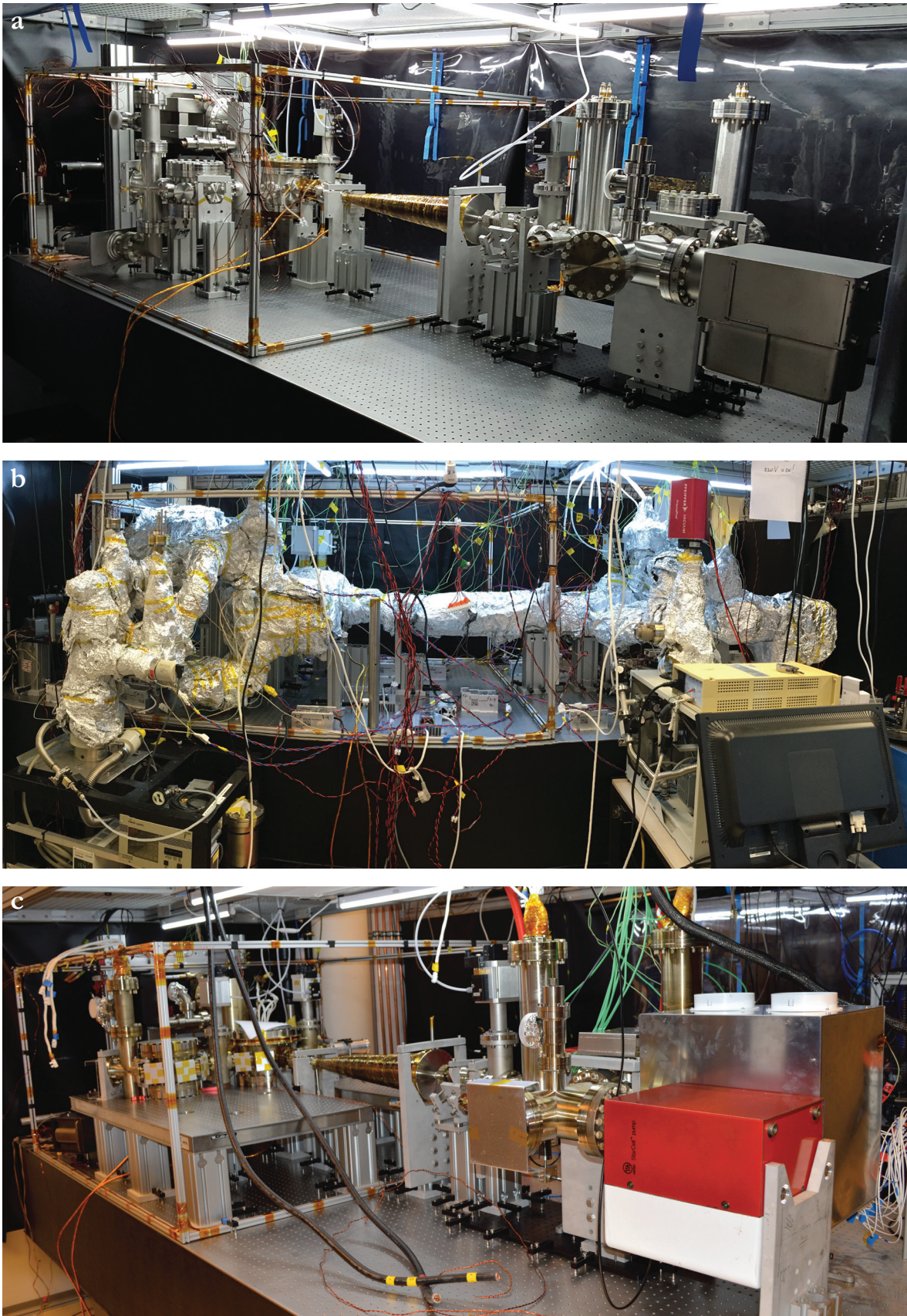


Figure 2.12: Vacuum system of the strontium apparatus. **a**, Before the high-temperature bake. **b**, During the high-temperature bake. **c**, After both bakes.

sembling the vacuum system by installing the elements with glass. The primary purpose of the second bake is to clean interior surfaces of the system after the unavoidable exposure to air. During the second bake the temperature was maintained at a level below 160 °C (Figure 2.12).

While baking the vacuum system the temperature has to be properly controlled and increased slowly and uniformly. When changing the temperature it is important to avoid gradients, because different parts of the vacuum system could expand with different rates and the resulting mechanical stress could open leaks. To have a good control during bakes, we placed about 60 thermocouples in various locations on the machine<sup>22</sup> and automatically measure values every 5 seconds. The temperature was changed slowly, with a maximum rate below 7 °C/hour and we tried to change it evenly across the machine. For heating we used heater tapes, which were wrapped around the whole machine and the connection tubes to the pump stations.<sup>23</sup> After placing heating elements and thermocouples, the machine was wrapped in several layers of aluminum foil. These layers act as thermal insulation resulting in more uniform heating and allow to reach high temperatures without excessive influence on the lab environment.

Figure 2.13 shows the pressure in the vacuum system<sup>24</sup> and the temperature for several sections of the machine as a function of time during the first vacuum bake. The readings of other thermocouples from different locations on the vacuum system are fairly similar to those shown in the plot. At the beginning and ending of the bake the temperature was changed during the day and left constant during the night. This time management explains the steps in temperature and corresponding peaks in pressure. In the first bake we reached temperatures close to 300 °C. On the 14<sup>th</sup> day of baking, we decided to increase the temperature by about 25 °C to obtain a better efficiency of removing impurities from the bulk and a corresponding increase of pressure is clearly visible in the plot. When the system was being cooled down, we degassed the TiSubs a few times to clean them and the associated narrow peak in pressure is noticeable on the 38<sup>th</sup> day. While cooling down, the cold cathode gauge reached its limit at a pressure of about 10<sup>-9</sup> mbar. Therefore we switched to the hot cathode gauge, which can measure slightly lower pressures and recordings from it are shown in the inset. Almost at the end of the bake, a leak opened and

---

<sup>22</sup>We use type K thermocouples, made from thermocouple cable (Omega, GG-KI-24-300M).

<sup>23</sup>Omega, ultra-high temperature heating tapes (STH052-100, STH102-060 and STH102-080); Omega, mica insulated band heaters (MBH00236, MBH00274 and DB-100182).

<sup>24</sup>For measuring pressure, the pump stations are equipped with cold and hot cathode gauges.

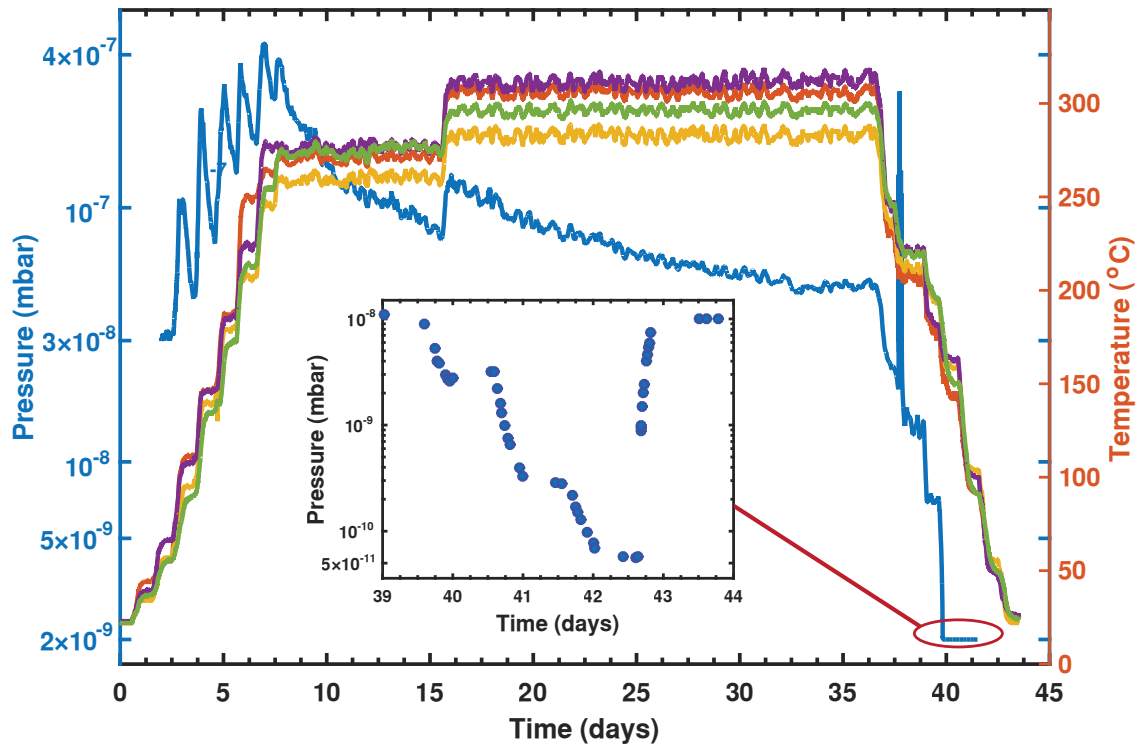


**Figure 2.13: Pressure and temperature during high temperature bake.** The temperature is shown for four different parts of the machine, representing different sections: cross with wobble stick (orange), main chamber (green), slower window (red) and oven reservoir (purple). The measured temperatures in others locations are similar to the data presented here. The pressure was measured with a cold cathode gauge and, during the last days of the bake, with a hot cathode gauge (inset).

the pressure went up. This was not a serious issue since the vacuum system was anyways exposed to air after the bake in order to exchange blanks with viewports. Before executing the second bake we rigorously tested the joints of vacuum flanges and fixed the suspicious connections either by stronger tightening or replacing the gasket.

Temperature and pressure during the second vacuum bake are shown in Figure 2.14. We followed a similar baking procedure to the first one, but this time the maximum temperature was limited to values below 160 °C, safely lower than specified for viewports and the glass cell. Analogous steps in temperature and associated peaks in pressure are recognizable at the beginning and the end of the bake. The TiSubs were degassed on the 8<sup>th</sup> day with a clearly distinguishable behavior: a corresponding dip in pressure, while the newly deposited absorbing layer is pumping background gases, and a following increase in pressure, while this layer is satu-

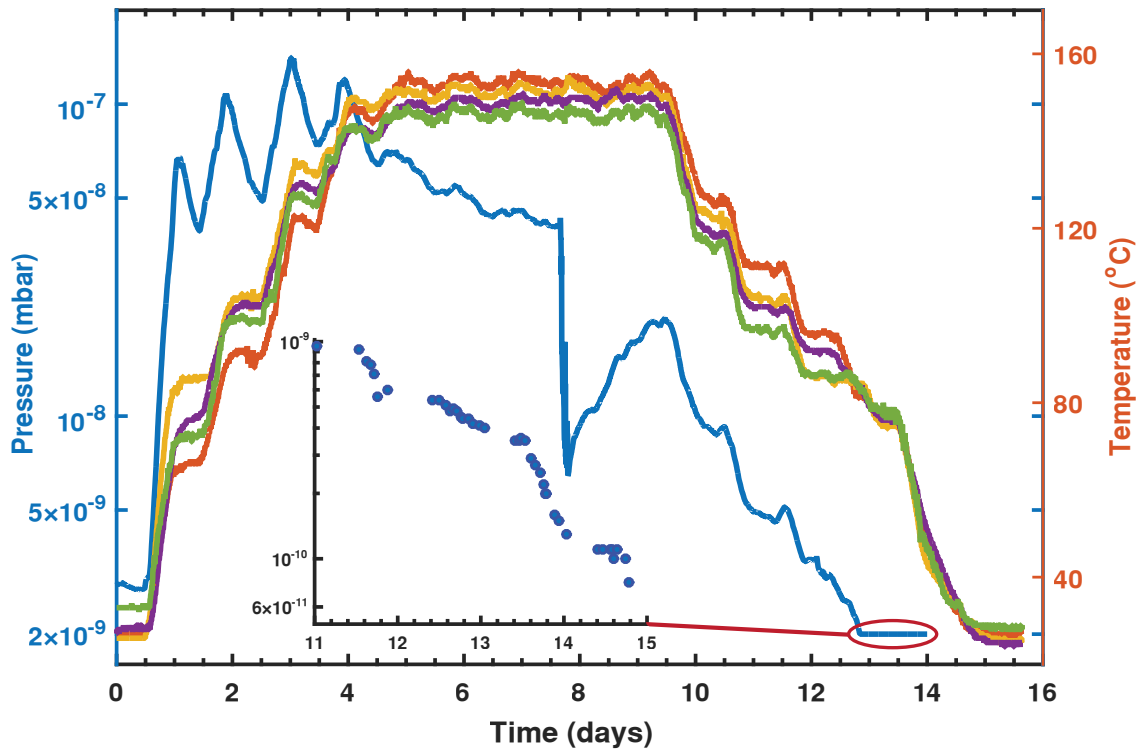


**Figure 2.14: Pressure and temperature during the second bake.** Temperature is shown for four different parts of the machine, representing different sections: TC section (orange), back window (green), oven reservoir (red) and main chamber (purple). The measured temperatures in others locations are similar to the data presented here. The pressure was measured here with a cold cathode gauge and, during the last days of the bake, with a hot cathode gauge (inset).

rating. At the end of the bake the pressure in the vacuum system reached a level around  $10^{-11}$  mbar. After finishing the second bake we again searched for leaks and detected a few minor openings on flange connections. Fortunately, we were able to fix the detected leaks by simply stronger tightening of bolts, exploiting a gap that we had intentionally left during assembly between the two metal flanges of the connection. After the leaks were eliminated the TiSubs were run a few times and the pressure dropped even lower, which brought a pleasant result for our endeavors.

During these two bakes the vacuum system was pumped by pump stations and internal ion pumps were switched off to avoid their saturation, which could have resulted in the release of adsorbed gases later. After finishing the second bake, the pump stations were disconnected and since then the vacuum is maintained by ion pumps and TiSubs. Our vacuum system is designed without dedicated vacuum gauges, so for monitoring the pressure we rely on measurements of the ion pump

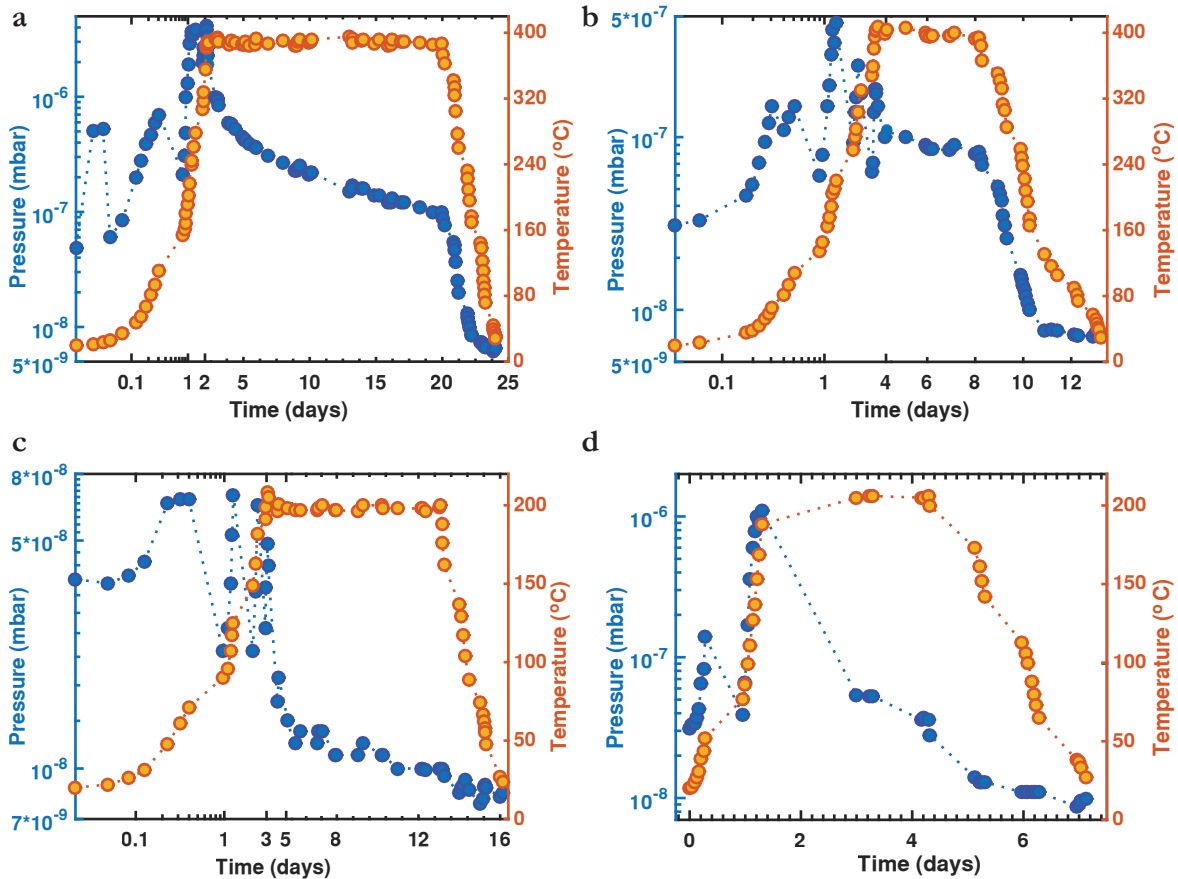


**Figure 2.15: Pressure and temperature during separate bakes of parts inside the vacuum system. a, Oven assembly. b, Stainless steel parts of RF antennas. c, Tip for the wobble stick. d, Copper wires.**

currents, which are proportional to pressure. This method allows us to determine an upper bound of the pressure, but to establish an accurate value a suitable vacuum gauge should be used. Pressure measurements performed with ion pumps located in the UHV section are at the detection limit of about  $1 \times 10^{-10}$  mbar. When the experiment is running and the oven is heated up to a high temperature ( $550^\circ\text{C}$ ), ion pumps located in the oven section show values of about  $10^{-9}$  mbar. This high pressure in the oven section does not disturb the vacuum quality in the main chamber, because of the low conductance of the differential pumping tubes and large pumping speed in the UHV section.

The small parts that were installed in the vacuum system underwent a separate high-temperature bake from the one of the vacuum system (Figure 2.15). Generally, rigorous cleaning of these parts is necessary, particularly for the ones machined in our mechanical workshop. The reason is that oil traces are possibly left after manufacture, since machining metals, especially stainless steel, completely without

lubricants is complicated. Additionally some in-vacuum parts are made from materials different from stainless steel, so the requirements for baking are different. In our vacuum system the elements that were treated separately are the nozzle, the RF antennas and the tip of the wobble stick.

The nozzle is composed of several parts: a specially made flange, microtubes, screws, a front plate and wedges (Figure 2.4). All of them are made from stainless steel, so it is necessary to deplete impurities from the bulk. The nozzle is heated up to a high temperature during the oven operation, thus it might be considered a baked element even without additional treatment. However, our concern was contaminating the whole vacuum system with possibly remaining oils, and therefore we baked it separately.

Other elements inside the vacuum system are the RF antenna assemblies and the tip of the wobble stick. This tip is made from aluminum and the RF antenna consists of stainless steel nuts and set screws, OFHC copper wires and beads made from Macor. All mentioned materials are standard choices for UHV and commonly used across diverse applications, and yet, the cleaning procedures vary between different fields of industry and research laboratories [79]. Although an ultimate procedure could not be established, there are acceptable commonalities among different procedures described in the literature. For the aluminum tip we chose a vacuum bake for ten days at a maximum temperature around 200 °C. It is not recommended to exceed this limit to avoid changing the structural strength, although this parameter is not crucial for our application. The OFHC copper wires were baked at a maximum temperature around 200 °C for three days.

To bake in-vacuum parts we assembled a separate, simple setup. The main part of the setup was a stainless steel chamber, which was used as a container for the small parts. This chamber was pumped by a pump station and heated up with similar technology to the one used to heat the main vacuum system. Retrospectively, the separate bake might be an excessive effort, although when dealing with vacuum it is better to be on the safe side.

## 2.3 Laser systems

In the previous sections I described the preparation of the low divergence strontium beam directed from the oven to the UHV section. By addressing different optical transitions, thermal atoms in the strontium beam can be decelerated, cooled, trapped and even brought to degeneracy. The preparation of an ultracold gas or

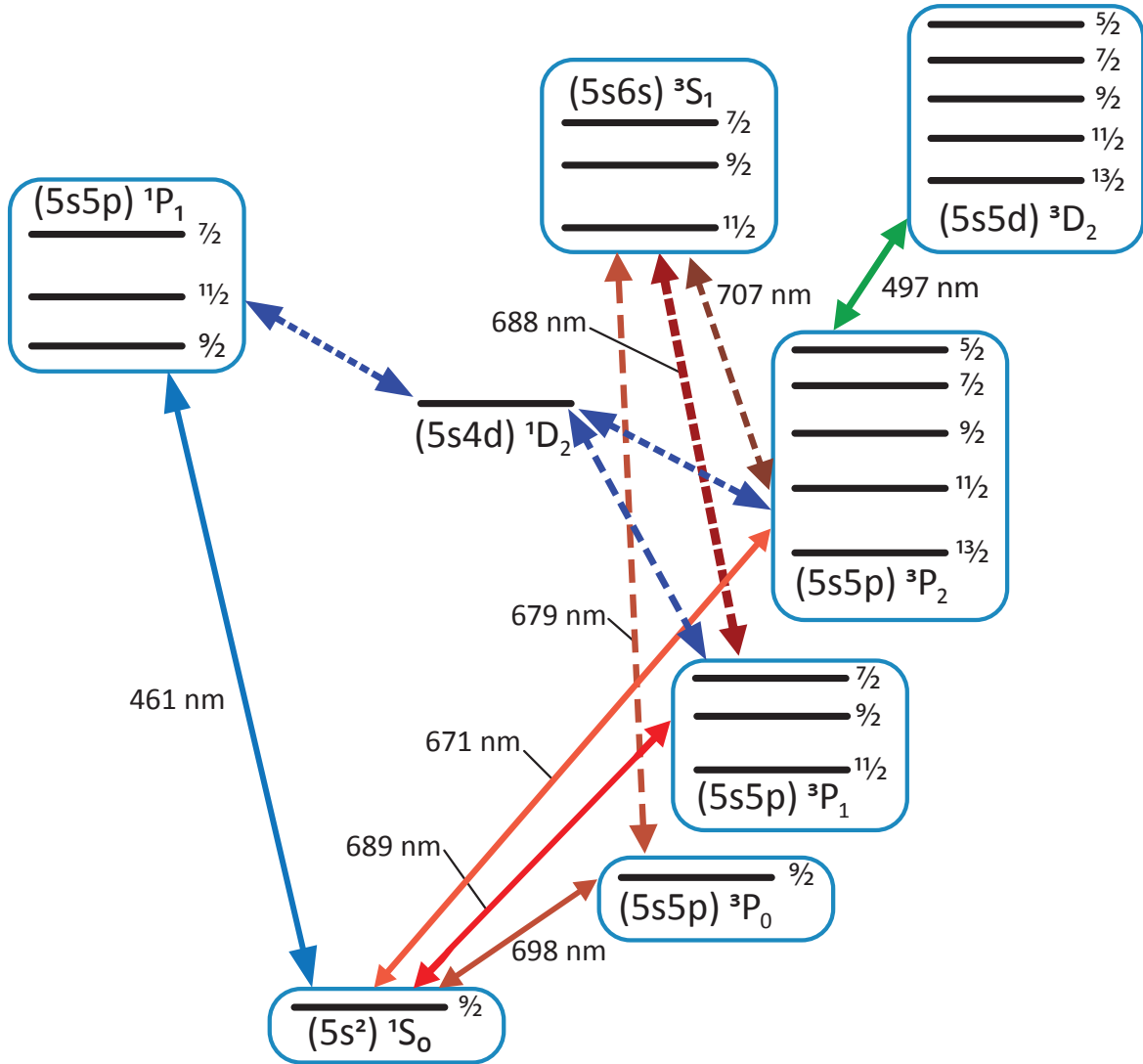


**Figure 2.16:** Level diagram of the low-lying energy states of  $^{87}\text{Sr}$ . The diagram for bosonic isotopes has the same structure but without hyperfine sublevels. The hyperfine splitting of the  $^1D_2$  state is omitted for simplicity.

even quantum gas is the starting point of each experimental cycle and its performance relies on stable and easily manageable laser systems. In this section I will describe the laser systems used in our experiment: near resonant laser systems in the blue (461 nm), red (689 nm), and green (497 nm) as well as a far-detuned high-power system in the infrared (1064 nm) (Figure 2.16).

### 2.3.1 Blue laser system

For most laser cooling techniques closed transitions that are easily accessible with current laser technologies are required. The specific level structure of an atom

Isotope	Natural abundance	Statistics	Nuclear spin
$^{84}\text{Sr}$	0.56%	bosonic	0
$^{86}\text{Sr}$	9.86%	bosonic	0
$^{87}\text{Sr}$	7.00%	fermionic	9/2
$^{88}\text{Sr}$	82.58%	bosonic	0

Table 2.1: Naturally occurring isotopes of strontium [82].

defines the applicable cooling strategy. Sr has a near-closed and strong optical transition at 461 nm from the ground state to the  $^1P_1$  state with a linewidth of  $\Gamma = 2\pi \times 32 \text{ MHz}$ ,<sup>25</sup> corresponding to a large saturation intensity  $I_{\text{sat}} = 43 \text{ mW cm}^{-2}$ . This transition is used in experiments with ultracold Sr for several important applications: reducing the divergence of the atomic beam in the transverse cooling section; decelerating atoms in the Zeeman slower; cooling and trapping of atoms in a magneto-optical trap (MOT) and imaging of trapped atoms.

The saturation intensity of the transition is relatively high. To fully exploit the benefits of the large cycling rate, typical intensities of laser beams for TC, ZS or MOT should be a significant fraction of the saturation intensity.<sup>26</sup> To address a sufficient volume containing atoms the diameter of the laser beams have to be on the centimeter scale, which makes the requirement for laser beams with high intensity difficult to fulfill. In addition these laser beams suffer from unavoidable power loss on elements of the optical system, such as AOMs, required for frequency shifting, or optical fibers, used for mode cleaning and connecting different optical setups. Hence, to provide sufficient intensity for all blue laser cooling beams the source has to produce at least 100 mW. Furthermore, for laser cooling to operate reliably the laser source has to be actively frequency stabilized and the laser linewidth has to be narrower than the linewidth of the addressed transition.

Several options exist for the blue laser source. One option is to use a master oscillator at 922 nm followed by an amplifier and second harmonic generation. This type of laser system is well-developed and easily commercially available. As master oscillator one typically uses a narrow linewidth external-cavity diode laser (ECDL) operating at 922 nm. The light is then amplified to the watt level by a semiconductor

<sup>25</sup>In the literature an alternative value for the linewidth could be found:  $\Gamma = 2\pi \times 30.5 \text{ MHz}$  corresponding to saturation intensity  $I_{\text{sat}} = 40.7 \text{ mW cm}^{-2}$ .

<sup>26</sup>Our MOT laser beams have intensities of  $\sim 0.1 I_{\text{sat}}$ , while intensities of the TC and Zeeman slower are about  $I_{\text{sat}}$ .

tapered amplifier. The amplified light is coupled into a bow-tie cavity containing a non-linear optical crystal for second harmonic generation, which provides a few hundred mW of power at 461 nm.

Another option is to use widely tunable lasers that can be adjusted to produce light at 461 nm [6, 83]. In early experiments with ultracold Sr a typical approach was to use a Titanium-Sapphire laser, operating at 922 nm, in combination with second harmonic generation, which provides more than 1 W at 461 nm. Yet another option is to obtain the 461 nm light by frequency conversion, employing the technique of optical parametric oscillation, which can provide more than 400 mW [84]. The mentioned light sources provide the required power and they are broadly used as reliable laser systems in research with ultracold strontium.

However the option we chose is different still. It makes use of laser diodes operating at 461 nm, which recently became available due to breakthroughs in semiconductor technology [85]. Our laser system uses these diodes as narrow-line, low power, actively frequency stabilized master oscillators and also as slave amplifiers, in order to reach the required power level. The main benefit of the master-slave concept is the lower price compared to the other options. Furthermore, it provides increased flexibility in designing the laser system and expanding it in the future. However there are drawbacks, namely the maximum output power of a single diode, limited to about 100 mW, and poor spectral and spatial mode qualities, which require narrowing the spectral line and its stabilization, beamshaping and mode cleaning. After thorough consideration of the available options, we decided to use the laser diode approach with the primary reason being the lower price.

The advancements in semiconductor technologies continue to widen the range of wavelengths covered by diode lasers. While being an outstanding breakthrough, the currently commercially available blue laser diodes do not completely match our requirements. Laser cooling of Sr needs a wavelength of 461 nm, whereas the closest available laser diodes are only specified to cover 450 to 460 nm. However, upon special request, the producer<sup>27</sup> can preselect the diodes to reach 461 nm. The output power of the diode is about 100 mW. The spatial mode structure of the slave lasers based on this diode is rather poor, therefore we clean the mode by sending the slaves' light through single-mode fibers, losing about 40% of power in the coupling process. A free-running laser diode emits light with a broad spectrum of about 2 nm width, hence for our purpose the linewidth has to be narrowed and the frequency has to be stabilized relative to the Sr transition. To achieve the required improve-

---

<sup>27</sup>Nichia, part number NDB4216E.

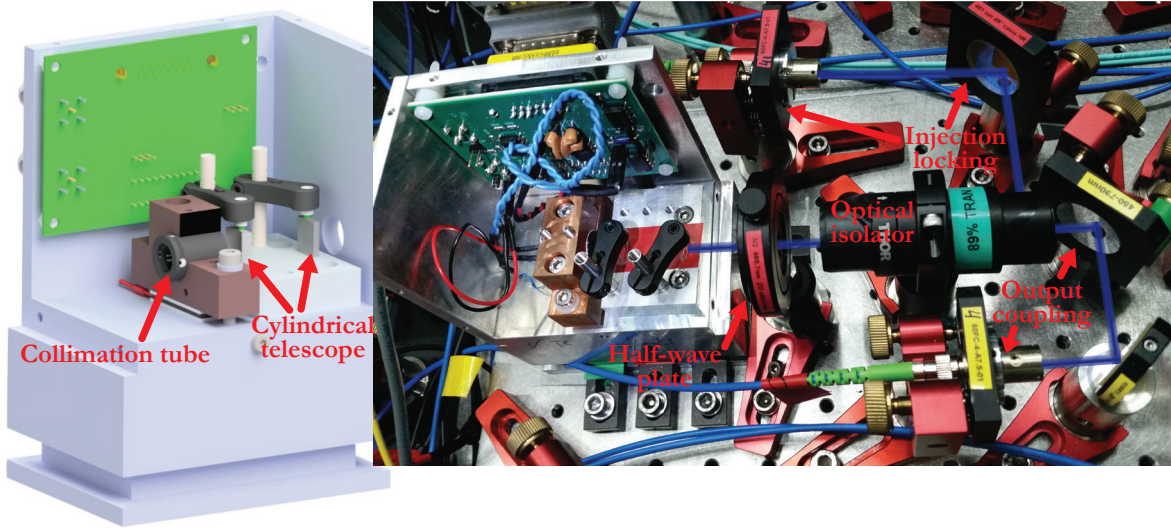


Figure 2.17: Slave laser assembly and injection locking outline.

ments in the spectral properties we use the injection locking technique, by which the slave lasers inherit the spectral characteristics of a master laser [86].

The key principle of the injection locking technique is to transfer the spectral properties of the master laser to the slave lasers. In our lab, we have two lasers that can be used for seeding slaves. The first one is based on a Toptica DL Pro system, a tunable IR diode laser operating at 922 nm, followed by power amplification in a tapered amplifier and frequency doubling. This system is the main laser source for the first Sr experiment in our group, the RbSr experiment. We now use it also as the master for two other Sr experiments in our group, among them the one described here which takes about 1 mW of master laser light. The RbSr laser is locked through saturated absorption spectroscopy to the  $^1S_0 - ^1P_1$  transition of  $^{88}\text{Sr}$ . The second option for the master oscillator is an external cavity diode laser (ECDL) operating at 461 nm, which was built to disentangle the new experiments from the RbSr experiment. This ECDL is designed in Littrow configuration with the same laser diode as used in the slaves. It is locked with a setup analogous to the RbSr master laser. Independent of the master laser choice the slave setup of our experiment starts with about 0.5 mW of light from a master, resonant with the  $^1S_0 - ^1P_1$  transition of  $^{88}\text{Sr}$ .

Details of the slave laser assembly used in our laser systems are shown in Figure 2.17. The output of the laser diode is collimated by an aspheric lens, then shaped by a cylindrical telescope<sup>28</sup> and sent through an optical isolator.<sup>29</sup> The isolator pre-

<sup>28</sup>All parts from Thorlabs. Collimation tube: LT230P-B; aspheric lens C330TMD-A,  $F = 3.1$  mm; cylindrical telescope: LK1753L1-A,  $F = -15$  mm and LJ1402L1-A,  $F = 40$  mm.

<sup>29</sup>Thorlabs Optical Isolator IO-5-460-PBS-HI with about 90 % transmission for 461 nm.

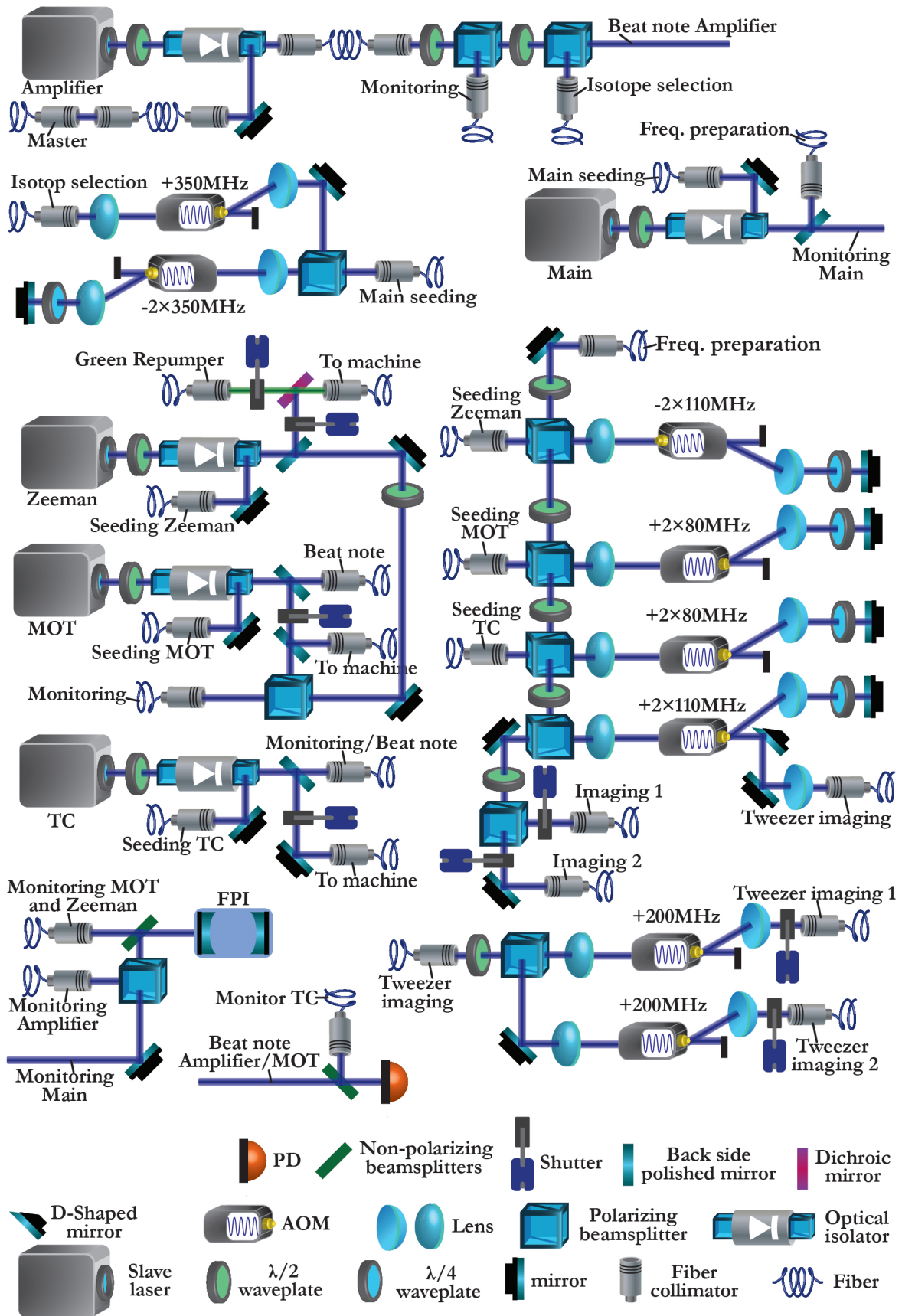


Figure 2.18: Simplified layout of the blue laser system.

vents backreflections from optical elements further down the beam path to reach the laser diode, since those backreflections would compete with the seed light and be detrimental for stable laser operation. The polarizing beamsplitter of the optical isolator that is further away from the diode is used to feed seed light to the diode, with about 0.3 mW necessary for stable locking. We notice an extreme sensitivity of the lock to the mode matching between the slave diode and the seed light and also a strong sensitivity to fluctuations in seed power. To analyze the spectrum of the slaves and control the lock, a scanning Fabry-Perot interferometer (FPI) is used.<sup>30</sup> Monitoring more than four slaves on a single FPI is rather inconvenient. Therefore the fifth slave, dedicated for TC, is monitored with a beat-note or alternatively by registering the fluorescence signal from atoms in the TC section. The absolute maximum output power specified for the laser diodes is 120 mW, but we typically operate below 90 mW in order to hopefully increase the lifetime of the diodes. And indeed we never observed degradation of any slave laser over about three years of operation. Thus it might be that we have been too conservative and could operate safely at a higher power.

We decided to place the laser systems of our experiment on a different optical table from the one used for the vacuum system. Light is transferred from one table to the other through optical fibers.<sup>31</sup> By choosing fiber connections we hope to settle several issues. The spatial mode of the laser beams is improved. The alignment of the optical system is simplified since it can be done separately on each table. The laser system on the laser table can be upgraded without disturbing optics on the vacuum system table. And finally, the ultracold atoms can easily be protected from stray light by placing shutters in front of the fiber inputs and enclosing the laser table in dark cloth.

To provide the required power for our experiment five slaves were built for the blue optical system (Figure 2.18). The master laser provides just enough power for injection locking of one slave, therefore the first slave amplifies light from the master (Figure 2.19). In order to select the Sr isotope the amplified light is frequency shifted by a 350 MHz AOM in double-pass configuration. The double-pass configuration reduces beam motion during frequency changes, which would otherwise result in a frequency dependent light intensity at the output of the subsequent

---

<sup>30</sup>Toptica FPI 100.

<sup>31</sup>We mostly use polarization-maintaining single-mode fibers in our laser systems (Thorlabs, patch cables, panda PM FC/APC, fiber type PM-S405-XP (blue laser system), PM460-HP (green laser system), PM630-HP (red laser system)).

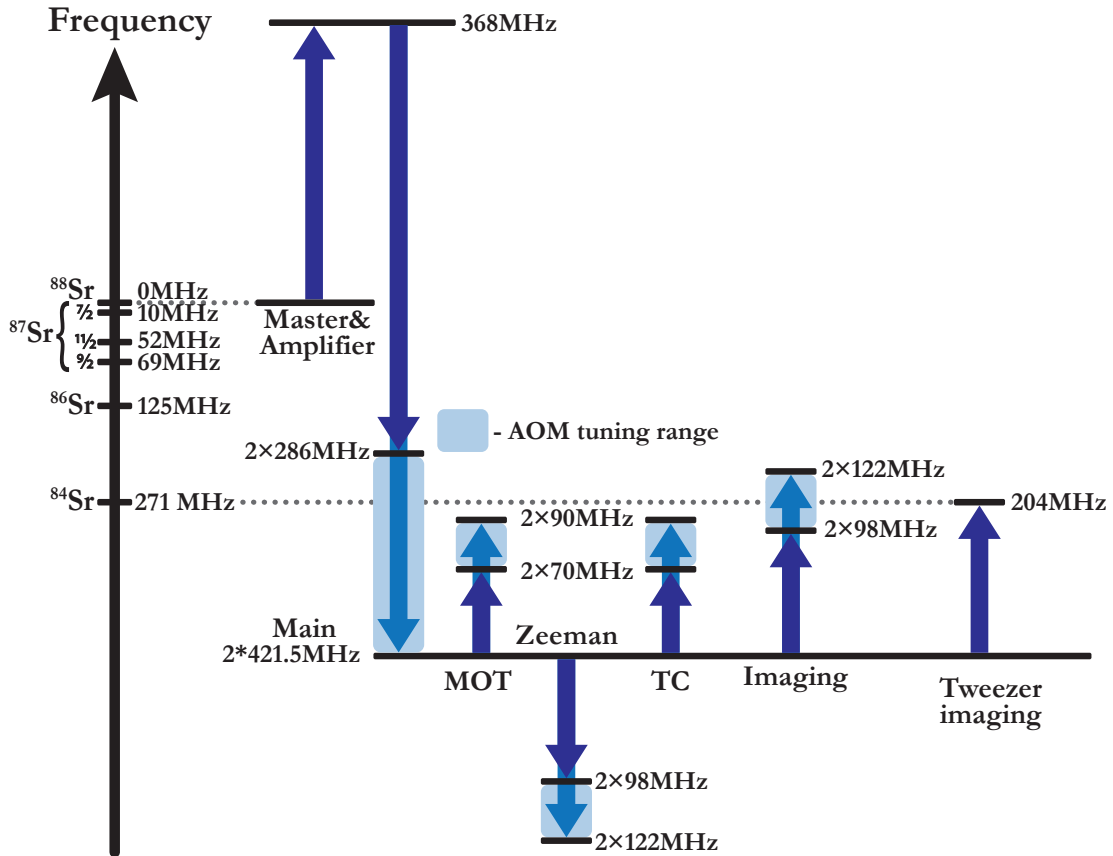


Figure 2.19: Frequency scheme of the blue laser system.

fiber. Such intensity changes can easily break the injection locking of the subsequent slave. This AOM provides a frequency span of 300 MHz, which is sufficient to cover the isotope shift of the  $^1S_0 - ^1P_1$  transition of all stable Sr isotopes. A peculiarity of this setup is that this AOM is aligned to minimize changes in output power when the frequency is shifted, so switching between isotopes does not require additional adjustment. The next slave amplifies light for the chosen isotope (denoted on the figure as Main) and sends it to the frequency preparation stage, composed of six AOMs, with the purpose to prepare light with the required frequencies for imaging and for seeding of the Zeeman slower (ZS), MOT and TC slaves.<sup>32</sup> To have flexibility for the final frequency adjustment, the AOMs preparing seed light are built in double-pass configuration. ZS, MOT and TC light each is prepared by a dedicated AOM and amplified by the dedicated slave. The imaging beam is a low power laser beam and therefore no slave is needed to amplify it.

<sup>32</sup>AOMs, Crystal Technology 3080-120,125,194 (80 MHz); 3110-120 (110 MHz); 3200-121,125 (200 MHz); 3350-199 (350 MHz).

## Absorption imaging

A widely used method to characterize the ultracold atomic cloud is absorption imaging. For absorption imaging a laser beam with a frequency tuned close to the strong  $^1S_0 - ^1P_1$  transition is sent through the atomic cloud. The atoms scatter light, reducing the incident light intensity and casting a shadow in the beam, which is imaged onto a CCD camera, focused on the atomic cloud. The quantity we want to measure is the optical depth  $OD(x, y)$  of the cloud, where  $x$  and  $y$  are two coordinates orthogonal to the propagation direction of the absorption imaging beam. This quantity allows to retrieve characteristics of the atomic cloud, such as the number of atoms, the cloud temperature, its peak density, and so on [87–89]. To calculate the optical depth we take three images. The first is the laser beam with the atomic shadow,  $I_{\text{abs}}$ . The second is a reference image  $I_0$ , recorded with absorption imaging beam, but without atoms. The third is a background image  $I_{\text{bg}}$  recorded without absorption imaging beam and the atomic cloud. From these images we derive the optical depth integrated along the beam direction [87]

$$OD = -\ln \frac{I_{\text{abs}} - I_{\text{bg}}}{I_0 - I_{\text{bg}}}.$$

In our experiment two imaging systems are used to characterize the atomic cloud (see Figure 3.5). They are aligned to take images in the horizontal plane, perpendicular to each other. The magnifications are calibrated by the time-of-flight method: releasing atoms from the trap and measuring the distance that the cloud drops after a certain time. To make an absorption image low intensity laser beams are used. We can reach up to 1 mW of power in these beams corresponding to an intensity of  $0.06I_{\text{sat}}$ , but usually only a fraction of the available power is used.

### 2.3.2 Green laser system

For the efficient operation of the MOT closed atomic transitions are highly valuable as they simplify cooling and trapping. Unfortunately completely closed laser cooling transitions are rather rare among all elements of the periodic table. Usually there are decay channels to one or more dark states. An atom being optically pumped by the cooling light into these states stops interacting with the laser light. Without additional measures these atoms are lost from the MOT. A common solution to this problem is to add repump lasers, which excite atoms from the dark state into states that ultimately decay into the ground state of the cooling transition.

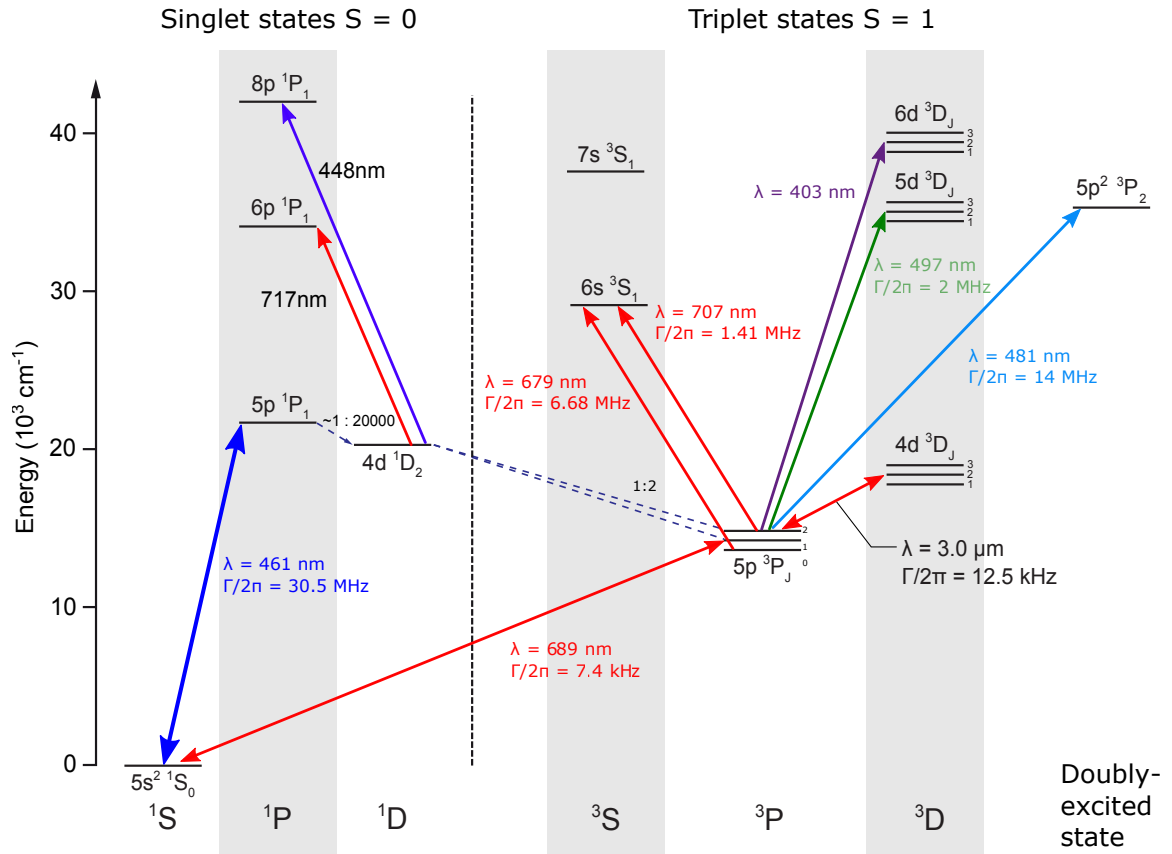


Figure 2.20: Strontium atomic level structure with various options for closing the decay channel from the  $^1P_1$  state [90].

In strontium, laser cooling on the  $^1S_0 - ^1P_1$  transition leads to decay to dark states. The  $^1P_1$  state does not only decay to  $^1S_0$ ; there are weak decay channels from the  $^1P_1$  state with a dominant pathway to  $^1D_2$  and then to the  $^3P_{0,1,2}$  manifold. The  $^3P_2$  state is metastable with a lifetime on the order of minutes, giving rise to a substantial loss from the blue MOT (bMOT) laser cooling cycle. The other two states do not pose a significant problem. The  $^3P_1$  state has a relatively short lifetime of  $21 \ \mu\text{s}$  and atoms decay back to the ground state. The cumulative leakage to the  $^3P_0$  state during the blue magneto-optical trap (bMOT) operation over different trajectories is estimated to be two orders of magnitude smaller than the loss to the other two states of the manifold.

To return atoms back to the cooling cycle from the  $^3P_2$ , optical pumping via various transitions can be used (Figure 2.20). The choice of the transition is primarily guided by the efficiency of returning atoms back to the ground state and the technical challenge to construct a light source at the desire wavelength. For the first experiment in our group, the RbSr experiment, repumping via the  $5s5d \ ^3D_2$  state

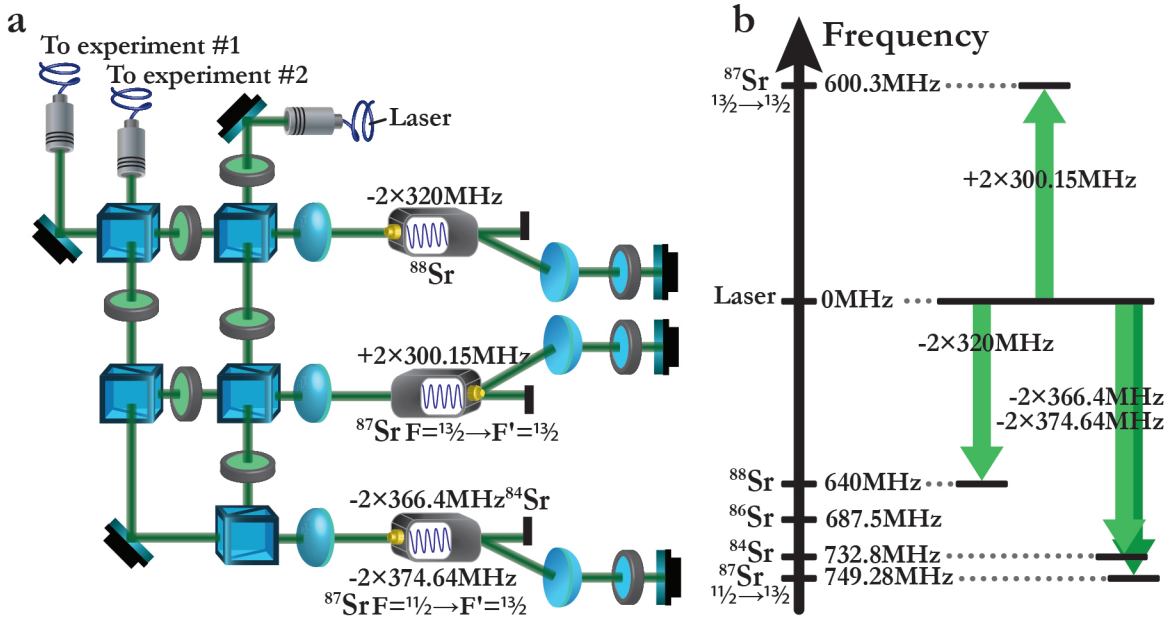


Figure 2.21: a, Simplified layout of the green laser system. b, Frequency scheme of the green laser system.

was chosen [70]. From  $^3D_2$  atoms mostly decay into two states, back to  $^3P_2$  or with a higher probability into  $^3P_1$ , from which they return to the ground state. The requirements for the light source to address the  $^3P_2 - ^3D_2$  transition are relatively modest since the linewidth of the transition is a few MHz and the necessary power for efficient repumping is about  $100 \mu\text{W}$ . The primary complication comes from the technical challenge to generate light at  $497 \text{ nm}$ , although recently laser diodes at this wavelength became available [91]. To produce repump light we use a Toptica SHG laser system, which is based on IR diodes, generating about  $300 \text{ mW}$  at  $994 \text{ nm}$ , followed by a bow-tie cavity for frequency doubling, providing about  $40 \text{ mW}$  if optimized properly. The repump laser beam is sent onto the atoms along the ZS beam path by overlapping repumper and ZS beam on a dichroic mirror.

The properties of the  $^3P_2$  state invite to look at it from a different perspective: it can be a beneficial feature of Sr, rather than just an annoying loss mechanism. The  $^3P_2$  state is a metastable state with a minute scale lifetime. Moreover this state has a large magnetic moment and therefore atoms in the low-field seeking  $m_F$  substates are captured in the magnetic trap that is created by the quadrupole field of the bMOT. This magnetic trap can be used as a reservoir, collecting atoms from the decay channel of the bMOT and it can accumulate 1000 times more atoms than the bMOT [92]. These unique properties allow an alternative approach to the usual continuous repumping of atoms out of dark states. In absence of repump light

atoms from the bMOT continuously leak into the reservoir, where they accumulate. Once enough atoms have been accumulated a short pulse of repump light brings them back to the ground state, where they are captured by the next trapping stage, a red magneto-optical trap (rMOT) operating at a wavelength of 689 nm [92], see Section 3.3.2.

For our experiment we use the reservoir strategy instead of continuous repumping. An advantage of this strategy is that the repumper is only needed for a few tens of milliseconds during the seconds long experimental cycle, thus one repump laser can be conveniently shared by several experiments.<sup>33</sup> Another advantage is to enable consecutive accumulation of different Sr isotopes in the reservoir using only one blue laser system. To repump all Sr isotopes or various isotopic mixtures, the repump laser system can create the frequencies necessary to address all isotopes using several AOMs, as shown in Figure 2.21. The lowest AOM in the figure is used either for  $^{84}\text{Sr}$  or one of the  $^{87}\text{Sr}$  transitions, in dependence on the isotope required for the experiment. We use around 100  $\mu\text{W}$  per required frequency component on the vacuum system table. Working with the fermionic isotope is more complicated because of its hyperfine structure, which doesn't exist in bosons and which leads to a large splitting of the  $^3P_2$  state, on the order of GHz. We expect that atoms in the reservoir mostly populate the  $F = 13/2$  and  $F = 11/2$  substates, therefore our repumping scheme only addresses these transitions [92].

### 2.3.3 Red laser system

One of the valuable features of the Sr level structure is the narrow linewidth of the  $^1S_0 - ^3P_1$  transition ( $\Gamma = 2\pi \times 7.4\text{kHz}$ ). Having the ability to laser cool using this narrow transition is highly advantageous since the Doppler temperature is proportional to the linewidth of the laser cooling transition. A challenge compared to MHz-line laser cooling is that the frequency stability of the laser source has to be much higher: the linewidth and the long-term frequency drift have to be less than the transition linewidth. A nice aspect of the narrow linewidth is the low saturation intensity of  $I_{\text{sat}}=3\ \mu\text{W cm}^{-2}$ . This aspect combined with readily available and af-

<sup>33</sup>We usually work only with one isotope at a time, but because of the specific implementation of our repump light sharing we receive light for the isotopes used by the RbSr experiment. This circumstance does not cause problems since additional frequency components do not decrease the efficiency of the repumping process and since blue and red laser systems operate selectively for a chosen isotope.

fordable laser diodes and even tapered amplifiers<sup>34</sup> at 689 nm make it easy to create laser beams at the saturation intensity level.

The requirements on the power of the light source and its stability for the red laser system are in a vivid contrast to the blue laser system, which addresses the broad Sr transition. For the blue system the primary challenge is to construct a powerful system with a reasonable price per photon, whereas the frequency is trivial to stabilize.

A well developed approach to build the red laser system, which we adopt here, is to use a master-slave setup, similarly to the blue laser system. Typically the master laser is an ECDL that is reduced in linewidth and carefully stabilized to the correct wavelength. A common method to reduce the linewidth to the kHz level is locking of the laser to a high-finesse optical cavity. The state-of-the-art in the field of atomic clocks is a linewidth of about 10 mHz [93] and systems with linewidth below 1 Hz are even commercially available.<sup>35</sup> The short-term stability of such systems is determined by the properties of the cavity. To suppress the slow frequency drift of the cavity the laser can additionally be referenced to an atomic or molecular transition or a frequency comb.

The first experiment in our group (the RbSr experiment) uses an ECDL from Toptica (DL Pro) as a red laser system master. This laser is locked to a cavity with a finesse of about 15 000 and the cavity length is stabilized onto the time-averaged signal of a strontium spectroscopy cell [70], similar to the one used in the blue setup. This master laser is now used for all red laser systems in our group and provides our experiment with a few hundred  $\mu\text{W}$  of light, blue shifted by 80 MHz from the  $^{88}\text{Sr}$  transition.<sup>36</sup> This power is sufficient to seed the first slave, which becomes the basis for the frequency generation stage (Figure 2.22). The frequency generation stage is composed of seven AOMs, preparing light for the experiment, primarily to address the three bosonic isotopes and three transitions of the fermionic isotope (Figure 2.23). To amplify the generated light we use three additional slave lasers. Depending on the goals of our research the roles of these slaves can be quickly changed by modifying the frequency of the seed light. Therefore by swapping fibers with seed light they become amplifiers of light around 689 nm for various purposes, for instance addressing transitions of different isotopes, creating laser beams for

---

<sup>34</sup>For instance Eagleyard Photonics part number EYP-TPA-0690-00500-2003-CMT02-0000 provides an output power of about 0.5 W.

<sup>35</sup>For example from Menlo Systems or Stable Laser Systems.

<sup>36</sup>The light from each amplifying slave is sent through an 80 MHz AOM and the  $-1$  order is sent to the atoms, compensating the frequency shift of the master laser.

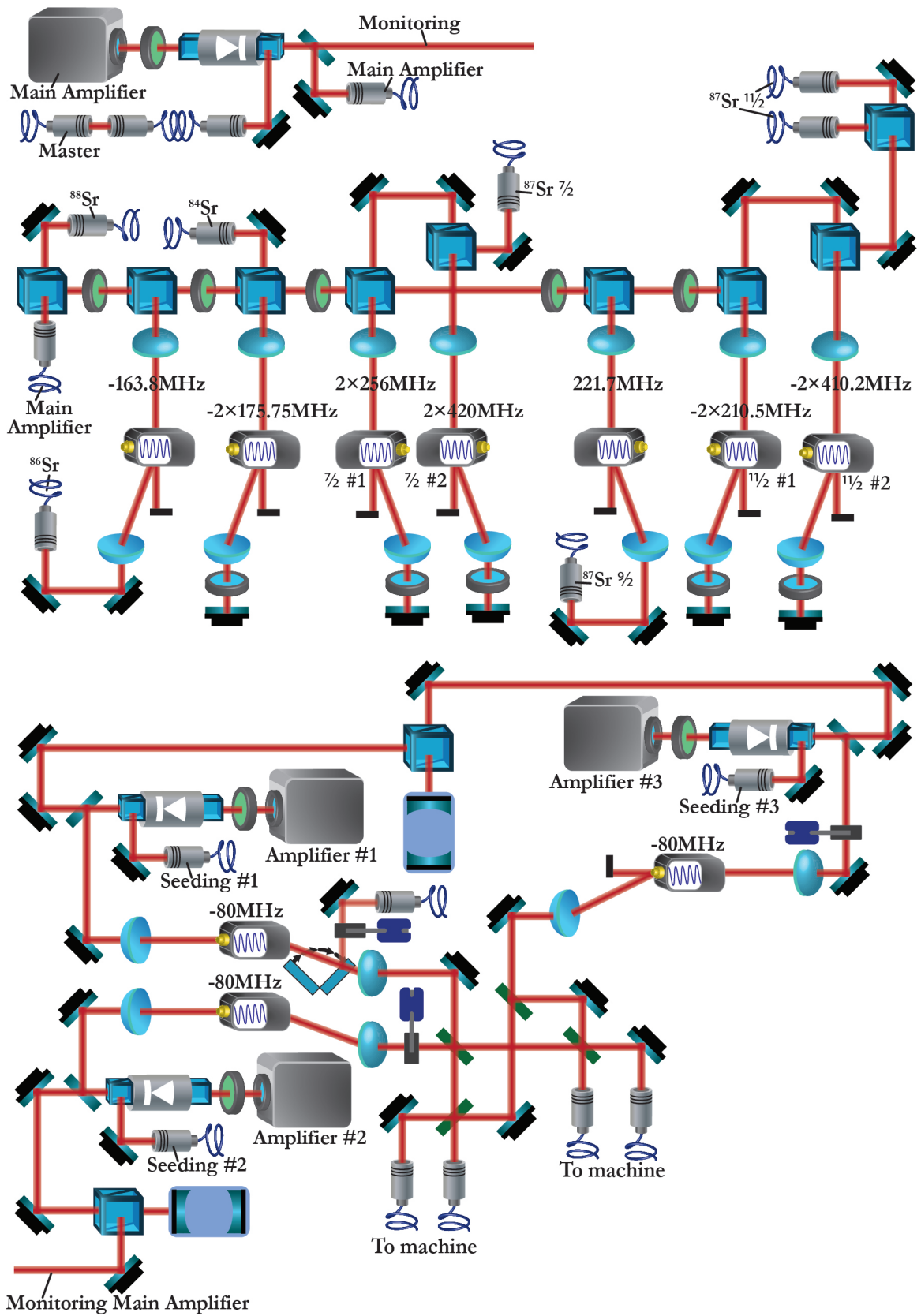


Figure 2.22: Simplified layout of the red laser system.

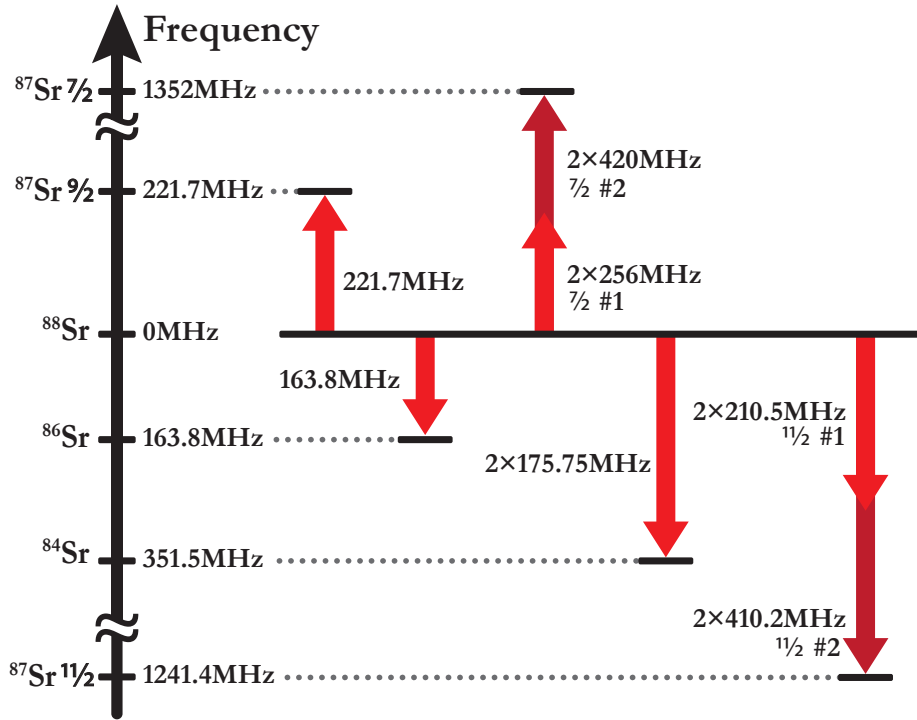


Figure 2.23: Frequency scheme of the red laser system.

optical Stern-Gerlach technique or absorption imaging with the red transition. The light from each amplifying slave is coupled to 80 MHz AOMs to generate sidebands for the rMOT (red magneto-optical trap) and also to quickly switch off the light, in contrast to the blue system, where simply mechanical shutters are used for that task.<sup>37</sup>

To prepare light for the rMOT, beams from the three slaves are combined on a system of non-polarizing beamsplitters. The combined beams are then sent through optical fibers from the laser system optical table to the vacuum system table. For this work all rMOT laser beams are retro-reflected, while we have the option to use separate beam paths for the vertical rMOT beams. We use three (or, in the case of individual vertical beams, four) fibers to transport the rMOT light between tables. The power of each rMOT beam can be controlled by half-wave plates and polarizing beamsplitters placed after the fibers (see Figure 3.5). The fiber coupling is aligned to obtain similar powers on the vacuum system table for each slave. Often only one

<sup>37</sup>Simply using shutters for the blue beams is possible because atoms are accumulated in the reservoir, making it irrelevant to control the duration of the bMOT precisely. Since the lifetime of the reservoir is about 30 s [94] jitter on the millisecond scale between switch off of the bMOT and re-pumping is also irrelevant. The main benefit of using shutters instead of AOMs is that we avoid losses due to the finite efficiency of AOMs.

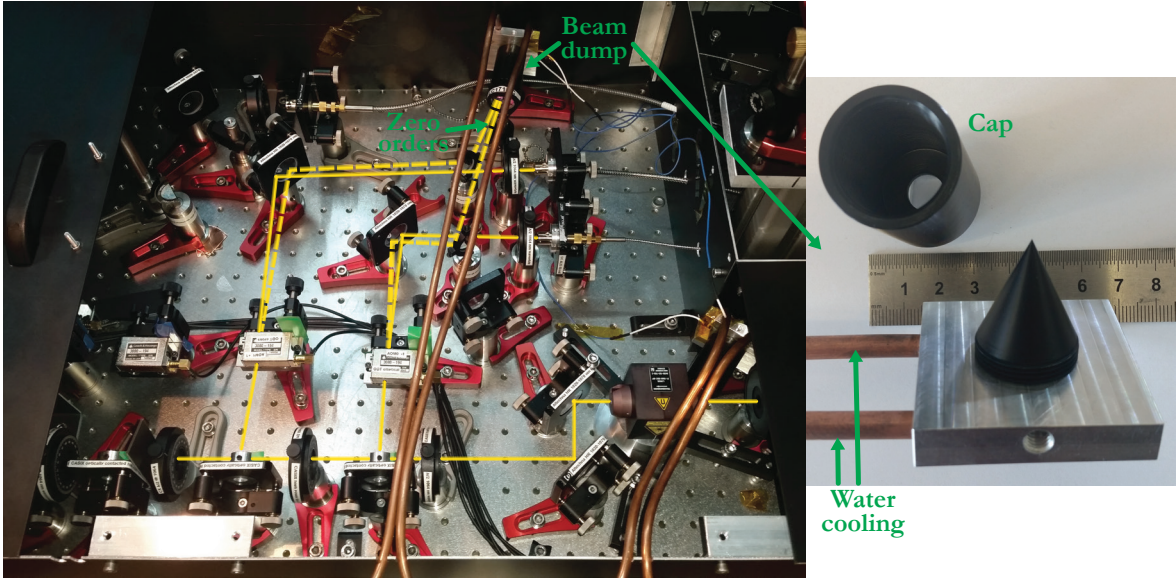


Figure 2.24: Optical setup of the infrared laser system, with the beam dump assembly shown on the right.

or two slaves are needed for a given experiment. For instance to produce a BEC of  $^{84}\text{Sr}$  only one slave is required and only two for a DFG of  $^{87}\text{Sr}$ . The third slave is important to produce Bose-Fermi mixtures or for nuclear spin state detection using the optical Stern-Gerlach technique [95]. Each slave produces about 30 mW of power<sup>38</sup> and for the injection locking we use typically about 100  $\mu\text{W}$ . More details about the red laser system are described in the PhD thesis of Oleksiy Onishchenko.

### 2.3.4 Infrared laser system

The final trapping stage on the road to quantum degeneracy is the confinement of atoms in an optical dipole trap (ODT), which is an essential tool for experiments with ultracold Sr. High power lasers at a frequency far-detuned from atomic resonances are commonly used to create a sufficiently deep trap, while suppressing the off-resonant scattering of photons. We use a crossed-beam ODT, consisting of two focused laser beams crossing at an angle, to strongly confine atoms in all three dimensions.

To generate light for the trap we use a laser source at 1064 nm with an output power of 45 W.<sup>39</sup> The output of the laser is coupled to a system of AOMs to prepare

<sup>38</sup>Laser Diode: HL6738MG.

<sup>39</sup>AZUR LIGHT systems; linewidth below 50 kHz and  $M^2 < 1.1$ .

several optical beams for the experiment.<sup>40</sup> Using AOMs provides the necessary control over intensities and also allows to rapidly switch the light.<sup>41</sup> To avoid the creation of interference patterns between the two laser beams of the ODT in the trap region each of the beams is prepared by an individual 80 MHz AOM, which are operated in opposite orders. The 160 MHz frequency difference between the two beams results in rapidly moving interference patterns. The atoms cannot follow this pattern and effectively explore a time-averaged potential.

When working with high-power lasers the safe handling of laser beams is strictly required since even a small percentage of reflected light can be dangerous. Even anti-reflection coating of the optical elements and vacuum windows does not eliminate this problem since coatings are never perfect. The entire IR laser system is located on the vacuum system table and for safety reasons it is placed in a box, made from anodized aluminum (Figure 2.24). The laser beams after the AOMs are coupled to fibers,<sup>42</sup> which bring light to the breadboards around the vacuum chamber. To safely block high power beams we use water cooled beam dumps. The design of the beam dumps is shown in the Figure 2.24.

## 2.4 Magnetic field control

One of the essential elements of experiments with ultracold quantum gases are magnetic fields. They are crucial for many tasks: decelerating atoms in the Zeeman slower, trapping atoms in the MOTs and magnetic traps, inducing the splitting of magnetic sublevels; guiding the orientation of the atomic magnetic moments and more. In this section I describe the magnetic field coils used in our apparatus to control the magnetic field.

### **Zeeman slower**

We use a Zeeman slower (ZS) to decelerate the atomic beam effusing from the oven. Most atoms in this beam have a velocity of several hundred m/s, which is too fast to be captured directly into the bMOT. The ZS decelerates atoms from up to 500 m/s down to about 20 m/s, allowing efficient loading of atoms into the bMOT. The radi-

---

<sup>40</sup>An optical isolator is used to prevent the detrimental effect of back reflections on the power and spectral stability of the laser. LINOS, part number: FI-1060-3SC BP.

<sup>41</sup>For the crossed-beam optical dipole trap we use only two AOMs out of six that are available.

<sup>42</sup>OzOptics single-mode, polarization-maintaining fibers with end cap option A3AHPC to increase the range of applicable powers.

ation force created by a laser beam counter-propagating to the atomic beam is used to slow atoms. The frequency of the laser beam needs to be kept in resonance with the frequency of the atomic transition in order to sustain a high scattering rate of photons. While the atoms are decelerated, the Doppler shift changes much more than the linewidth of any Sr transition and atoms can leave the slowing process before the target velocity is reached. The Zeeman slower overcomes this difficulty by compensating the changing Doppler shift with a changing Zeeman shift. The spatial variation of the Zeeman shift needs to be tailored to match the variation of the Doppler shift along the atomic trajectory from the oven to the main chamber.

Our Zeeman slower magnetic field has the "midfield zero" magnetic field configuration (also known as "spin flip" configuration). The field is always oriented parallel to the atomic beam direction, but its sign changes at one point along the length of the slower (Figure 2.25). The magnetic field profile is designed to operate with the slower laser beam, which has a large frequency detuning of 434 MHz below the  $^1S_0 - ^1P_1$  transition. This detuning maintains effective atom-light interaction at the zero crossing point, i.e. at zero magnetic field, where atoms have a velocity of about 200 m/s. This large value of the detuning is chosen to avoid pushing atoms out of the bMOT, since the slower beam intersects with the bMOT, which contains slow atoms at a magnetic field close to zero. Our slower is designed to maintain a constant deceleration  $\eta a_{\max}$ , created by the radiation pressure force along the atomic trajectory [96]. The targeted deceleration is reduced by the design parameter  $\eta$  compared to the maximum value

$$a_{\max} = \frac{\hbar k \Gamma}{m \cdot 2},$$

originating from the maximum photon scattering rate. Here  $k$  is the light field wave vector,  $m$  is the atomic mass of strontium and  $\Gamma$  is the transition linewidth [97]. The parameter  $\eta$  accounts for imperfections in the deceleration process such as deviations of the actual magnetic field from the designed field, limited available laser power and inhomogeneous spatial distribution of the light intensity in the laser beam. A smaller  $\eta$  allows to obtain a better stability of the slowing process, however the slowing distance

$$l = m \frac{v_F^2 - v_I^2}{\eta \hbar k \Gamma}$$

is increased proportionally. Here  $v_F$  and  $v_I$  are initial and final velocities of an atom during the deceleration [97]. The primary objective for the design of our Zeeman slower is to obtain a high atomic flux of atoms that can be captured in the MOT and assured operation even with lower than expected beam power or magnetic field

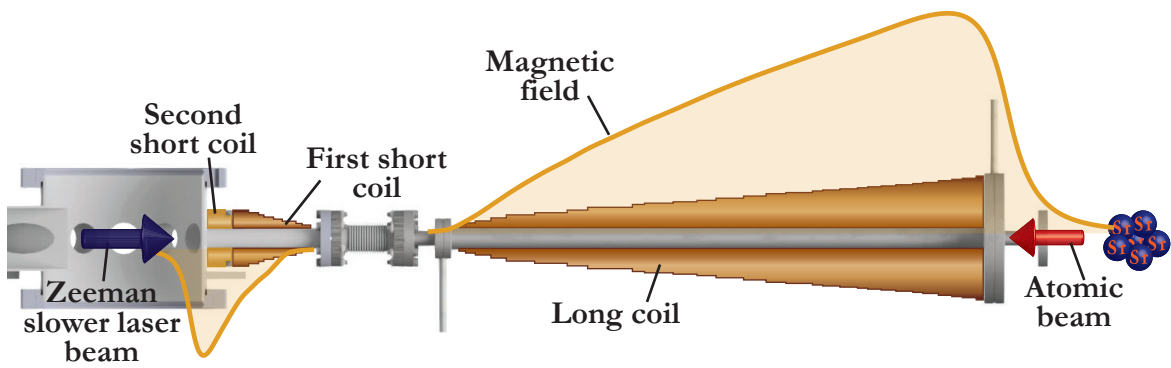
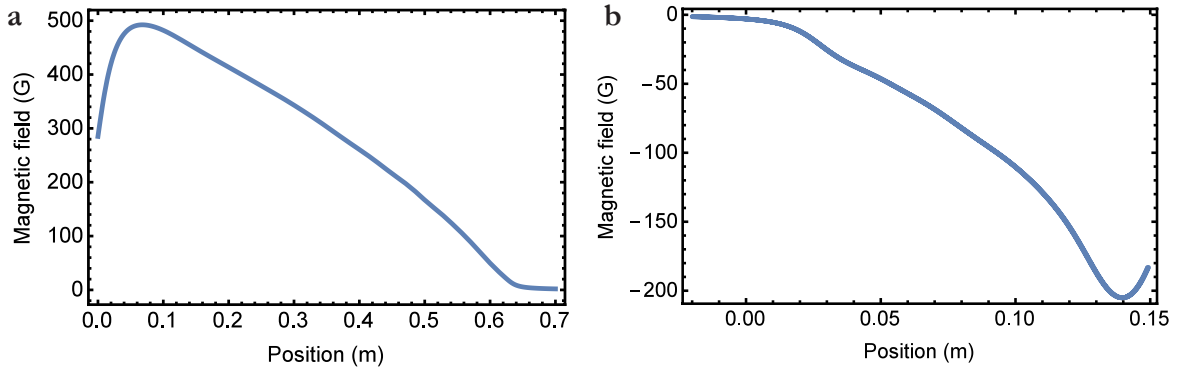


Figure 2.25: Schematic representation of the Zeeman slower.

profile that is not perfectly smooth, with less importance given to minimizing ZS size and weight. Thus in our experiment the targeted  $\eta$  is relatively low: 0.2 for the long coil and 0.15 for the short coils.

The profile of the magnetic field is created by three coils: a long coil and two short coils, responsible for the field with opposite sign (Figure 2.26).<sup>43</sup> The long coil is wound on a dedicated water-cooled vacuum tube (see Figure 2.6) while the two other coils are wound on the long arm of the main vacuum chamber. The reason for splitting the second part of the Zeeman slower into two coils is the requirement for an abrupt slope of the magnetic field at the slower output. An additional constraint for the design of the short coils is limited space between the chamber's arms, forcing us to build compact coils with a small number of windings, but using high current. To achieve the required field while keeping the construction compact, two different types of wires are used with different specified maximum current. A flat enameled copper wire (1.15 mm×4.67 mm) is used for the long coil and the first short coil and send currents through them are 5 A and 7 A respectively. The number of coil turns in each layer of the long coil are {134, 132, 129, 127, 125, 123, 121, 119, 116, 114, 112, 107, 105, 104, 102, 96, 94, 91, 89, 84, 81, 77, 75, 72, 68, 64, 62, 56, 53, 49, 44, 42, 36, 32, 30, 26, 24, 22, 21, 14, 11, 10, 9, 8, 7, 6, 5, 4}, where all layers start on the oven side of the slower. For the first short coil the layer winding numbers are {22, 21, 16, 12, 10, 6, 4, 2}, where the layers start on the MOT side, next to the second short coil. This second short coil is built with round water-cooled copper tubing with 6 mm outer diameter, operated at 82 A. The water cooled coil is the closest to the MOT location of all coils, touching the body of the main chamber. It is wound

<sup>43</sup>The magnetic field produced by the short part of the Zeeman slower was measured and it corresponds to the expected calculated profile. We did not measure the field of the long coil and rely only on its calculation.



**Figure 2.26: Calculated magnetic field profiles produced by the Zeeman slower coils: a, Long coil. b, Two short coils.**

around the chamber arm as two layers with five and three turns. The current in each coil was optimized on the atom number in the bMOT.

### MOT coils

An essential part of the MOT and the magnetic trap is a quadrupole magnetic field, generated in our experiment by the MOT coils. The MOT coils are a pair of coils that are placed inside the reentrant windows on the main chamber. In addition to creating a quadrupole field these coils can generate a bias field by switching the current direction in one of the coils. The capability to produce large bias fields is important for future research, for instance to split the magnetic substates of the  $^{87}\text{Sr}$  ground state or to broaden the ultranarrow clock transition for bosonic Sr.

The coils are designed and assembled in accordance with the constraints of the vacuum system and the requirements of the experiment. The goal is to achieve up to 1000 G for the bias field and about 200 G/cm for the quadrupole field. So far in the experiment we have only used a quadrupole field with a maximum gradient of about 80 G/cm for the bMOT.

The main constraints of the design are the dimensions of the reentrant windows, which set the boundaries for the inner and outer coil diameters (Figure 2.27). The coils have few windings in order to reduce their inductance and a high current is used to reach the required field. They are made from copper tubes that are water cooled to efficiently remove the resistive heat. To manufacture the coils annealed square hollow copper tubing was chosen with an outside dimension of 6 mm and an inside dimension of 3 mm. Each coil is assembled from three nested barrels with sequentially increasing diameter. Each barrel has two turns in the horizontal direction and eight turns in the vertical direction. The inner diameter of the assembled

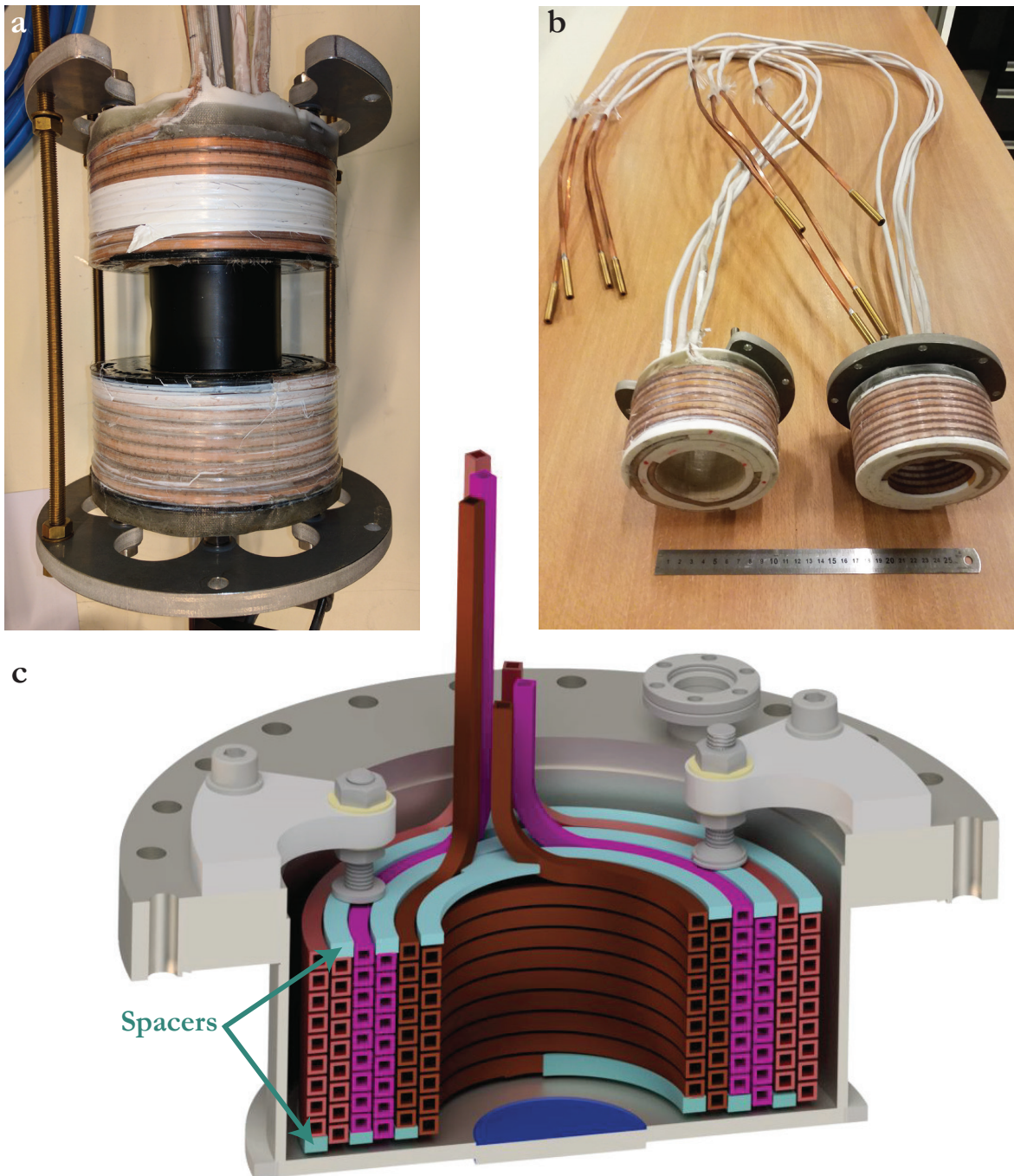


**Figure 2.27: Design and pictures of the constructed coils for the main and science chambers.** **a**, Assembled and prepared for testing MOT coils before installation on the vacuum system. **b**, Science chamber coils. **c**, CAD drawing of the top MOT coil and the reentrant window, shown in a cutaway view. The spacers are used to fill gaps, created by changing layers between horizontal turns.

coil is 71 mm and the outer diameter is 147 mm. The surfaces of the two coils facing each other have an estimated distance of 61 mm when installed on the apparatus. The magnetic field produced by the coil pair was tested before installation on the vacuum system. The measured magnetic field in the bias configuration is about  $3.8 \text{ GA}^{-1}$  at the center of the assembly. The field gradient in the quadrupole configuration is about  $1 \text{ GA}^{-1} \text{ cm}^{-1}$  along the coil axis. The resistances of the coils are  $15.9 \text{ m}\Omega$  and  $17.7 \text{ m}\Omega$ , and the inductances are  $170.5 \text{ }\mu\text{H}$  and  $170.8 \text{ }\mu\text{H}$ .

When using a water cooled device one has to be concerned about leaks in the cooling system, which might lead to spraying water over sensitive parts of the machine. Especially prone to failure are the connections between copper and plastic tubes, which are unavoidable in our design to electrically insulate different water cooling circuits. We place these connections below the level of the optical table, greatly reducing the danger of damaging the equipment. Each coil barrel is wound such that it has a one meter long tube left as a connection lead. The ends of these tubes are soldered into short brass fittings, connecting tubes with square and round profiles. The round tube then leads to the side of the vacuum table, where it is connected to plastic pipes. The six barrels are connected to the water cooling system in parallel to provide efficient cooling, whereas the three barrels of each coil are electrically connected in series. Currently we use only one power supply for the MOT coils, but in principle the leads of each barrel could be connected separately to independent power supplies to improve control over the magnetic field.

An important characteristic of the coils and their driving circuit is the switching time between the gradients needed for the bMOT and the rMOT. A short switching time is required for an efficient transfer of atoms from the reservoir to the rMOT. Currently we simply rely on the power supply to change the magnetic field. The typical timescale on which the magnetic field changes from  $65 \text{ G/cm}$  to  $5 \text{ G/cm}$  is  $\sim 35 \text{ ms}$ . This rather long duration is the result of significant energy stored in the electromagnetic field and the limited ability of the electronic circuit to dissipate this energy. A more elaborate circuit, e.g. using high voltage IGBT switches, would reduce the switching duration, which might improve the transfer efficiency [98, 99].

We prepared a second pair of coils for the science chamber, designed and constructed in a similar way to the MOT coils. The primary difference of the second pair is a more compact style since the size of the reentrant windows on the science chamber is smaller than the ones on the main chamber. To achieve the smaller size the coils are constructed from two barrels instead of three. Analogously to the MOT coils each barrel has two turns in the horizontal direction and eight turns in the

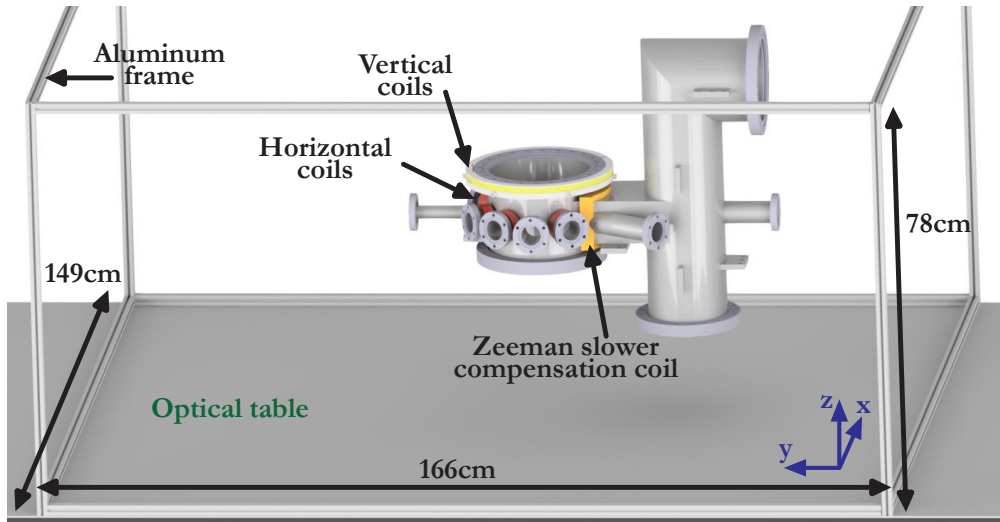


**Figure 2.28: Locations of the compensation coils on the apparatus.** To give a clear view, most elements of the apparatus are omitted, except the main chamber and the optical table.

vertical direction of the same hollow copper tube as used for the MOT coils.

### Low field coils

Our experiment requires precise control over the bias magnetic field at the location of the MOTs. For example we need to be able to null the magnetic field to perform the spectroscopy measurements. We also need to apply a small magnetic field in a well-defined direction to precisely overlap the rMOT with the dipole trap. To achieve this control, we need to compensate external magnetic field sources, such as the earth magnetic field, ion pump magnet fields or fields created by neighboring experiments.

In order to achieve fine control over the magnetic field at the trap location several small coils are installed on the apparatus to produce a low field up to 10 G. All installed low field coils are hand-wound with circular profile enameled copper wire and we limit the maximum current of each coil to 10 A to prevent overheating.

To compensate the residual field at the MOT location we used three orthogonal pairs of coils, which are wound on a large aluminum frame, placed around the vacuum system (Figure 2.28). Each coil of the frame has ten turns of round enameled copper wire. The frame has a relatively large size for several reasons. The large coils generate an almost homogeneous field at the trap location and inductive coupling to the coils in the MOT region is relatively small. Furthermore the large frames barely restrict the access to the vacuum chamber. The downside of the large size is a relatively weak magnetic field produced at the trap location of 34 mG/A, 40 mG/A,

144 mG/A for the two horizontal and the vertical coil pairs respectively.

Additionally a versatile set of coils is installed on the main chamber to apply weak magnetic fields for various purposes, for instance to guide the orientation of atomic magnetic moments, to induce a small Zeeman splitting between states, to generate an offset field for the optical Stern-Gerlach technique or to move the rMOT from the center of the vacuum chamber to the focal plane of the microscope objective. Six coils are installed on arms of the main chamber to control the magnetic field component in the horizontal plane. Two coils are wound on a frame that is attached to the top flange of the main chamber in order to add a field along the vertical axis.

Another low field coil is used to compensate the residual magnetic field of the Zeeman slower at the MOT location, which is still a few Gauss despite the sharp drop in ZS field after the last ZS coil and the distance of about 100 mm between that coil and the MOT location. To cancel this residual field a compensation coil is wound on the main chamber duct, on the opposite side to the Zeeman slower (Figure 2.28).

# Chapter 3

## Obtaining quantum degenerate gases

The primary objects of study in our research are ultracold strontium clouds, confined in a trap. Specific features of strontium atoms facilitate achieving quantum degeneracy, but also create challenges to overcome. In this section I describe details of the experimental steps that we take to bring thermal gases to degeneracy: transverse cooling, Zeeman slowing, magneto-optical trapping using the broad blue transition at 461 nm (bMOT) and the narrow red transition at 689 nm (rMOT), dipole trapping and evaporative cooling to Bose-Einstein condensation and Fermi degeneracy.

### 3.1 Transverse cooling

The divergence of the atomic beam emerging from the oven influences the fraction of atoms reaching the main chamber, which in turn has an effect on the maximum number of atoms in the bMOT. In order to use the Sr in the oven efficiently the divergence of the effused atomic beam needs to be reduced. Transverse cooling is one of the broadly used techniques to collimate atomic beams, and over the years has become a standard approach in ultracold gas experiments.

Transversal cooling (TC) is based on an optical molasses, using red detuned laser beams propagating transversally to the atomic beam. These beams create a radiation pressure force that reduces the transversal velocity component. To collimate atoms into a beam directed to the main chamber, laser beams are aligned in a plane perpendicular to the atomic beam and directed in the vertical and horizontal directions (Figure 3.1). The laser beams are retro-reflected in order to better use the limited available power. To increase the duration of the atom-light interaction while the atoms are passing through the TC section the beams are expanded into an elliptical

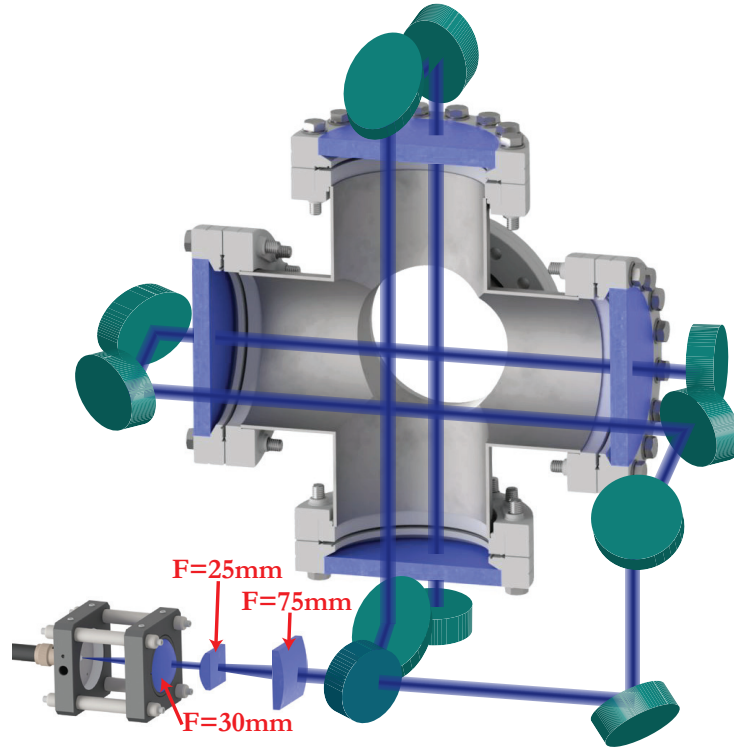


**Figure 3.1: Outline of the transverse cooling section with simplified optical setup.** Two vacuum tees with pumps on the sides are removed on the figure for clarity.

shape by a cylindrical telescope resulting in a Gaussian beam with waists of  $2.4 \text{ mm} \times 7.1 \text{ mm}$ .<sup>1</sup> The major axis of the ellipse is oriented along the propagation direction of the atomic beam. Furthermore, the laser beams are arranged in a double-pass geometry to double the length of the atom-light interaction. The total power used for transverse cooling is 32 mW and it is generated by a dedicated slave in the blue laser system. As required for the laser cooling the light's frequency is shifted below the  $^1S_0 - ^1P_1$  transition by  $44 \text{ MHz} \sim 1.5\Gamma$ . The relatively broad linewidth of the transition of 32 MHz is advantageous for transversal cooling since the maximum achievable radiation pressure force is proportional to the linewidth. The collimation could be improved by adding another slave and increasing the number of passes through the vacuum chamber to fully exploit the DN100CF viewport size.

<sup>1</sup>Throughout this thesis the size of a Gaussian beam is defined by the size at an intensity level of  $1/e^2$  from the intensity in the beam center. The Gaussian intensity distribution is

$$I = I_0 e^{-\frac{2x^2}{\omega_x^2}} e^{-\frac{2y^2}{\omega_y^2}},$$

where  $\omega_{x,y}$  is the beam waists.

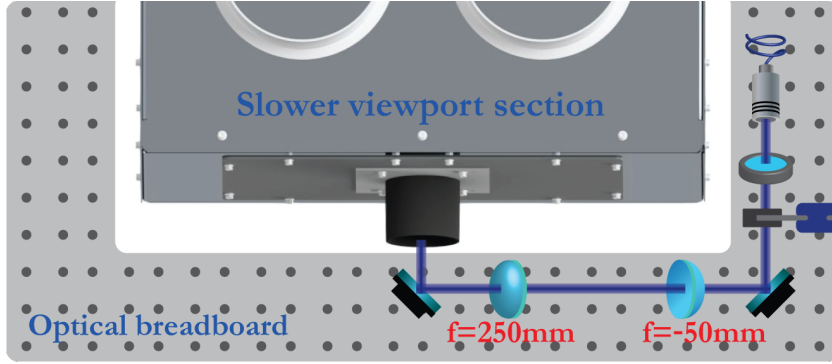


Figure 3.2: Simplified optical setup to shape the Zeeman slower laser beam and send it into the vacuum system.

## 3.2 Zeeman slowing

The next stage in the experimental cycle is the deceleration of the atoms to a velocity below the capture velocity of the MOT. Over the years several deceleration methods have been developed and the most common technique nowadays is the Zeeman slower. It decelerates atoms through the radiation pressure force exerted on the atoms by a laser beam that is counter propagating to the atomic beam. The Zeeman shift of the laser cooling transition created by a spatially varying magnetic field is used to compensate the changing Doppler shift as atoms are slowed down. Doppler and Zeeman shifts compensate each other throughout the slower, keeping the slowing laser on resonance with the atomic transition.

For the Zeeman slower laser beam it is natural to choose the strong  $^1S_0 - ^1P_1$  transition because of its relatively broad linewidth, which is beneficial for obtaining a large scattering rate.<sup>2</sup> The slower laser beam overlaps with the MOT and therefore can create a radiation pressure force on the trapped atoms. To minimize the negative impact on the MOT the Zeeman slower was designed to operate with a laser beam detuned by  $434\text{ MHz} \sim 14\Gamma$  below the resonance. The power of the laser beam is 33 mW, provided by a dedicated slave in the blue laser system. The slower laser beam is prepared on a specially shaped optical breadboard that is located near the slower viewport vacuum section (Figure 3.2). From the fiber output collimator the beam is sent through a quarter-wave plate, expanded by a spherical telescope to a waist of 6.2 mm and finally sent through the vacuum viewport against the atomic beam. By adjusting the distance between lenses of the telescope the laser beam is

<sup>2</sup>As was mentioned in the repumping section the  $^1S_0 - ^1P_1$  transition is not entirely closed, therefore leakage channels limit the maximum number of scattered photons.

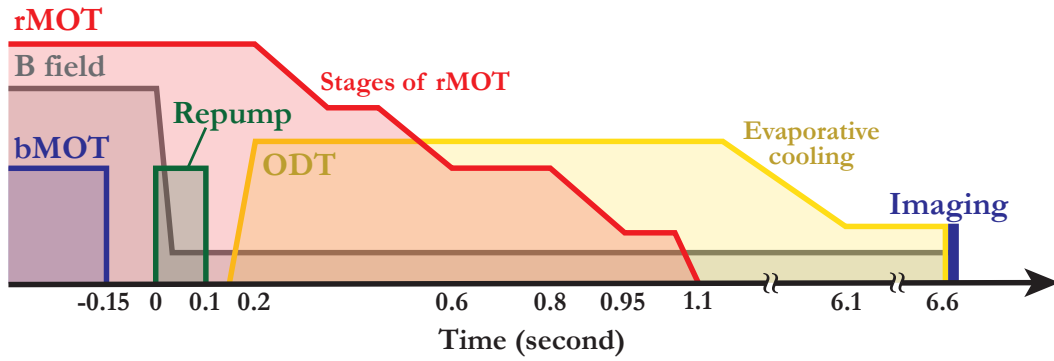


**Figure 3.3: Typical timing diagram of the experimental cycle.** The magnitude of the quadrupole magnetic field gradient used for the MOTs is shown in gray. All other quantities are intensities of the relevant laser beams involved in the indicated experimental steps. During the bMOT operation atoms are accumulated in the metastable reservoir and the accumulation stage can last for many seconds. The details of the diagram vary in dependence of the goals of the experimental sequence. Different arbitrary scales are used for each quantity.

made slightly convergent onto the oven nozzle to compensate for the divergence of the atomic beam.

### 3.3 Magneto-optical traps

A core part of most experiments with ultracold gases is a magneto-optical trap (MOT), cooling atoms to the ultracold regime and confining them into a small region. Over the years, with enhancements of laser technology and ingenious experimental ideas, many chemical elements and even molecules have been trapped and cooled in MOTs. In our experiment we employ two MOT stages, which sequentially bring decelerated atoms from the Zeeman slower closer to degeneracy. In the following paragraphs I will describe details of the MOTs realized in our experiment.

#### 3.3.1 Blue MOT

The first trapping stage in our experiment is the MOT operating on the strong  $^1S_0 - ^1P_1$  transition, loaded with atoms decelerated by the Zeeman slower (Figure 3.3). It uses the standard configuration of three orthogonal laser beams, retro-reflected to obtain counter-propagating beams and circularly polarized by quarter-wave plates (Figure 3.4). The total power used for the bMOT is 25 mW, which is split into three

beams, two horizontal and one vertical, with a ratio of 3.6:3.6:1 (Figure 3.5).<sup>3</sup> The light from the slave is sent to the vacuum system table through an optical fiber and the laser beam is expanded to a waist of 1.5 mm by the collimator. The beam is split into three using half-wave plates and polarizing beamsplitters. These beams are further expanded using spherical telescopes to a waist of 4.7 mm for the vertical beam and 10.1 mm for the horizontal beams. To achieve cooling the laser frequency is red detuned by 45 MHz $\sim$ 1.5 $\Gamma$  with respect to the atomic transition. The typically used magnetic field gradient in the vertical direction is about 50 G/cm, created by the coil pair attached to the reentrant windows (MOT coils, see Section 2.4).

The strontium energy level structure dictates the details of the cooling mechanism and its efficiency. For bosons the ground state is a single, non-degenerated state, which means it has no dark states, an advantage compared to alkali atoms, which need a repumper to address the dark states. The  $^1S_0 - ^1P_1$  transition is not entirely closed since the excited state can decay to several states, therefore repumpers are needed to close these decay channels in order to obtain a high number of atoms, see Section 2.3.2. A disadvantage of a ground state without hyperfine splitting is that Sisyphus cooling doesn't work as easily as in alkalis. Hence we can only cool close to the Doppler temperature limit of 768  $\mu$ K.

Working with the fermionic isotope is complicated by the hyperfine structure due to the presence of a nuclear spin  $I = 9/2$ . The textbook explanation of a MOT is given for the  $F_g \rightarrow F_e = F_g + 1$  transitions, which is here only justified for the  $F_e = 11/2$  state. However during the bMOT operation all three substates of the  $^1P_1$  manifold (see Figure 2.16) are populated due to the inverted energy level structure and the small hyperfine splitting on the order of the linewidth. The presence of the magnetic substates enable sub-Doppler cooling, reducing the achievable temperature below the Doppler limit [100].

In our experiment we use the reservoir strategy to accumulate atoms beyond what the blue MOT can hold (see Section 2.3.2). The reservoir is populated by a decay channel from the  $^1P_1$  state through the  $^1D_2$  state into the metastable  $^3P_2$  state. Some substates of  $^3P_2$  are low-field seeking and they can be magnetically trapped by the quadrupole magnetic field used for the bMOT. The bMOT is operated until

---

<sup>3</sup>The optical system on the vacuum system table that creates the trapping beams is arranged in three levels: 1) the optical table, 2) two breadboards on the sides of the main chamber and 3) a top breadboard. The top breadboard is removed from Figure 2.1 for clarity. OSG stands for optical Stern-Gerlach, which is the technique used to characterize the nuclear spin state mixture of  $^{87}\text{Sr}$  clouds [95].

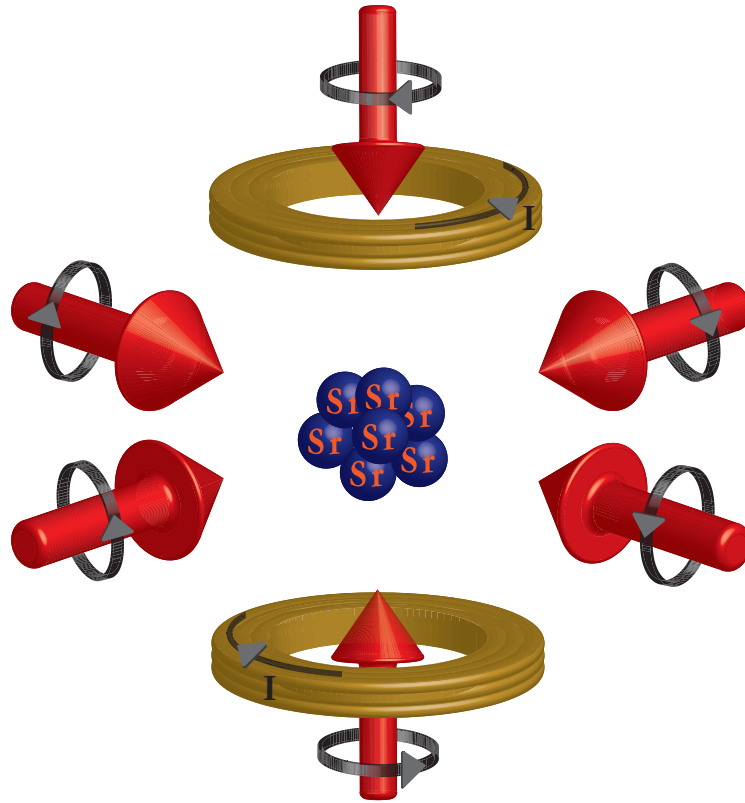


**Figure 3.4: Standard configuration of a magneto-optical trap.** The six laser beams (red) are circularly polarized as indicated by the black, circular arrows. The brown rings are quadrupole magnetic field coils with current  $I$ .

a sufficient number of atoms have been accumulated in the metastable reservoir. This loading time varies between isotopes to compensate for their different natural abundances (Table 2.1) and also depends on the desired number of atoms. The typical loading time ranges from 100 ms to 10 s. Even longer loading times up to 20 s are occasionally used for a single experimental run to obtain the largest possible atom number, but these long times are rather tedious and we avoid them when taking series of many measurements.

### 3.3.2 Red MOT

Once the desired number of atoms in the reservoir is reached the bMOT beams are shuttered off and a repump laser pulse transfers the reservoir atoms back to the ground state, where they are trapped by the next stage in the experimental sequence, a broadband rMOT. This MOT is operating on the narrow, 7.4 kHz wide  $^1S_0 - ^3P_1$  transition. Using such narrow optical transitions for laser cooling and trapping has become a powerful tool for experiments with alkaline-earth atoms. Cooling on

a narrow line allows to cool atoms close to the recoil limit by conventional Doppler cooling in a MOT and to achieve a high phase-space density, just three orders of magnitude away from quantum degeneracy [101].

The narrow linewidth of the transition gives the rMOT peculiar properties in comparison to the bMOT, which operates on a broad, 32 MHz wide transition. The pronounced differences between the two MOTs can be revealed by considering the range of the atomic velocities that can be captured by the MOT. An important condition for efficient laser cooling is continuous interaction of laser light with an atom while it is captured by the MOT. An atom that is slowed down by a MOT beam sees this beam under a changing Doppler shift during the slowing process and a changing Zeeman shift due to the spatially varying magnetic field. If the change in frequency is too large and the resonance condition is not fulfilled anymore, the atom might leave the MOT region. A bMOT can capture atoms of a large velocity range since the Doppler shift corresponding to the linewidth is relatively large,  $v_{\Gamma} = \Gamma/k = 15$  m/s. Furthermore an atom can scatter many photons from a single frequency laser beam while being slowed in the bMOT, resulting from  $\Gamma \gg \omega_R$ , where  $\omega_R = \hbar k^2/2m$  is the photon recoil frequency shift,  $k$  is the wave vector of the light and  $m$  is the strontium atomic mass. The rMOT has a very different behavior. The narrow linewidth corresponds to a small Doppler shift  $v_{\Gamma} = 5$  mm/s, which means only atoms in a small velocity range can be captured by the rMOT without additional tricks. Furthermore the photon recoil frequency shift is  $\omega_R/2\pi = 4.7$  kHz, which means that  $\Gamma \sim \omega_R$  and an atom can leave the resonance condition with light after scattering just a few photons. Moreover the two MOTs differ vastly in the maximum radiation pressure force that they can exert on the atoms. For the bMOT this force is  $F_{\max} = \hbar k\Gamma/2 \approx 10^5 \times mg$  ( $g$  is the gravitational acceleration of earth), whereas for the rMOT it is only  $F_{\max} \approx 16 \times mg$ .

Clearly, the two MOTs have distinctive properties. The bMOT is capable of capturing atoms from the Zeeman slower and cooling them to a typical temperature around 1 mK. The corresponding velocity distribution exceeds the capture velocity of the single frequency rMOT, limiting the transfer efficiency of atoms between the two MOTs. To improve the efficiency the spectrum of the rMOT laser beams is broadened by frequency modulation to match the Doppler profile of atoms in the reservoir [101]. The loading of the reservoir is finished by shuttering off the bMOT laser beams in about 4 ms with mechanical shutters. Next the atoms are captured by the broadband rMOT, the laser beams of which are switched on since the beginning of the experimental sequence. To capture the atoms they are optically pumped from

### 3.3. MAGNETO-OPTICAL TRAPS

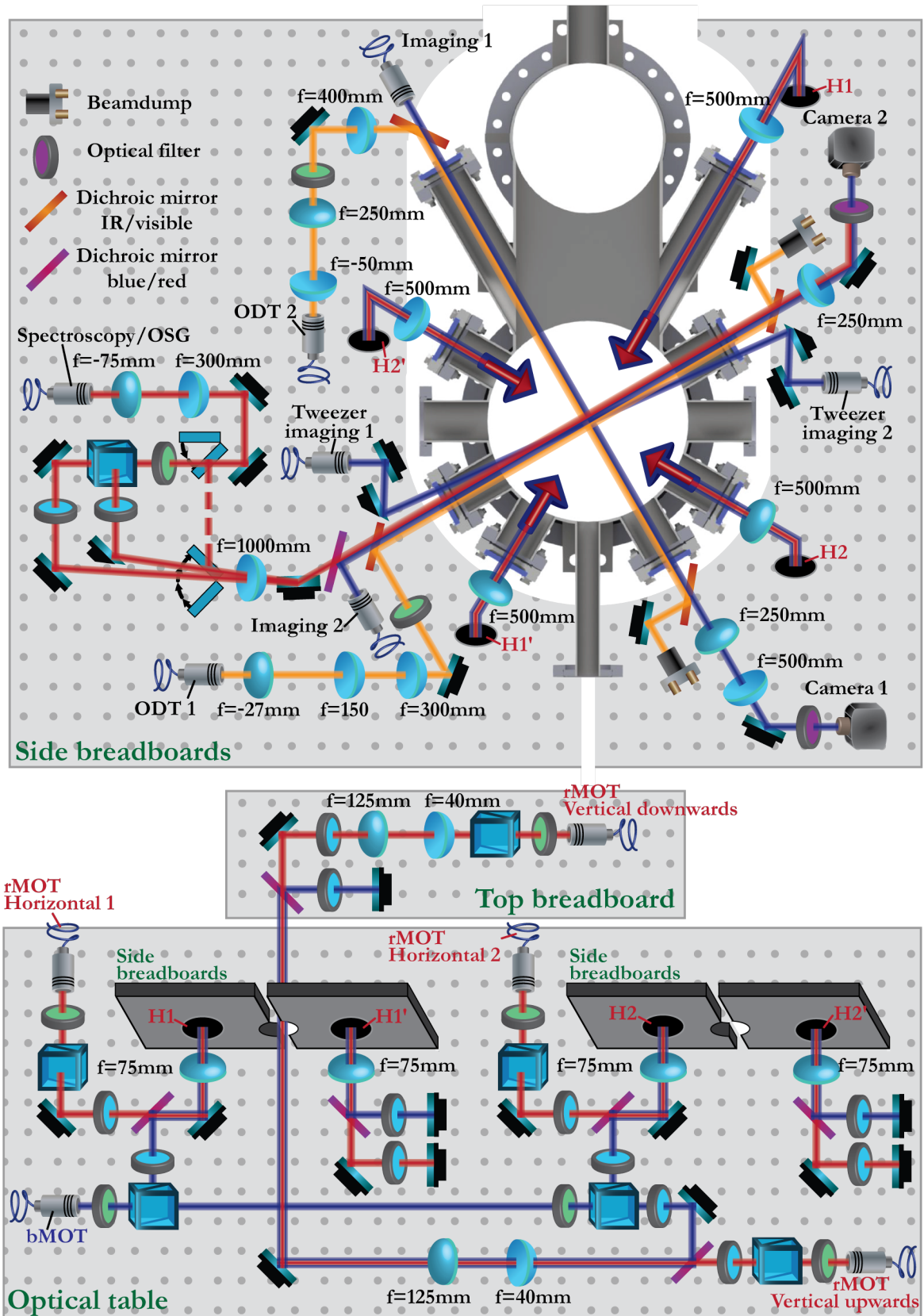


Figure 3.5: Optical setup preparing laser beams for the MOTs near the main vacuum chamber.

the  $^3P_2$  state to the ground state and the magnetic field gradient is ramped down to about 3.5 G/cm in the vertical direction (see Section 2.4).<sup>4</sup>

To reduce the temperature of the atomic cloud and to prepare it for loading into the dipole trap the parameters of the rMOT are changed in several steps over about 1 s. These parameters are the rMOT beam intensity and frequency span, and the quadrupole magnetic field gradient and center position. Before describing these steps we first need to discuss some important features of the rMOT.

We first consider the simple case of an rMOT with just a single frequency in its laser beams. The shape of this rMOT is related to the condition of significant photon scattering of the laser beams by the atoms [102], which is

$$2|\delta + \vec{k}\vec{v} - \mu B(\vec{r})| < \Gamma_E ,$$

where  $\delta = \omega - \omega_0$  is the frequency detuning from the atomic resonance  $\omega_0$ ,  $\mu = \mu_B(g_e m_e - g_g m_g)/\hbar$ ,  $B(\vec{r})$  is the magnitude of the rMOT quadrupole field,  $g_e = 1.5$  is the Lande factor for  $^3P_1$  and  $g_g = 0$  the one for  $^1S_0$ .  $\Gamma_E = \Gamma\sqrt{1+s}$  is the power broadened, effective linewidth of the  $^1S_0 - ^3P_1$  transition, where  $s = I/I_{sat}$ , with saturation intensity  $I_{sat} = 3 \mu\text{W cm}^{-2}$ . Assuming for simplicity that the atoms are moving very slowly and that the linewidth is small, we can neglect the velocity dependent term and set  $\Gamma_E = 0$ , resulting in  $\delta = \mu B(\vec{r})$ . This equation describes an elliptical shell on which the lasers are resonant with the atoms. Atoms on this shell experience a radiation pressure force pushing them inwards, resulting in an outer boundary of the MOT. The width of the shell in which the atoms experience the force is finite in reality, since  $\Gamma_E$  is finite.

To determine the shape of the single-frequency MOT we need to take into account the effect of gravity. For the bMOT the effect of gravity is negligible since the radiation pressure force is  $10^5$  times larger than the gravitational force. However the situation is different for the rMOT, where the radiation pressure force is only 16 times larger. The effect of gravity becomes especially noticeable for large detuning ( $\delta > \Gamma_E$ ) and intensities above the saturation value ( $s > 1$ ). The atoms experience no light pressure inside the shell and the gravitational force pulls them to the shell's bottom, where the cloud adapts the form of a shallow, round bowl. The atoms do not absorb photons from the beam that is propagating downwards since its frequency is far detuned from the atomic transition that its polarization allows to address. They

---

<sup>4</sup>An optional additional change for the magnetic field is compression of the magnetic reservoir to improve overlap with the rMOT. The additional step is a ramp of the field gradient from the bMOT value of about 50 G/cm to 80 G/cm and only then to the rMOT field of 3.5 G/cm.

mostly absorb photons from the beam that is propagating upwards and the radiation pressure force is balancing the gravitational force, keeping the atoms levitated. The position and the shape of the atomic cloud are influenced by the origin of the quadrupole magnetic field, which can be moved around by applying bias fields, and by the frequency detuning, which determines the size of the shell for a given magnetic field. Using bias fields and frequency detuning, the size and position of the cloud can be adjusted, for example to match the shape and position of an optical dipole trap. The picture described so far is correct for an atomic cloud that is very cold and for an elliptical shell that exceeds the size of the atomic cloud. For temperatures above a few microKelvin the cloud significantly expands upwards in the gravitational potential. The maximum extension in this direction is usually given by the upper edge of the resonance shell, where the downwards propagating rMOT beam pushes the atoms back down.

The capture velocity and the capture volume of the single-frequency rMOT is too low to capture the milliKelvin-temperature reservoir atoms that are spread out over a cubic centimeter or so. In order to increase the capture velocity and volume the frequency of the rMOT laser beams is modulated, leading to a broad comb of frequencies. Each frequency corresponds to one of many nested shells on which stationary atoms are resonant with one of the laser beam's frequencies, thereby providing a large capture volume. The resonance width of each shell is related to the effective linewidth of the atomic transition  $\Gamma_E$ . We use a spacing of 20 kHz between up to 150 frequency components and  $s > 1$  to broaden the shells, which keeps the scattering rate close to maximum throughout the resonant volume. The frequency comb also allows us to address a large range of velocities, which increases the capture velocity of the rMOT. Together the increased capture velocity and volume lead to an efficient capture of reservoir atoms by the broadband rMOT after repumping. Perhaps astonishingly little laser power is needed to prepare the frequency comb because the saturation intensity of this narrow transition is low. In our system the typical power per rMOT laser beam per slave is about 3 mW, allowing to reach  $s \sim 3$  per frequency component for a beam with about 1 cm waist and 150 frequency components.<sup>5</sup>

The achievable temperature of the atomic cloud in the rMOT can be very low. The Doppler temperature  $T_{\text{Doppler}} = \hbar\Gamma/2k_B = 180 \text{ nK}$  is lower than the temperature

---

<sup>5</sup>The power of each beam of the rMOT optical setup is additionally controlled by polarizing beamsplitters with half waveplates placed after fiber collimators and the power is reduced to about 2.7 mW (Figure 3.5).

Stage	Modulation range [MHz]	# frequency components	Ramp time [ms]	Hold time [ms]
Capture	-0.15 ... -3	142	on from beginning	200
I	-0.15 ... -1.15	50	150	100
II	-0.1 ... -0.6	25	150	200
III	-0.1 ... -0.1	1	150	100

**Table 3.1: Typical stages of the rMOT operation used to produce quantum degenerate gases.** The modulation range is given relative to the atomic transition. The rMOT laser beams are on from the beginning of the experimental cycle. The duration of the capture stage is given with respect to the switching time of the magnetic field from the bMOT to the rMOT. Each stage consists of a linear ramp of all relevant parameters and a hold time during which the parameters are held fix.

corresponding to a single photon recoil of  $T_{\text{recoil}} = \hbar^2 k^2 / mk_B = 460 \text{ nK}$  where  $k_B$  is the Boltzmann constant. When using laser beams with a single frequency component and low intensity ( $s \sim 1$ ), the effect of the photon recoil becomes pronounced. It modifies the dynamics of the cooling process and the lowest reachable temperature is close to the recoil temperature [103]. Obtaining a low temperature in the rMOT facilitates laser cooling close to quantum degeneracy, for the pulsed regime the phase-space density can reach  $10^{-2}$  [101] and in continuous operation  $10^{-3}$  [28].

### Red MOT stages

The rMOT parameters are varied over time in stages, which have the tasks to first efficiently capture reservoir atoms, then to compress and cool the cloud, and finally to overlap it with the optical dipole trap. Staged operation was pioneered in single-frequency rMOTs [7, 104] and further analyzed in [70, 105–107]. It was shown that the trap dynamic is primarily governed by the detuning  $\delta/\Gamma_E$  and the saturation parameter  $s$ . In our experiment we do not necessarily follow through stages discussed in those works, but our stages are somewhat similar.

The stages are distinguished by the intensity and frequency broadening range of the rMOT laser beams. We use several different ramp schemes in dependence of the pursued goals. Table 3.1 shows the ramp scheme typically used to produce degenerate quantum gases. The rMOT beams are set with the parameters of the capture stage already at the beginning of the experimental cycle. For all stages the modulation frequency, and therefore the spacing of the frequency components, is

20 kHz. The modulation is executed in a triangular fashion in between the extreme frequencies.<sup>6</sup> In the capture stage the full laser power is used, leading to a high saturation parameter per frequency component ( $s > 1$ ). In the following stages of the rMOT, the power gradually drops and the frequency spectrum range decreases, but the saturation parameter is maintained at a level of  $s \sim 1$  per frequency component.

The rMOT stages can conveniently be adapted to different requirements. For instance, to efficiently load the dipole trap, the size of the rMOT and its location can be adjusted to match the shape and position of the dipole trap. Another example is changing the compromise between the number of atoms, the temperature of the cloud and the duration of the experimental cycle, e.g. two short stages can be used while tolerably decreasing the number of atoms and increasing the temperature.

The optical layout for the rMOT on the vacuum system table is analogous to the bMOT (Figure 3.5). The major difference is using dedicated optical fibers for the horizontal and vertical beams. To make a compact design and preserve valuable space on the vacuum system table, blue and red laser beams are overlapped on dichroic mirrors. The telescopes expanding beams for the bMOT are used to increase the waists of the rMOT laser beams to 5.3 mm for the vertical beams and to 11.3 mm for the horizontal beams. The power and frequency settings of the rMOT laser beams are controlled with 80 MHz AOMs in the red laser system.

### 3.3.3 Fermionic rMOT

Laser cooling on the narrow  $^1S_0 - ^3P_1$  transition has additional features for fermionic  $^{87}\text{Sr}$  in comparison to bosonic Sr. The fermionic isotope has a nuclear spin of  $I = 9/2$  leading to hyperfine splitting. The  $^1S_0$  state has a single hyperfine state of  $F = 9/2$  with ten magnetic substates, while the hyperfine interaction splits the  $^3P_1$  state into three states with  $F = 7/2, 9/2$  and  $11/2$ .

Conventional laser-cooling is most easily understood for a  $F_g = 0 \rightarrow F_e = 1$  transition with a single, non-magnetic ground state, as it is the case for bosonic Sr. This technique is readily expanded to several magnetic substates  $F_g \rightarrow F_e = F_g + 1$  if the Zeeman shift in the ground and excited manifold have similar magnitude, resulting in efficient cooling and trapping for all substates, as is the case for alkali atoms. A criterion for the proper functioning of the MOT can be defined by considering the

---

<sup>6</sup>We use Analog Devices AD9852 direct digital synthesizers to produce the modulated radiofrequency.

resonance condition for the restoring force

$$\hbar\delta = ((m \pm 1)\mu_e - m\mu_g)B(x),$$

which for simplicity is written for one spatial dimension. Here  $\delta$  is the laser detuning as before,  $m$  denotes a magnetic substate of the ground state manifold,  $\mu_e = g_e\mu_B$  and  $\mu_g = g_g\mu_B$ , with Lande g-factors of the considered ground and excited states, and  $\mu_B$  is the Bohr magneton. The  $\pm$  sign stands for the interaction with  $\sigma^+$  and  $\sigma^-$  polarized laser beams. This equation needs to be fulfilled for all substates so the restoring force can act on all atoms regardless of their specific substate. This condition can be formulated as the inequality

$$\frac{F}{F+1} < \frac{\mu_e}{\mu_g} < \frac{F}{F-1} \quad \text{for } F \rightarrow F+1,$$

assuming that the laser light is detuned below the resonance, i.e. red detuning [108]. These inequalities are for instance satisfied for Rb, guaranteeing that all magnetic substates are trapped.<sup>7</sup>

The situation is more subtle with alkaline-earth elements since the magnetic moment of the ground state is determined by the nuclear moment, orders of magnitude smaller than the magnetic moment of an electron, and consequently  $\frac{\mu_e}{\mu_g} \gg 1$ . As a result the ground state is not influenced significantly by the magnetic field and stays almost degenerate (Figure 3.6a-c). To more clearly understand the differences between a usual MOT and an rMOT of  $^{87}\text{Sr}$ , let us consider the force that atoms experience in the trap. As an example we use an atom in the ground state with  $m_{Fg} = 9/2$  located to the left of the MOT center, see Figure 3.6d. Absorbing a photon of  $\sigma^+$  polarized light from the right-propagating beam creates a restoring force pushing the atom to the center. Alternatively there is a probability to absorb a photon from the  $\sigma^-$  polarized left-propagating beam, making an expelling force pushing the atom away. Hence, the dynamics is governed by the interplay of the restoring and expelling forces, leading to substate dependent trapping. The situation is corrected by the transition strengths, which are proportional to the Clebsch-Gordan coefficients and which depend on the  $m_I$  substate and light polarization (Figure 3.6e). The strength of  $m_{Fg} \rightarrow m_{Fe} = m_{Fg} + 1$  transitions reach a maximum for the largest  $m_{Fg} = 9/2$  and decrease monotonically going to  $m_{Fg} = -9/2$ . For the  $m_{Fg} \rightarrow m_{Fe} = m_{Fg} - 1$  transitions the strength distribution is the opposite: maximum

<sup>7</sup>The cooling transition for  $^{87}\text{Rb}$  is  $5^2S_{1/2}(F=2) - 5^2P_{3/2}(F=3)$  with Lande g-factors for the ground and excited states  $g_F(5^2S_{1/2}) = 1/2$  and  $g_F(5^2P_{3/2}) = 2/3$ . Plugging these values into the inequalities leads to  $2/3 < 4/3 < 2$ .

for  $m_{F_g} = -9/2$  and decreasing to  $m_{F_g} = 9/2$ . In the considered example of  $m_{F_g} = 9/2$ , the excitation probability ratio for the restoring and repulsing force is the most extreme 55:1. Therefore on average over many absorbed photons the restoring force dominates [109].

Another important feature of the trapping process is evident from the previous consideration: the restoring force creates a proper confinement in only one hemisphere. In the example with the atom in the  $m_F = 9/2$  substate on the left side from the MOT center, the resonance condition might be satisfied for either beam in the counter-propagating pair. However, if the atom moves to the right-hand side the resonance condition is not fulfilled since the linewidth of the transition is narrow. Hence neither MOT beam is resonant with the atomic transition and the restoring force is weak, leading to loss of atoms. An often employed mechanism to close this loss channel is based on the fast redistribution of atoms over the magnetic substates. An additional laser beam is used to randomize the atomic population in the ground manifold, which on average recovers a restoring force across the whole MOT. Accordingly, the fermionic rMOT requires two laser beams, one for creating the trapping force and another one for stirring the atomic population. An alternative mechanism of cooling without the stirring beam is realized in sawtooth-wave adiabatic passage (SWAP) cooling which is based on sweeping the laser frequency across the atomic resonance [110].

For the experiments with the fermionic isotope we use two amplifying slaves on the red laser system with superimposed beams. The first one generates trapping light and it is red detuned to the  $^1S_0(F_g = 9/2) \rightarrow ^3P_1(F_e = 11/2)$  transition, which satisfies the  $F_g \rightarrow F_e = F_g + 1$  condition. The second one is used for stirring and it is red detuned to the  $^1S_0(F_g = 9/2) \rightarrow ^3P_1(F_e = 9/2)$  transition. The Zeeman coefficient for the  $F_e = 9/2$  state is 4.5 times smaller than for the  $F_e = 11/2$  state, reducing the splitting of magnetic substates and thus increasing the spatial region of efficient atom-light interaction.<sup>8</sup>

The presence of ten magnetic substates in the ground manifold influences the shape of the atomic cloud. The resonance condition for the restoring force is fulfilled at different locations for different substates. Hence the spatial structure of the trap can be seen as a set of nested shells (Figure 3.7).

The ramp stages of the fermionic rMOT are similar to the ones of the bosonic rMOT. A small difference exists in the final rMOT parameters. Typically for bosons the final modulation range is only one frequency component, i.e. no frequency mod-

<sup>8</sup>The  $g$ -factor of the  $F_e = 11/2$  state is 3/11 in comparison to 2/33 for  $F_e = 9/2$ .

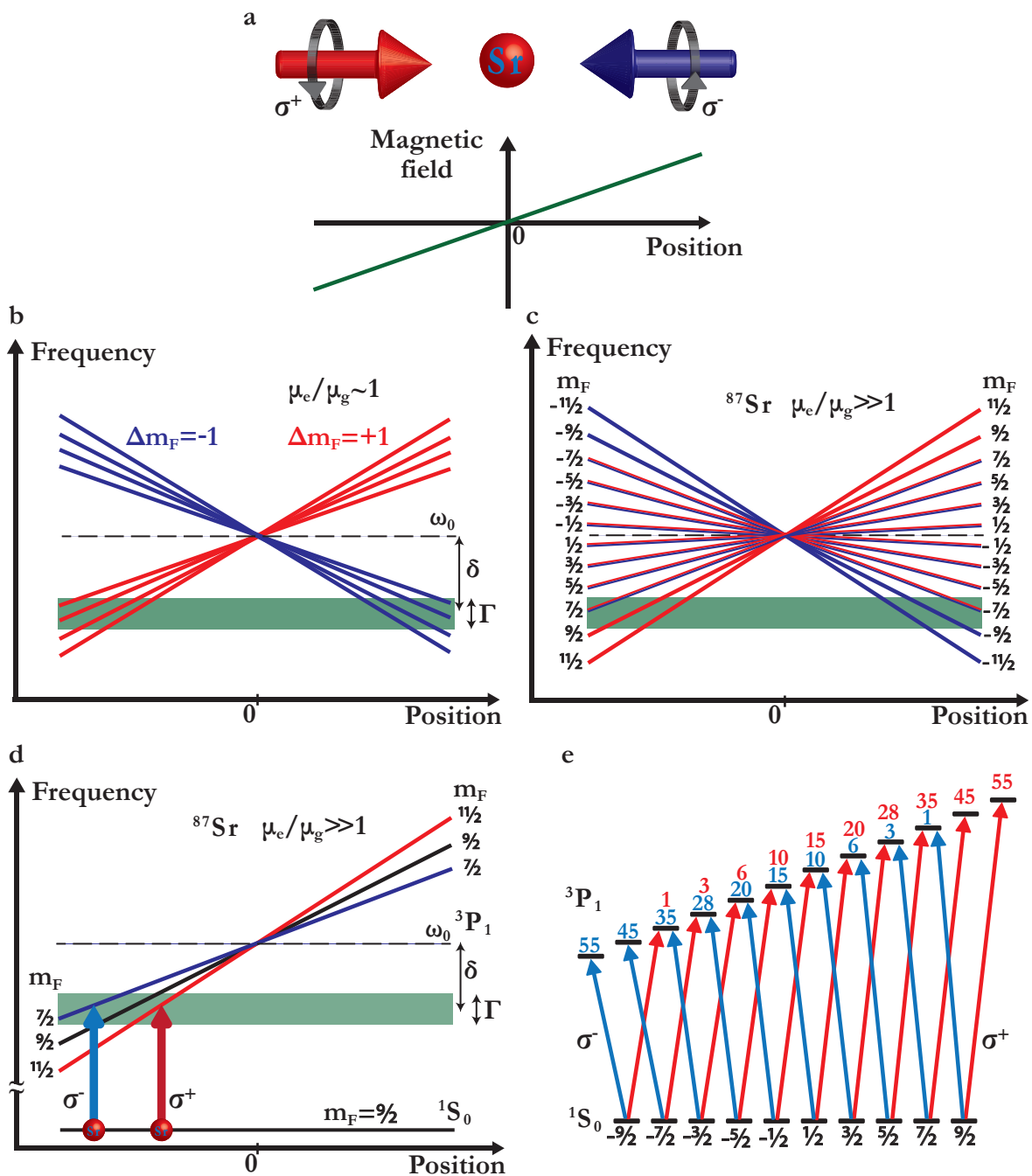


**Figure 3.6: Details of  $^{87}\text{Sr}$  laser cooling with the rMOT.** **a**, Conventional configuration of the magneto-optical trap, illustrated for simplicity only along one axis. The quadrupole magnetic field close to the center points along that axis and depends linearly on space. **b** and **c** show the difference in energy between ground and excited F,  $m_F$  states connected by sigma transitions. The green bar indicates the resonance condition for the rMOT laser beams, which have detuning  $\delta$  and address a transition with width  $\Gamma$ . **b** illustrates a typical diagram for alkali elements, e.g. Rb, and **c** for the  $^{87}\text{Sr}$   $^1S_0 - ^3P_1$  transition. **d**, Example illustrating the balance of forces from the rMOT beams for an atom in the  $m_F = 9/2$  substate, see text for details. **e**, Relative transition probabilities.

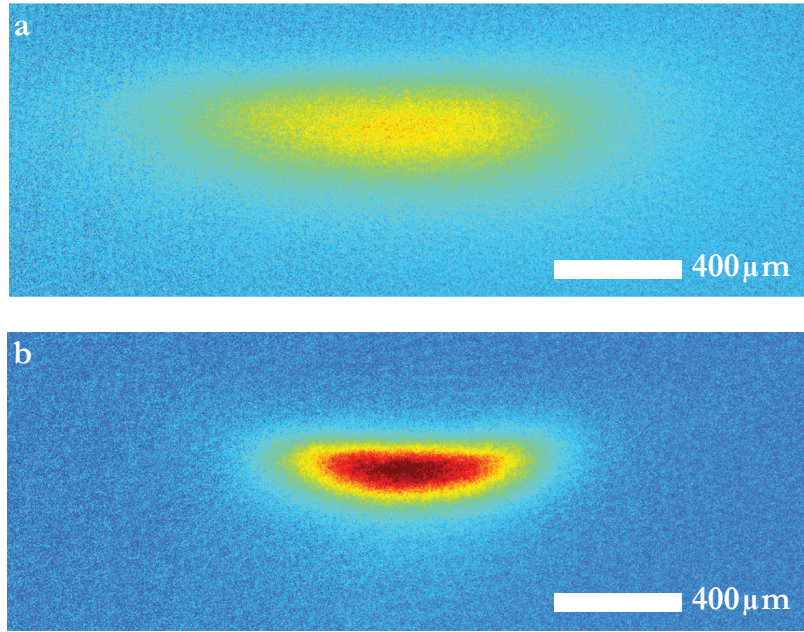


**Figure 3.7: In-situ absorption images of the  $^{87}\text{Sr}$  rMOT during the last stages of laser cooling.** The size of the atomic cloud is dictated by the parameters of laser beams and the magnetic field gradient. For image **a** the modulation range is about 0.6 MHz and the sideband closest to resonance is detuned by 0.1 MHz. **b**, The size of the MOT is reduced by increasing the confinement using a ramp of the modulation width down to 0.03 MHz and shifting the closest sideband to a detuning of 0.07 MHz from the resonance. In both cases the magnetic gradient of the MOT quadrupole field is 3.65 G/cm in the vertical direction (along the coils axis). As described in the main text the  $^{87}\text{Sr}$  rMOT is a set of nested shells, corresponding to different magnetic substates. Therefore the trapped atoms tend to occupy a large fraction of an ellipsoid volume in comparison to the bosonic rMOT, which settles at the bottom of such an ellipsoid. For comparison Fig. 3.8a shows a single-frequency  $^{84}\text{Sr}$  rMOT.

ulation, while for the fermionic isotope the modulation range extends over five frequency components separated by 20 kHz with an intensity of  $I_{\text{sat}}$  per component. The changes in the parameters of the stirring beam closely follow the changes in the trapping beam parameters, with almost identical settings for the modulation spectrum and intensity of laser beams.

### 3.4 Dipole trap

The next trapping stage after the rMOT is an optical dipole trap (ODT), a focused laser beam with frequency far detuned from atomic resonances [111]. ODTs have

become an indispensable tool in experiments with ultracold gases especially for research focused on creating quantum degenerate gases. They are particularly important for experiments with alkaline-earth elements due to the absence of an electronic magnetic moment in the ground state, which renders magnetic trapping impossible. To create a tight confinement in all three dimensions we use a crossed-beam configuration with laser beams propagating horizontally and perpendicularly to each other. To simplify alignment the ODT laser beams are overlapped with the imaging passes on the optical setup around the main chamber. This allows to take an image of the trapped atoms and the ODT beams using the same camera, which makes overlapping the ODT beams with the atoms easier. The optical setups for the two laser beams are similar: light is delivered to the optical breadboards through polarization-maintaining single mode fibers, collimated by aspherical lenses, expanded by a factor five with telescopes and then focused onto the atomic cloud with lenses. The focal waist of the two ODT beams are 77 and 62  $\mu\text{m}$ .

To efficiently load atoms into the dipole trap the depth of the optical potential should be substantially higher than the temperature during the final stage of the rMOT, which is typically  $\sim 1 \mu\text{K}$ . The laser power in the two ODT beams is limited to 4 W and 2 W respectively, allowing to produce a sufficiently deep trap of about 30  $\mu\text{K}$  depth with trap frequencies of around  $\{\omega_x, \omega_y, \omega_z\} = 2\pi \times \{211, 193, 285\} \text{Hz}$ , where the z axis is vertical, and the x and y axes are oriented along the dipole trap beams. The IR light source is specified to provide up to 45 W, which exceeds the necessary power for the crossed ODT and will allow us in the future to also provide light for the optical transport of atoms from the main chamber to the science chamber or the glass cell and for optical lattices.

To determine the trap frequencies we measure a spectrum of collective excitations of atoms in the trap, induced by time-dependent perturbation of the dipole trap parameters [112–114]. An initial, rough determination is undertaken by modulating the power of the ODT beams and observing dips in the number of atoms as the modulation frequency reaches multiples of the trap oscillation frequencies, leading to parametric heating of atoms out of the trap. An additional method to verify the trap frequencies is to induce center-of-mass motion and measure the frequency of the damped oscillation. To produce this motion the power of one ODT beam is abruptly switched to a lower value for a short period of time or alternatively the power is modulated at the resonant frequency.

The dipole trap is the stage following the rMOT and the transfer efficiency between the two traps depends to a high degree on good shape-matching and over-

lapping. As discussed in the previous sections the trap geometry of the rMOT is different for the bosonic and fermionic isotopes. The bosonic isotopes occupy the bottom of an ellipsoid shell, while the fermionic isotope tends to fill an ellipsoid volume. The size and position of elliptic shells are determined by the resonance condition for the rMOT restoring force as a result of the interplay between the laser detuning, saturation parameter and magnetic field gradient. By varying the parameters of the last phase of the rMOT the trap size is reduced, increasing the atomic density. The rMOT location is adjusted by adding offset fields with the compensation coils, thereby shifting the position of the MOT quadrupole center. A challenge is to optimize the ODT to work efficiently with either isotope without changing the optical setup. The rMOT shape is extended in the horizontal plane, therefore in experiments with ultracold strontium horizontally extended, elliptical ODT beams are usually used to improve the overlap between the rMOT and ODT. We currently use round beams and leave the optimization of the beam shapes for the future. The typical number of atoms and the temperature of the cloud in the dipole trap are about  $2.5 \times 10^6$  atoms at  $1.3 \mu\text{K}$  for  $^{84}\text{Sr}$  and about  $10^6$  atoms at  $1.5 \mu\text{K}$  for  $^{87}\text{Sr}$ .

The specifics of the loading process from the rMOT to the crossed ODT are represented in Figure 3.8. The figure is a collection of in-situ absorption images, taken during the alignment of the traps when we were pursuing condensation of  $^{84}\text{Sr}$ . They illustrate our alignment procedure and show how to progressively increase the transfer efficiency. The alignment task is to overlap three traps: the rMOT and the two ODTs. The alignment starts by overlapping the rMOT with just one of the two ODTs, ODT1. The rMOT is shown in Figure 3.8a and a characteristic feature of the rMOT is the sharp bottom edge of the atomic cloud, corresponding to the elliptical shell. Figures 3.8a,c show the overlapping between the rMOT and ODT1. The transfer efficiency is limited and atoms that are not trapped by ODT1 fall under the gravitational force as soon as the rMOT is switched off (3.8e). Next the second ODT laser beam, ODT2, is added to the setup, creating a crossed ODT configuration. Figures 3.8d to g show the rMOT and ODTs in a sequence of situations with gradually improving alignment. To analyze the trap overlap in all three dimensions, we use two imaging systems that image along the ODT beams. Figures 3.8k to l show images from the second imaging system, which has about two times smaller resolution than the first system.

When trying to make an experimental sequence work it can be useful to briefly increase the number of atoms in the rMOT with measures that would not be usually used during long-term operation of the experiment. I will list here a few measures

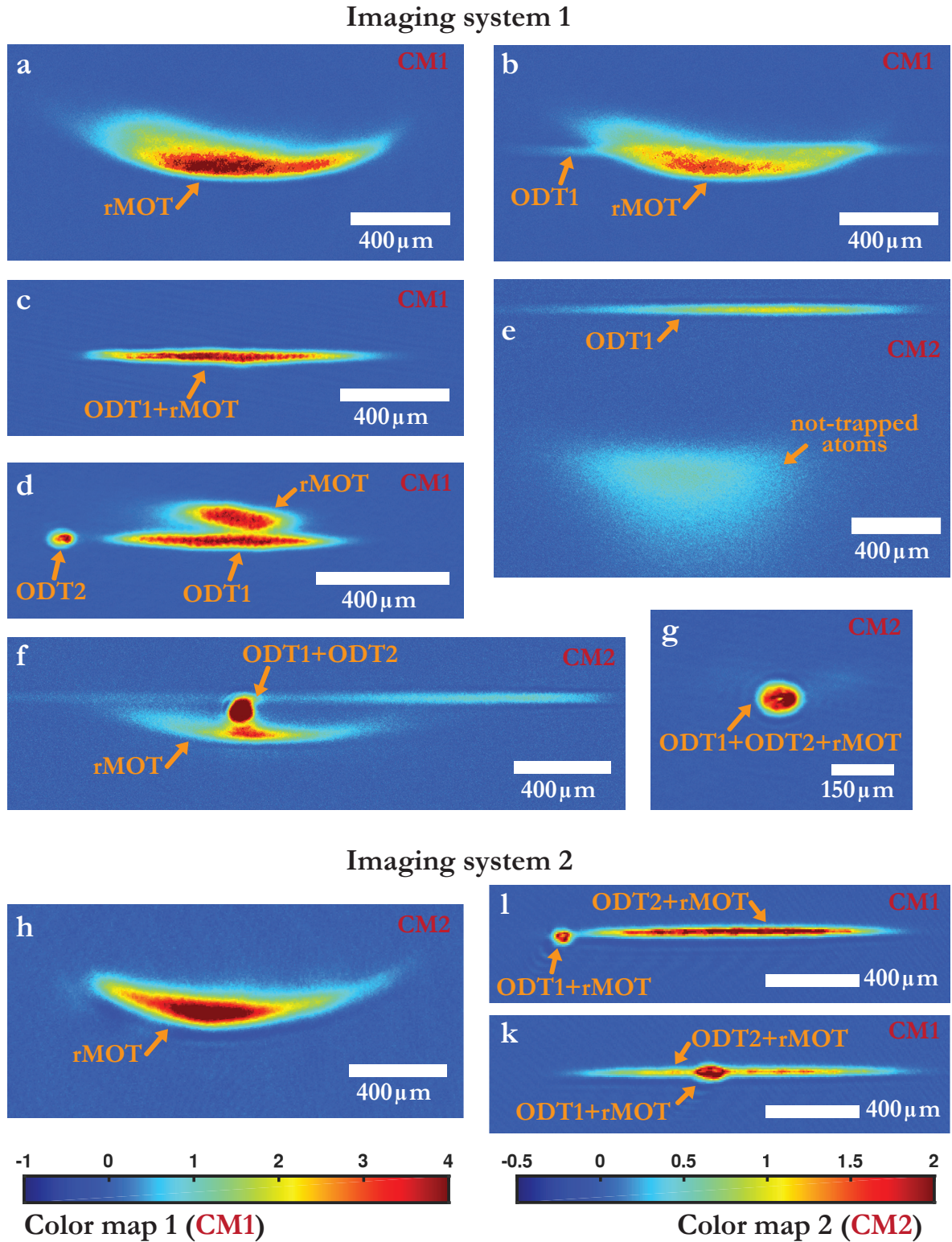


Figure 3.8: A collection of absorption images illustrating the transfer of  $^{84}\text{Sr}$  from the rMOT to the crossed ODT. For details see the main text.

that might be helpful in obtaining for the first time, for instance, the dipole trap or degenerate gases. The first option is to increase the loading time of the magnetically trapped reservoir, thus accumulating more atoms in the metastable state. The long accumulation time substantially increases the duration of the experimental cycle beyond the usual time used to make quantum gases. The second option is to increase the flux of atoms effusing from the oven by increasing the oven temperature. A higher temperature is a tempting solution to overcome a difficult situation, however it should be used wisely to avoid premature depletion of the Sr in the oven. The next possibility is to increase the power of the laser beams in the blue and IR systems. We noticed that the bMOT performance is improved when higher intensity is used for the Zeeman slower or MOT laser beams. One way to increase the power is to operate the blue slave laser diodes at higher current than we usually do. To increase the laser diode lifetime we chose to operate slave lasers below their specified maximum power. Since we didn't observe any degradation of these laser diodes in years, we might have been very conservative and could push the power to the maximum specified value. Another way to increase the power is to build additional slaves for each MOT axis or to move the slave preparing the Zeeman slower laser beam to the vacuum system table, gaining about 50% of power currently lost on the fiber coupling. Another enhancement of our experiment, already mentioned above, is to better mode match the ODTs with the rMOT, which requires increasing the power of the IR laser beams. The disadvantage of increasing the usage of laser power is purely financial and appetite for more powerful light sources is notorious to grow quickly.

### **Evaporative cooling**

After loading atoms into the dipole trap the primary technique to achieve quantum degeneracy is evaporative cooling. The idea is to force evaporation of atoms with energy larger than average by gradually reducing the trap depth. Atoms remaining in the trap continuously rethermalize by elastic collisions and thermal equilibrium is reached at lower temperature. Although the total number of trapped atoms is decreased by evaporation, they occupy a smaller volume and their temperature is progressively lowered. This leads to the required gain in phase-space density, allowing to reach quantum degeneracy.

An unpleasant feature of strontium for evaporative cooling is an unfavorable relation between scattering properties and isotope abundance. The scattering length

of the most abundant strontium isotope,  $^{88}\text{Sr}$ , is close to zero, therefore the rate of elastic collisions is small, hampering efficient thermalization. Conversely, the scattering length for the next abundant isotope,  $^{86}\text{Sr}$ , is very large, resulting in a high inelastic collision rate and strong three-body losses. The broadly used technique of tuning the scattering properties with magnetic Feshbach resonances is not applicable in alkaline-earth systems due to the low sensitivity of the ground state to the magnetic field. Only the scattering behavior of the two less abundant isotopes, bosonic  $^{84}\text{Sr}$  and fermionic  $^{87}\text{Sr}$ , is suitable for efficient evaporation.

The evaporation trajectory depends on the desired final characteristics of the atomic cloud and on the acceptable evaporation time. We used one, two or three linear ramps during evaporation depending on the goals. For instance the measurement of the trap frequencies, which is done with a BEC, do not require high atom number, but profit from a short time of the experimental cycle, therefore the evaporation can be done with a single, short power ramp. Conversely, the production of a large DFG is a more demanding target, thus our evaporation strategy consists of three carefully optimized ramps.

### 3.5 Bose-Einstein condensation of $^{84}\text{Sr}$

With the creation of the first Bose-Einstein condensate (BEC) of ultracold atoms in 1995, these quantum gases became a powerful instrument for studying quantum phenomena, creating great impact across various fields in physics. Since then the number of species cooled down to quantum degeneracy has been gradually increasing. The unique properties of strontium make the degenerate gases of this element a promising platform to address challenging problems in the fields of quantum computation and simulation, quantum chemistry and precision measurement, to name but a few.

There are three bosonic isotopes of strontium and condensation was achieved with each of them [5]. Due to the significantly different scattering properties the cooling strategy has to be tailored for each isotope. The first BEC was obtained with  $^{84}\text{Sr}$  where the primary advantage is a favorable scattering length of about  $124a_0$ , where  $a_0$  is the Bohr radius [1, 2]. The low natural abundance of 0.56% is overcome by using a long accumulation time of atoms in the metastable reservoir. Besides, the efficiency of narrow-line laser cooling allows to reach a remarkable phase-space density in the dipole trap of about 0.1, higher than the one reached in rMOTs [5]. The reason is that an rMOT must support atoms against gravity,

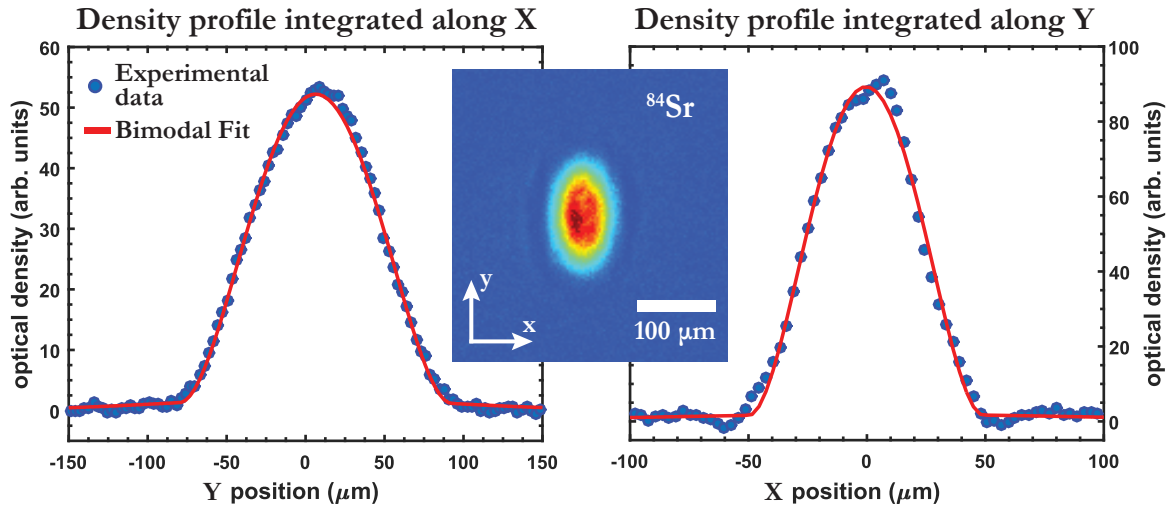


**Figure 3.9: Condensation of  $^{84}\text{Sr}$ .** An almost pure BEC of  $^{84}\text{Sr}$  is observed after evaporative cooling in the dipole trap followed by 20 ms of free expansion. The data points in the left and right profiles are densities integrated along the absorption imaging beam and one of the image axes. The solid red line is a bimodal fit with parameters retrieved from a two-dimensional fit. The inset shows the absorption image corresponding to the profiles.

requiring beams with an intensity around  $I_{\text{sat}}$ , whereas laser cooling of atoms in a dipole trap can be done with much weaker beams, reducing multiple scattering of photons and light-assisted collisions. Quantum degeneracy can even be reached using only laser cooling to remove the entropy from the gas. To do so, the density of atoms is increased in a small additional dipole trap, protected from laser cooling photons [115]. This cooling procedure even brings hope to produce BECs in steady-state and variations of it might lead to a continuous atom laser [28]. The largest produced  $^{84}\text{Sr}$  BECs exceed  $10^7$  atoms and BECs with about  $10^5$  atoms have been created in experimental cycles that take only 2 s [94].

$^{86}\text{Sr}$  has a good natural abundance (9.86%), but it suffers from strong three-body losses because of its large scattering length of  $830a_0$ . The challenge to achieve degeneracy is overcome by performing evaporation with a dilute sample ( $n \sim 3 \times 10^{12}$  atoms/cm<sup>3</sup>), more than an order of magnitude less than the typical densities used for  $^{84}\text{Sr}$  [94]. Reducing the atomic density sufficiently improves the ratio of elastic collisions to three-body collisions. Even at the lowered density a sufficiently high elastic collision rate for evaporation is reached because of the large scattering length. To efficiently capture atoms from the rMOT while maintaining the condition of low density a large volume optical dipole trap is used. The largest  $^{86}\text{Sr}$  BECs created thus far have a few  $10^4$  atoms [116].

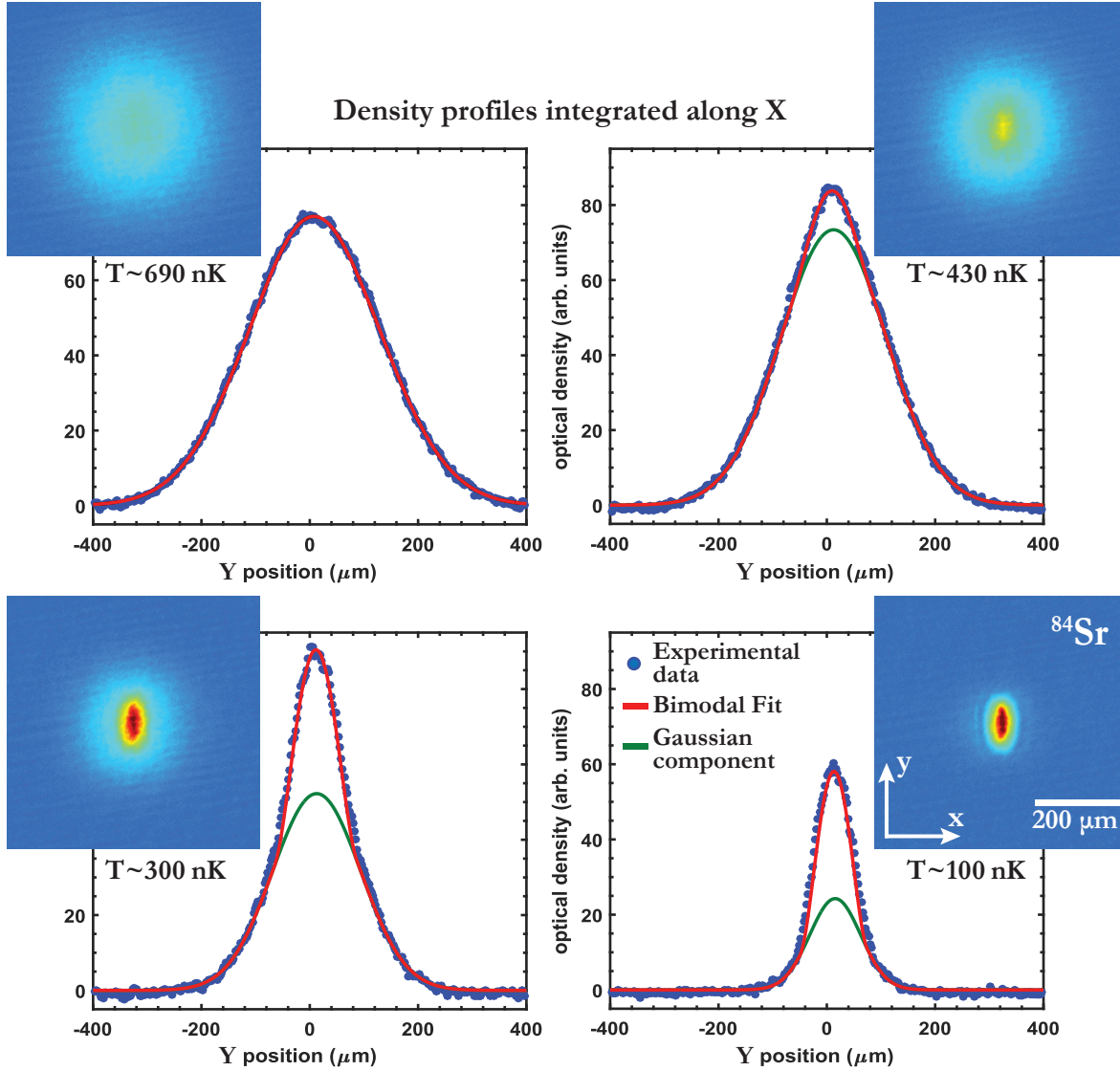


**Figure 3.10: Phase transition from a thermal atomic cloud to a BEC.** The density profiles show the formation of the condensate during evaporative cooling, achieved by varying the power of one of the ODT laser beams. The density profiles are obtained by integrating along the x axis of the absorption images (shown as insets), recorded after 15 ms of time-of-flight. The solid red lines show the bimodal fits with parameters retrieved from two-dimensional fits, the solid green lines correspond to the Gaussian part of the bimodal distribution, which is related to the thermal fraction.

Developing an efficient strategy to obtain a BEC of  $^{88}\text{Sr}$  is challenging despite the largest abundance among all the stable isotopes (82.58%) since the scattering length is small and negative, about  $-2a_0$  [117]. A successful strategy is based on sympathetic cooling with  $^{87}\text{Sr}$  by taking advantage of the favorable interspecies scattering length of about  $a = 55a_0$ . Hence, the experimental cycle is complicated by laser cooling and trapping of two isotopes. The number of condensed atoms is limited because species with negative scattering length experience an attractive interactions and collapse above a critical number of atoms [118].  $^{88}\text{Sr}$  BECs have been created with atom numbers close to  $10^4$  [117].

In our experiments with BECs we focused on the  $^{84}\text{Sr}$  isotope, although in principle the constructed system is compatible with the production of  $^{86}\text{Sr}$  and  $^{88}\text{Sr}$  condensates. In order to produce a  $^{84}\text{Sr}$  BEC we load atoms from the rMOT into the dipole trap and perform evaporative cooling. The evaporative cooling leads to an increase in phase-space density and a phase transition to quantum degeneracy is observed. An easily recognizable hallmark of the transition is a bimodal density distribution, recorded after suddenly releasing the gas from the trap and letting it freely expand for a few tens of ms. The bimodality originates from the different expansion behavior of thermal atoms and atoms in the condensate [88]. The bimodality is easily observable on absorption images, see Figure 3.10. The broader part of the distribution is the thermal fraction of the atomic cloud and in the simplest approximation it can be described by a Gaussian<sup>9</sup>

$$n_{\text{thermal}}(x, y) = A e^{-\frac{(x-x_0)^2}{2\sigma_x^2}} e^{-\frac{(y-y_0)^2}{2\sigma_y^2}} + b.$$

As evaporative cooling continues the condensate component gradually grows, visible as a dense elliptical core, and the thermal fraction reduces, until an almost pure BEC is obtained. In the case of large BECs with significant mean-field interaction compared to kinetic energy the dense core can be fitted by

$$n_{\text{BEC}}(x, y) = A \text{Max} \left[ 0, \left( 1 - \frac{(x-x_0)^2}{\sigma_x^2} - \frac{(y-y_0)^2}{\sigma_y^2} \right)^{3/2} \right] + b,$$

where  $A$  is the peak density,  $x_0$  and  $y_0$  are coordinates of the atomic cloud center,  $\sigma_x$  and  $\sigma_y$  are widths of the distribution and  $b$  is an offset. For image analysis we fit with a bimodal distribution in the form

$$n_{\text{bimodal}}(x, y) = n_{\text{thermal}}(x, y) + n_{\text{BEC}}(x, y).$$

<sup>9</sup>In the presence of the BEC component a more rigorous approach is based on a Bose-enhanced Gaussian distribution [119].

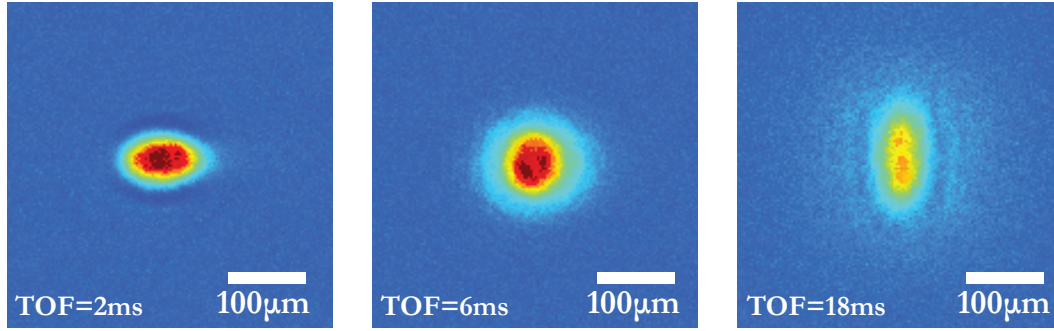


**Figure 3.11: Absorption images, showing an inversion of the aspect ratio during the free expansion of the atomic cloud.** To obtain these images evaporation is stopped before reaching a pure condensate, therefore the BEC coexists and overlaps with a thermal fraction. The presence of the thermal fraction is clearly noticeable on the last image and it does not hinder the observation of the aspect ratio inversion.

At the end of evaporation we routinely obtain almost pure BECs of  $^{84}\text{Sr}$  with about  $10^5$  atoms (Figure 3.9).

Another hallmark of the BEC is an inversion of the aspect ratio during the free expansion of the atomic cloud [120].<sup>10</sup> The velocity distribution obtained by releasing the thermal gas is isotropic regardless of the initial trapping potential. Contrarily, for a BEC the anisotropy of the trapping potential is revealed due to a release of the mean field energy primarily in the direction of the tighter confinement [122]. This anisotropic release is easily observed with the time-of-flight method from an anisotropic ODT even in the presence of a significant thermal fraction, providing another distinctive signature of the condensate (Figure 3.11) [123].

### 3.6 Degenerate Fermi gas of $^{87}\text{Sr}$

Achieving quantum degeneracy with Fermi gases in 1999 introduced a new outstanding experimental platform, complementing BECs and extending the sphere of applications for ultracold gases to fermionic statistics [124].

The unique properties of fermionic strontium are key beneficial features in a number of exciting proposals (a few possibilities are listed in Chapter 1). Among alkaline-earth-like elements, strontium stands out by its large nuclear spin and the related rich energy level structure. The narrow intercombination lines  $^1S_0 - ^3P_{0,2}$

<sup>10</sup>A similar evolution of the aspect ratio during the free expansion is an inherent trait of a thermal cloud in the hydrodynamic regime. Therefore a more detailed analysis is necessary to unambiguously distinguish a condensate from a classical gas [121].

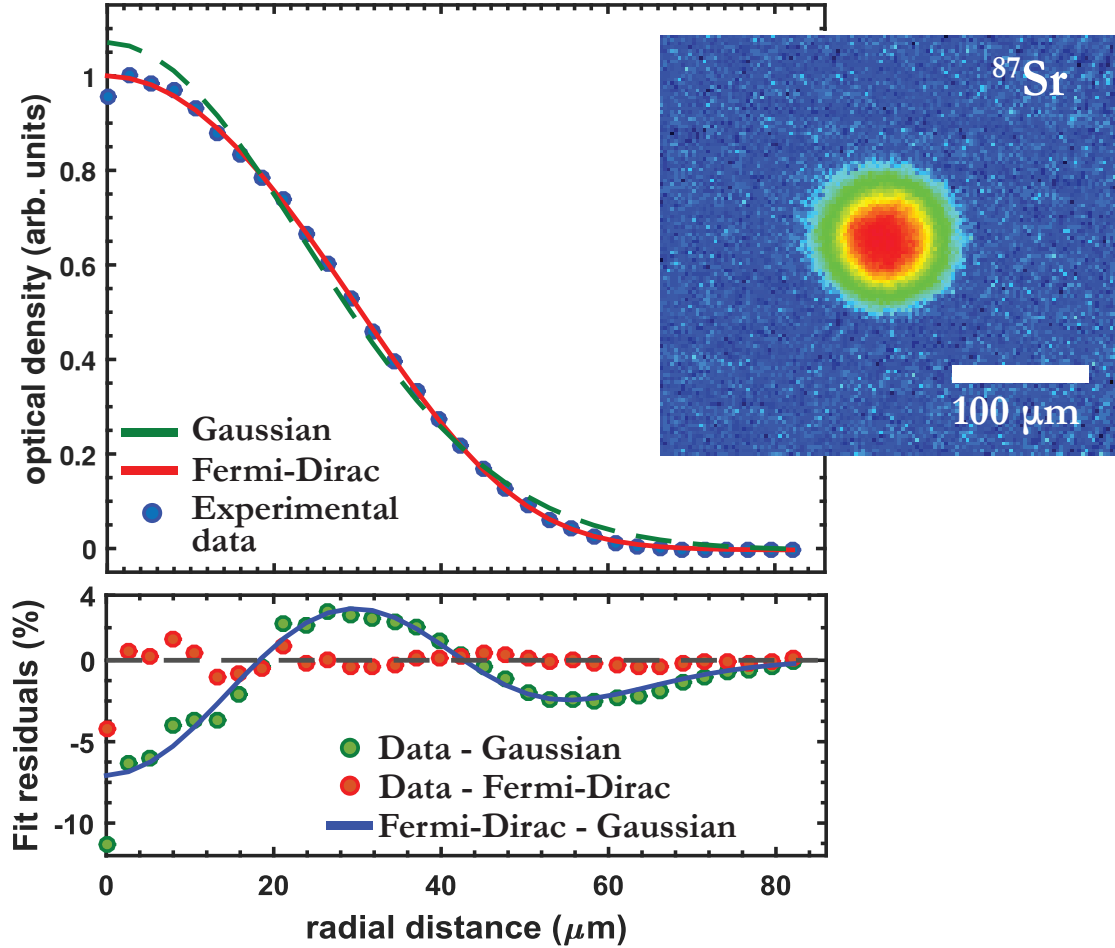


**Figure 3.12: Degenerate Fermi gas of fermionic strontium.** (Top) Blue points represent the azimuthally averaged optical density of the absorption image shown in the inset, which was taken after 10 ms of free expansion. For the shown atomic cloud  $T/T_F$  is  $\sim 0.2$ . The Fermi-Dirac fit (solid red line) captures distinct features of the data, in contrast to the Gaussian fit (dashed green line), which shows noticeable deviations at the center and in the wings. Fit parameters are determined before azimuthal averaging by using two-dimensional functions. (Bottom) The residuals of the fits demonstrate the discrepancies of the Gaussian fit (green point) and the Fermi-Dirac fit (red points) from the experimental data; the solid curve indicates the difference between two residuals.

have a special importance for applications. The non-magnetic  $^1S_0 - ^3P_0$  transition is used in optical lattice clocks and the  $^1S_0 - ^3P_2$  transition can be used for nuclear spin-state specific manipulation of the atoms, e.g. Raman coupling, AC Stark shifting or shelving. In the bosonic isotopes these strongly forbidden transitions need to be opened up by applying external fields [125]. In the fermionic isotope the hyperfine interaction mixes  $5s5p^3P_J$  and  $5s5p^1P_1$  states, leading to weak opening of  $^1S_0 - ^3P_{0,2}$  transitions to linewidths of around 1 mHz [126, 127], which is convenient for many applications.

To realize many of the intriguing theoretical proposals a deeply degenerate Fermi gas is highly preferable to a thermal gas. The cooling strategy to achieve the DFG with strontium is similar to the one used to create Sr BECs and it is based on forced evaporation in the dipole trap. However, the fundamental difference is a smooth crossover to the quantum regime in contrast to the bosonic isotopes, which exhibit a phase transition. Another important distinction is inhibited  $s$ -wave scattering in a single component Fermi gas due to the Pauli exclusion principle for identical fermions. A crucial consequence of this principle is hampering of the thermalization process, which renders evaporative cooling of a spin-polarized Sr Fermi gas impossible. A simple approach to overcome this difficulty is to use a mixture of atoms in different nuclear spin states, as naturally obtained during the operation of the rMOT. Using a mixture of atoms in all ten nuclear spin states allows  $s$ -wave collisions between nearly all atoms, resulting in the lowest temperature as measure in units of the Fermi temperature ( $T/T_F$ ) [94]. A mixture of two states is sufficient to guarantee proper thermalization and to reach quantum degeneracy. For a two component mixture the performance is limited by the fact that the possible number of collisions is two times smaller than for distinguishable particles. In experiments in which a fully spin-polarized degenerate Fermi gas is required, an established approach is to use sympathetic cooling with another isotope, for example  $^{84}\text{Sr}$  [4].

Detecting the onset of quantum degeneracy for fermions is more subtle than for bosons. The main feature that distinguishes the degenerate Fermi gas from a thermal gas is a change in the momentum distribution (Figure 3.12). This change is detected by analyzing time-of-flight absorption images of the atomic cloud released from the trap [89, 128]. Each image is fit by two-dimensional distributions, one corresponding to the Maxwell-Boltzmann statistics and having the Gaussian shape

$$n_{\text{Gaussian}}(x, y) = A e^{-\frac{(x-x_0)^2}{2\sigma_x^2}} e^{-\frac{(y-y_0)^2}{2\sigma_y^2}} + b$$

and the other corresponding to the Fermi-Dirac statistic with a shape defined by

$$n_{\text{FD}}(x, y) = A \frac{\text{Li}_2 \left[ -\xi e^{-\frac{(x-x_0)^2}{2\sigma_x^2}} e^{-\frac{(y-y_0)^2}{2\sigma_y^2}} \right]}{\text{Li}_2[-\xi]} + b,$$

where  $\xi$  is the fugacity,  $A$  is the peak density,  $b$  is an offset and  $\text{Li}_n$  is the  $n^{\text{th}}$ -order polylogarithm. For high temperatures ( $T \gg T_F$ ) these two fit functions are very similar, but in the degenerate regime the second flattens and broadens compared to the first. This difference in shape is due to the Pauli exclusion principle, which restricts the occupation number to one identical particle per state and its influence is more pronounced for states at low momentum. Comparing the quality of the two fits allows us to determine if we have reached the regime of quantum degeneracy.

The level of degeneracy is characterized by the ratio of the atomic cloud temperature to the Fermi temperature. This parameter can be quantified by two approaches. The first one relies on analyzing the shape of the momentum distribution: the fugacity is used as a fit parameter and the ratio  $T/T_F$  is calculated with the equation

$$T/T_F = (-6\text{Li}_3[-\xi])^{-\frac{1}{3}}.$$

The second approach is based on analyzing absorption images and retrieving a temperature  $T$  and a number of atoms  $N$ , which is used to calculate

$$T_F = \frac{\hbar\bar{\omega}}{k_B} (6N)^{\frac{1}{3}},$$

where  $\bar{\omega} = (\omega_x\omega_y\omega_z)^{1/3}$  is the geometric mean of the trap frequencies. We rely on both methods to accurately distinguish the regime of quantum degeneracy from the classical regime [4, 89].

Obtaining a DFG is a crucial step towards exploring many of the theoretical proposals that are appealing to be pursued with our experimental system. We cool the fermionic isotope to degeneracy in a similar way to the bosonic case. From the rMOT the atoms are loaded into the dipole trap, where they are further cooled by evaporation [3, 4]. Currently we use a roughly equal mixture of the ten nuclear spin states and the primary reason for this approach is the simplified evaporative cooling procedure, since distinguishable fermions thermalize. We routinely prepare degenerate Fermi gases of  $\sim 7 \times 10^4$  atoms distributed over all ten states with  $T/T_F \sim 0.2$  at  $T \sim 40$  nK. The created atomic cloud is a collection of ten spatially overlapped degenerate Fermi seas, each corresponding to a different nuclear spin state.

When designing and assembling a new apparatus in our field, achieving degenerate gases is a critical step, establishing the foundation for investigating exciting questions in quantum physics. By inheriting knowledge and experience from previous explorations, we demonstrate successful quantum gas creation with ultracold strontium. In the last two chapters I described the construction of our new experiment from empty optical tables to the creation of the first quantum gases with this machine.

# Chapter 4

## The frequency of the ultranarrow $^1S_0 - ^3P_2$ transition in $^{87}\text{Sr}$

### 4.1 Introduction

Atoms with two valence electrons, such as the alkaline-earth metals or ytterbium, possess ultra-narrow intercombination transitions from their singlet ground state to metastable triplet states. The  $^1S_0 - ^3P_0$  transition, which connects two states that are free of electronic magnetic moment, is used as frequency reference in optical atomic clocks [129] and is of interest for quantum simulation [130–134], computation [25, 135, 136], and gravitational wave detection [137–139]. The  $^1S_0 - ^3P_2$  transition is equally narrow [127], but it connects the ground state to an excited state with electronic magnetic moment. This property has enabled high-resolution imaging of an Yb quantum gas in a magnetic field gradient [140, 141], a method that could also provide selective access to qubits in a quantum computer [25, 135]. Isotopes with nuclear spin exhibit hyperfine structure in the  $^3P_2$  state, which will make it possible to induce nuclear spin state specific ac Stark shifts and Raman couplings using the  $^1S_0 - ^3P_2$  transition. This property might allow the creation of artificial gauge fields that are significantly less hampered by off-resonant scattering of photons or collisions between metastable state atoms compared to schemes exploiting broader transitions [45, 142–145] or using metastable atoms [131, 133, 146]. Ultracold mixtures containing  $^3P_2$  atoms have been obtained from quantum gases of ground state atoms by excitation on the  $^1S_0 - ^3P_2$  transition, leading to the discovery of Feshbach

---

The content of this chapter has been published as Phys. Rev. A **99**, 052503 (2019).

resonances between Yb  $^1S_0$  and  $^3P_2$  atoms [147]. These resonances are interesting for quantum information processing [25, 135, 136], are predicted to show signatures of quantum chaos [148] and have been exploited to form Feshbach molecules [149, 150]. Also mixtures of  $^3P_2$  Yb with Li have been created [151, 152] and their collisional stability investigated [153–157]. The  $^1S_0 - ^3P_2$  transition might also be useful to create quantum gases with quadrupole interactions [158–162].

Many of these applications require quantum degenerate gases and so far three two-valence-electron elements have been cooled to quantum degeneracy: Yb [163], Ca [164], and Sr [1]. The frequency of the  $^1S_0 - ^3P_2$  transition is only well known for Yb. Strontium has properties that significantly distinguish it from Yb, offering different opportunities. It enables higher phase space densities directly by laser cooling, which makes it possible to create quantum gases with large atom number or with high repetition rate [94]. Its fermionic isotope  $^{87}\text{Sr}$  has a nuclear spin of  $9/2$ , which should enable better Pomeranchuk cooling [165, 166] or larger synthetic dimensions [167]. In order to combine these favorable properties with the possibilities offered by the  $^1S_0 - ^3P_2$  transition, the frequency of this transition needs to be determined to at least the megahertz level.

In this article we report the measurement of the ultra-narrow  $^{87}\text{Sr } ^1S_0 - ^3P_2$  transition by direct optical excitation. We perform loss spectroscopy of an ultracold strontium sample and determine the resonance frequency by comparison to four spectral lines of molecular iodine, which serves as a natural and documented reference. The iodine lines are identified by comparing a gigahertz-wide iodine spectrum around the Sr lines with the spectra calculated by the IODINESPEC5 software [168]. The accuracy of the measurement is limited by the uncertainty in iodine transition frequencies, whereas the precision is limited by frequency drifts of an optical resonator used for spectroscopy laser stabilization. The relative frequency between the Sr transition and specific iodine lines is obtained with an accuracy of 0.5 MHz and the absolute frequency is limited by the iodine line accuracy of 30 MHz. These measurements open the door to using the Sr  $^1S_0 - ^3P_2$  transition for important applications, such as the creation of artificial gauge fields or quantum computation.

This article has the following structure: Sec. 4.2 describes the spectroscopy laser system, the iodine spectroscopy setup, and Sr sample preparation; Sec. 4.3 introduces relevant Sr transitions, presents initial coarse and final precise determination of the  $^1S_0 - ^3P_2$  transition frequency and analyzes the measurement error. Conclusions are given in Sec. 4.4.

## 4.2 Experimental details

### 4.2.1 $^1S_0 - ^3P_2$ spectroscopy laser setup

Light for the spectroscopy of Sr and iodine is produced by an external cavity diode laser (ECDL; wavelength: 671 nm; power: 24 mW; diode: Toptica LD-0670-0035-AR-1), see Fig. 4.1. The ECDL is locked to an optical resonator by the Pound-Drever-Hall (PDH) method [169]. The resonator uses a Zerodur spacer, is length-tunable by two piezos that compensate each other's thermal expansion [70], and is kept under vacuum, with the vacuum chamber placed inside a thermally insulating box. A frequency shift of 550 MHz to 850 MHz is introduced by an acousto-optic modulator (AOM) between the ECDL and the light used for locking. Spectroscopy scans are performed by slowly varying the AOM frequency so that the lock follows. The feedback loop uses a fast proportional-integral-differential (PID) controller (Toptica FALC 110), providing feedback of 1.9 MHz bandwidth to the ECDL current and 10 kHz bandwidth to the ECDL grating. Based on the error signal, we estimate the laser linewidth to be at most 85 kHz. The light is sent through polarization-maintaining single-mode optical fibers to the Sr sample and to the iodine spectroscopy setup. The absolute frequency of the spectroscopy laser can be obtained with a wavemeter (Toptica HighFinesse WSU-30, accuracy of 30 MHz) calibrated to the frequency of the 7.4 kHz-wide  $^1S_0 - ^3P_1$  transition of  $^{88}\text{Sr}$ , known to within 10 kHz [170]. The calibration laser's absolute frequency is determined by spectroscopy of a Sr Bose-Einstein condensate to better than 50 kHz and its frequency stability is better than 10 kHz, as verified by successful operation of a  $^1S_0 - ^3P_1$  line magneto-optical trap (MOT). The wavemeter calibration is done each day immediately before the data collection runs using the designated calibration port of the wavemeter.

### 4.2.2 Iodine spectroscopy setup

Spectra of iodine molecule vapor (natural sample, essentially 100%  $^{127}\text{I}_2$  [171]) contained in a heated quartz cell are recorded using Doppler-free saturated absorption spectroscopy [172, 173]. We will now briefly describe the  $\text{I}_2$  spectroscopy setup, see Fig 4.1. The quartz cell is 60 cm long and kept at approximately 530 °C (not stabilized by feedback) in order to populate the higher vibrational levels of the iodine molecule [173]. A cold finger, stabilized at 20.0(3) °C, is used to set the io-

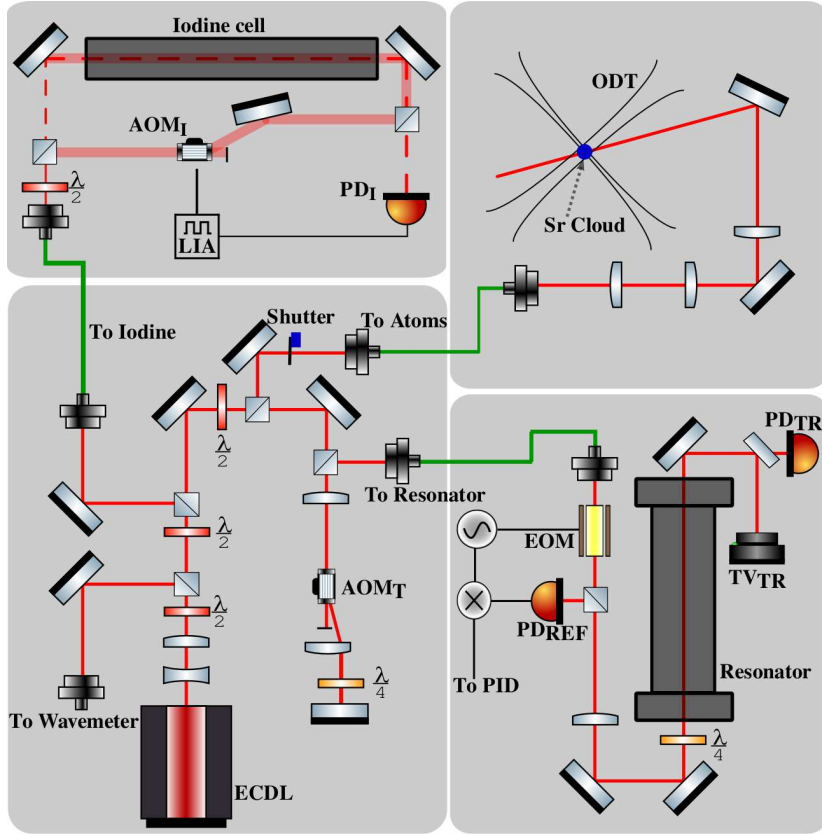


**Figure 4.1:** Scheme of the spectroscopy setup. The light of an extended cavity diode laser (ECDL) is distributed to a wavemeter, an optical resonator, an iodine spectroscopy setup, and Sr samples in an optical dipole trap (ODT). The laser frequency is stabilized to a mode of an optical resonator. Acousto-optic modulator  $\text{AOM}_T$  introduces a controlled offset between the laser light and the resonator mode and is used to perform spectroscopy scans. To lock the light to the resonator the Pound-Drever-Hall method is used, for which an electro-optic modulator (EOM) creates sidebands on the light sent to the resonator and photodiode  $\text{PD}_{\text{REF}}$  measures the light intensity reflected from it. The light transmitted through the resonator is analyzed by TV camera  $\text{TV}_{\text{TR}}$  and photodiode  $\text{PD}_{\text{TR}}$ . The laser frequency can be referenced to iodine lines using the iodine spectroscopy setup, consisting of an iodine vapor cell,  $\text{AOM}_I$ ,  $\text{PD}_I$ , and a lock-in amplifier (LIA).

dine partial pressure. The collimated spectroscopy beam entering the setup (waist 0.7 mm, power 5 mW) is split into a pump and a probe beam. The probe beam (power 0.5 mW) is sent through the cell onto a photodiode that records the spectroscopy signal. The pump beam is frequency shifted by acousto-optic modulator  $\text{AOM}_I$ , after which it has approximately 3 mW of power, and gets sent through the

iodine cell in a counterpropagating manner with respect to the probe<sup>1</sup>. We enhance the weak Doppler-free signal by lock-in detection. We use AOM<sub>I</sub> to chop the pump beam at 50 kHz (square wave) and we demodulate the detected probe signal at that frequency on a lock-in amplifier (EG & G Instruments Model 7265) using a time constant of 100 ms. A few things are worth mentioning about this approach: first of all, the lock-in method is necessary, because the bare Lamb dips in the Doppler spectrum are too weak to be seen directly with the available power; secondly, the method is quite forgiving in terms of the chopping frequency, and in particular, the chopping frequency can be increased if one wants to reduce the time constant of the lock-in for faster scans, at the expense of signal-to-noise<sup>2</sup>; thirdly, the method is forgiving to slight misalignment in the overlap of the pump and probe beams, imperfect collimation of the beams, and slight power fluctuations of pump and probe.

### 4.2.3 Strontium sample preparation and spectroscopy principle

Spectroscopy of the Sr  $^1S_0 - ^3P_2$  transition is done on an ultracold cloud of  $^{87}\text{Sr}$  in an equal mixture of all nuclear spin states contained in an optical dipole trap (ODT). The ODT consists of two horizontally propagating, linearly-polarized 1064 nm beams crossing at right angles and having waists of approximately 70  $\mu\text{m}$  and 60  $\mu\text{m}$  and powers of 2.2 W and 1.2 W; the beams have a 160 MHz frequency difference in order to avoid mutual interference. To prepare the sample, a magneto-optical trap is loaded from a Zeeman-slowed atomic beam and then transferred into the ODT using the techniques described in Ref. [94]. We obtain a cloud of  $2 \times 10^5$  Sr atoms at 730 nK, which has a  $1/e$ -width of  $\sim 25 \mu\text{m}$  in the vertical direction and  $\sim 38 \mu\text{m}$  in the horizontal direction. We reduce the residual magnetic field to less than 30 mG at the location of the atomic cloud. The Sr spectroscopy beam is focused to a waist of about 60  $\mu\text{m}$  at the sample position. Spectroscopy is performed time sequentially and measures frequency dependent loss of ground state atoms. A sample is prepared, exposed to spectroscopy light, which leads to atom loss, and the remaining ground-state atom number is detected by absorption imaging on the  $^1S_0 - ^1P_1$  transition.

<sup>1</sup>AOM<sub>I</sub> introduces the frequency shift of approximately  $\nu_{\text{AOM}_I}/2 = 35$  MHz between the frequency of the iodine transition under study  $\nu_{I_2}$  and the frequency of the spectroscopy beam entering the setup  $\nu_{\text{spec}}$ :  $\nu_{I_2} = \nu_{\text{spec}} - \nu_{\text{AOM}_I}/2$ .

<sup>2</sup>The chopping frequency cannot be much larger than roughly one linewidth of the transition that one tries to observe [174].

### 4.3 Determination of the $^1S_0 - ^3P_2$ transition frequency

Strontium levels and transitions that are relevant for this work are shown in Fig. 4.2. The transitions  $^1S_0 - ^3P_{0,2}$  are dipole forbidden in isotopes with pure spin-orbit (LS) coupling because of spin and total angular momentum selection rules [126]. A small dipole matrix element can be induced by mixing of the  $^3P_{0,2}$  states with  $^1P_1$  through the application of a magnetic field or through hyperfine coupling in the case of  $^{87}\text{Sr}$ , the only stable Sr isotope with nuclear spin. For the bosonic  $^{88}\text{Sr}$  the observation of the  $^1S_0 - ^3P_0$  clock transition has been reported with an external mixing field as low as 13 G [65, 125]. Most Sr optical lattice clocks use fermionic Sr in order to exploit hyperfine mixing to enable the clock transition.

In this work we use fermionic  $^{87}\text{Sr}$ , which allows dipole transitions between  $^1S_0$  ( $F = 9/2$ ) and  $^3P_2$  ( $F' = \{7/2, 9/2, 11/2\}$ ) with a linewidth of approximately 1 mHz by hyperfine mixing [127]. The transitions  $^1S_0$  ( $F = 9/2$ ) –  $^3P_2$  ( $F' = \{5/2, 13/2\}$ ) have  $\Delta F = \pm 2$  and the ground and excited states have opposite parity, which makes them dipole forbidden. They are however still accessible as magnetic quadrupole transitions (M2) [175] and we observe the  $^1S_0$  ( $F = 9/2$ ) –  $^3P_2$  ( $F' = 5/2$ ) transition.

We determine the  $^1S_0 - ^3P_2$  transition frequency in two steps. The first step, described in Sec. 4.3.1, determines the transition indirectly to within  $\sim 100$  MHz. This is sufficiently precise to find the transition with direct spectroscopy, see Sec. 4.3.2. In Sec. 4.3.3 we discuss the error of our measurement.

#### 4.3.1 Coarse, indirect determination

The  $^1S_0 - ^3P_2$  transition frequency has only been measured for the most abundant isotope  $^{88}\text{Sr}$  with an accuracy of 120 MHz [176]. The  $^{87}\text{Sr}$   $^1S_0 - ^3P_2$  transition frequencies can be estimated by adding the  $^{87}\text{Sr}$   $^3P_2$  hyperfine shifts, which have been determined by radiofrequency spectroscopy in hot Sr [177], and the isotope shift. Here we assume that the  $^1S_0 - ^3P_2$  isotope shift is the same as the measured  $^1S_0 - ^3P_0$  and  $^1S_0 - ^3P_1$  isotope shifts [178–180], which are both within 1 MHz of  $f_{88} - f_{87} = 62$  MHz. We verify the estimated transition frequency by performing a simple, coarse and indirect frequency determination. We determine  $f(^1S_0 - ^3P_2)$  using conservation of energy: we measure  $f(^3P_2 - ^3S_1)$  and use the well-known transition frequencies  $f(^1S_0 - ^3P_0)$  and  $f(^3P_0 - ^3S_1)$  [181] to calculate  $f(^1S_0 - ^3P_2)$  (see Fig. 4.2). The  $^3P_2 - ^3S_1$  transition is dipole allowed, which makes it much broader and easier find than the doubly forbidden millihertz-linewidth  $^1S_0 - ^3P_2$  transition.

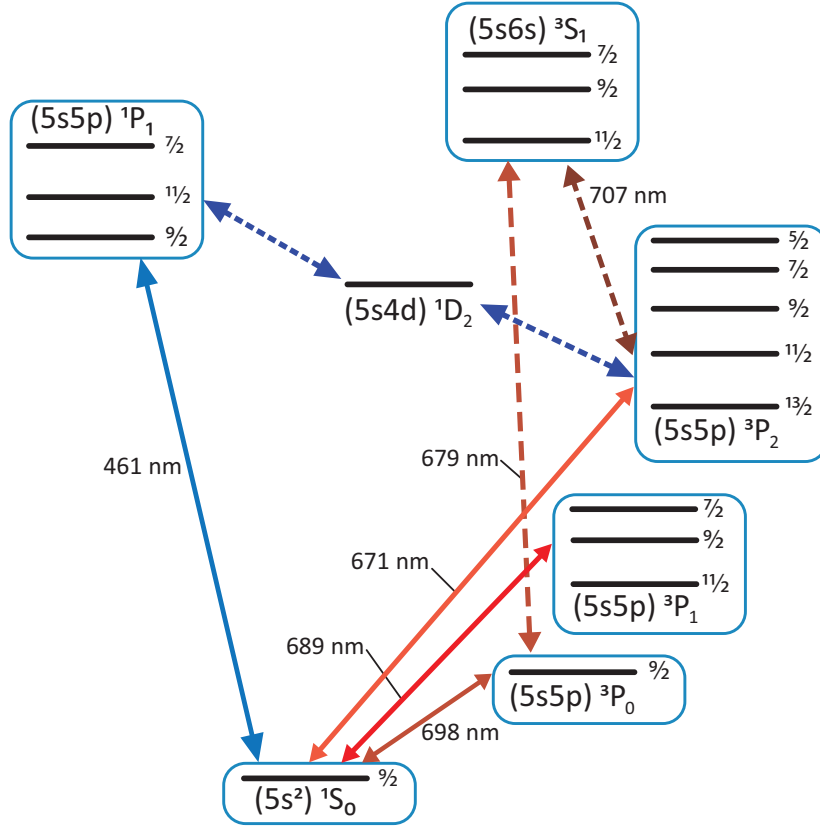


**Figure 4.2:** Level scheme of the low-lying electronic states of  $^{87}\text{Sr}$ . The transitions at 461 nm and 689 nm are used for MOTs, the transitions at 679 nm and 707 nm are repump transitions, the one at 698 nm is the clock line, and the transition at 671 nm is the  $^1S_0 - ^3P_2$  line whose frequency we measure in this work. The hyperfine structure of the  $^1D_2$  is neglected because it is irrelevant for this work.

Similar schemes were used to determine the Sr  $^1S_0 - ^3P_0$  transition [181] and the Yb  $^1S_0 - ^3P_2$  transition [182].

To determine  $f(^3P_2 - ^3S_1)$  we use reservoir spectroscopy [92]. This technique relies on the fact that atoms in the  $^1S_0 - ^1P_1$  MOT cycle can decay through the  $^1D_2$  state into the metastable and magnetic  $^3P_2$  state, the low field seeking  $m_F$  substates of which are captured in the magnetic quadrupole field of the MOT. These atoms can be pumped back into the MOT cycle with light on a transition from the  $^3P_2$  state to some higher-lying state that has a high chance of decaying into the ground state. We use the  $^3S_1$  state as the higher-lying state, from which atoms decay to the ground state through the short-lived  $^3P_1$  state. The  $^3P_2 - ^3S_1$  transition corresponds to a repump laser operating around 707 nm. Thus, when the repump laser is tuned to a resonance, the  $^3P_2$  atoms from the magnetically trapped reservoir are quickly brought back into the  $^1S_0 - ^1P_1$  MOT cycle, rapidly increasing the number of

ground-state atoms and causing a MOT fluorescence flash. There are nine repump resonances due to the number of hyperfine states in both  $^3P_2$  and  $^3S_1$ , but we do not need to measure all of those transitions to determine  $f(^3P_2 - ^3S_1)$ .

We observe three  $^3P_2 - ^3S_1$  repump resonances, which we can attribute to specific transitions between hyperfine states in the  $^3P_2$  and  $^3S_1$  manifolds using knowledge of the  $^3P_2$  hyperfine structure [177], knowledge of the  $^3S_1$  hyperfine structure [181], and selection rules. The absolute frequencies of these transitions are obtained with the wavemeter that is also part of the  $^1S_0 - ^3P_2$  spectroscopy setup. These measurements, combined with the known transition frequencies  $f(^1S_0 - ^3P_0)$  and  $f(^3P_0 - ^3S_1)$  [181], provide estimates of the individual transition frequencies  $f[^1S_0 (F = 9/2) - ^3P_2 (F' = \{7/2, 9/2, 11/2\})]$ . This determination has an accuracy of  $\sim 100$  MHz and confirms the estimated transition frequencies. Using this good starting point we now expect to find the transitions quickly in a direct spectroscopy search.

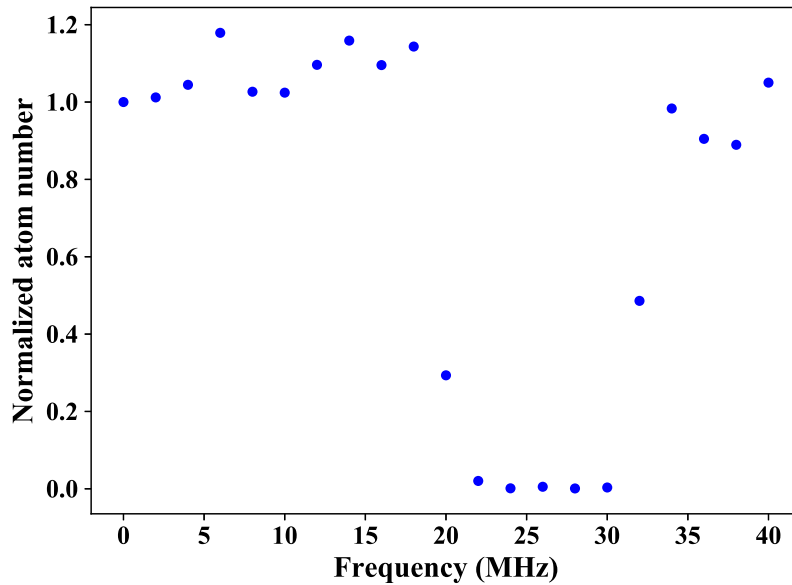


**Figure 4.3:** Spectrum of the  $^1S_0 (F = 9/2) - ^3P_2 (F' = 11/2)$  transition broadened by using a large Rabi frequency (spectroscopy laser power of 4.5 mW). The zero of the frequency axis is chosen arbitrarily.

### 4.3.2 Precise, direct determination

We perform direct spectroscopy of the  $^1S_0 - ^3P_2$  transitions using Sr samples in an ODT. When the spectroscopy laser is tuned into resonance, ground-state atoms are excited to the metastable  $^3P_2$  state. Atoms in this state are transparent to the  $^1S_0$

### 4.3. DETERMINATION OF THE $^1S_0 - ^3P_2$ TRANSITION FREQUENCY

-  $^1P_1$  absorption imaging beam and furthermore likely lost by inelastic collisions [183]. To find a resonance we measure the fraction of  $^1S_0$  atoms remaining in the ODT as a function of spectroscopy laser frequency, while keeping other parameters, such as illumination time and laser power, constant. During the first search for the transition we use the full power of the spectroscopy beam (4.5 mW). We repeatedly prepare Sr samples and use each to scan a 1 MHz frequency interval over 1 s. An example for the resulting spectrum is shown in Fig. 4.3 and determines all  $^1S_0 - ^3P_2$  transitions to within 10 MHz, using the known  $^3P_2$  hyperfine splittings.

$F'$	Frequency [MHz]	FWHM linewidth [MHz]
7/2	446 648 769(30)	0.52(4)
9/2	446 647 793(30)	0.74(3)
11/2	446 646 618(30)	0.69(8)

**Table 4.1:** Frequencies and measured linewidths of the  $^1S_0 - ^3P_2$  transition to three different hyperfine states in the  $^3P_2$  manifold. The frequencies are determined using a wavemeter, whereas the full-width half-maximum (FWHM) linewidths are obtained from Gaussian fits to the spectroscopy signals shown in Fig. 4.4.

In order to determine the transition frequency with more precision we zoom in on the detected broad spectroscopy signals by recording spectra with 0.45 mW of spectroscopy laser power and reduced frequency interval and illumination time per sample. The narrowest spectroscopy signals for  $F' = \{7/2, 9/2, 11/2\}$  are shown in Fig. 4.4 together with Gaussian fits, the parameters of which are summarized in Table 4.1. The values of the transition frequencies measured with the wavemeter are also reported in Table 4.1, and the uncertainty is dominated by wavemeter inaccuracy.

Next we determine the frequency difference between four iodine transitions and the  $^{87}\text{Sr } ^1S_0 (F = 9/2) - ^3P_2 (F' = 7/2)$  transition. This allows us to determine the frequency of the Sr transition with the accuracy of the known iodine transition frequencies, which currently is the same as the accuracy of the wavemeter (30 MHz), but can be improved in the future with iodine spectroscopy alone [173]. More importantly the accuracy of the frequency difference (0.5 MHz) is much higher than the accuracy of the absolute frequency, which makes it possible to find the Sr transition with simple iodine spectroscopy and to lock the Sr laser to iodine lines.

The  $F' = 7/2$  state is used for iodine comparison because it is within the spec-

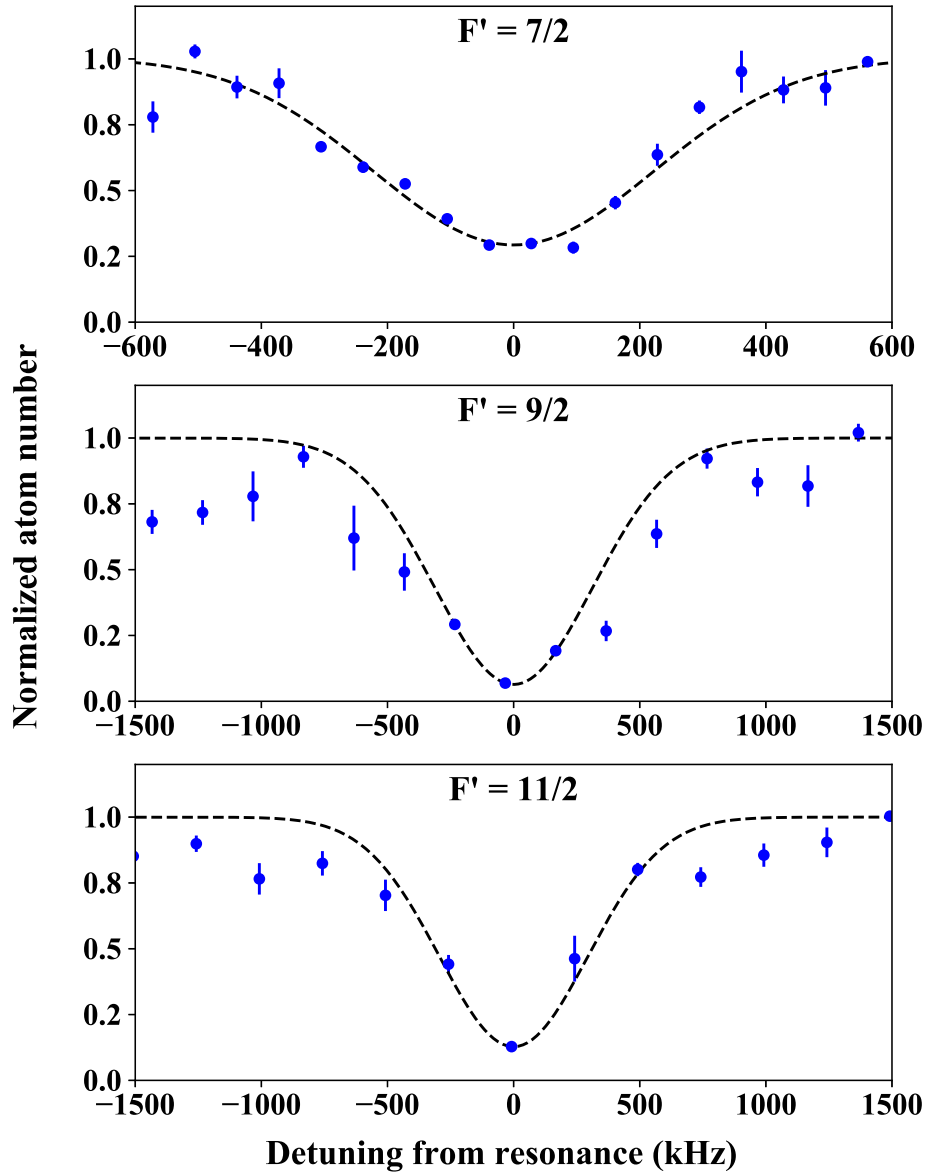


**Figure 4.4:** High-resolution spectra of the  $^1S_0 - ^3P_2$  ( $F' = \{7/2, 9/2, 11/2\}$ ) transition in  $^{87}\text{Sr}$  measured by atom loss spectroscopy in an ODT using low spectroscopy beam power (0.45 mW). The atom numbers are normalized to the ones far away from any spectroscopy signal. The error bars represent the standard error of five measurements per data point.

### 4.3. DETERMINATION OF THE $^1S_0 - ^3P_2$ TRANSITION FREQUENCY

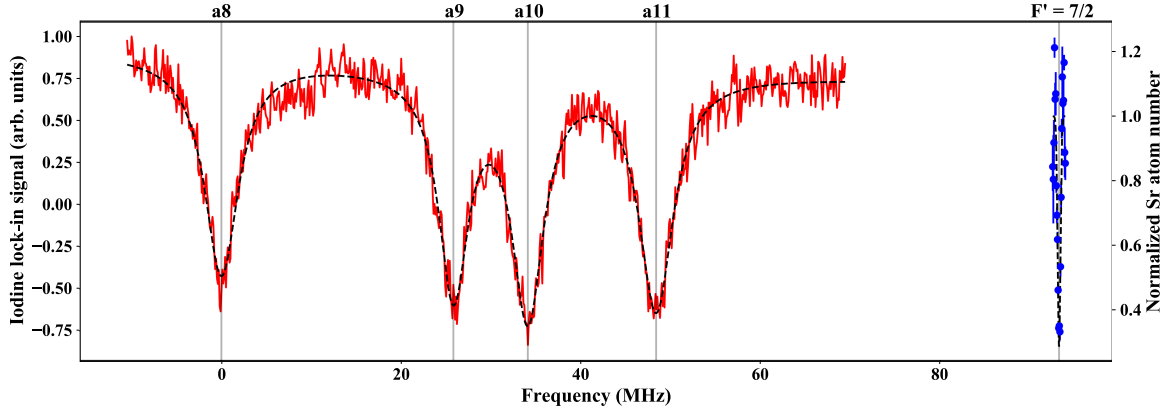


**Figure 4.5:** Combined spectrum of the  $^{87}\text{Sr } ^1S_0 - ^3P_2$  ( $F' = 7/2$ ) line and iodine lines {a8, a9, a10, a11}. The red line is iodine data, the blue circles are  $^{87}\text{Sr}$  data, the black dashed lines are the fits to the respective spectra (multiple Lorentzian for iodine and Gaussian for  $^{87}\text{Sr}$ ). The center of each fitted spectral line is marked with a vertical gray line and labeled on top. The center of the a8 line is chosen as the zero of the frequency axis.

troscopy AOM tuning range of the strong iodine transitions ( $J' - J'' = 32 - 33$ )( $\nu' - \nu'' = 9 - 9$ ) {a8, a9, a10, a11}<sup>3</sup>. The frequencies corresponding to the other hyperfine states in the  $^3P_2$  manifold can be found by using this frequency and the known  $^3P_2$  hyperfine splittings [177]. Figure 4.5 presents an example of a recorded iodine spectrum (scan time 1.5 minutes), fitted with Lorentzians, combined with the Sr spectrum, fitted with a Gaussian. In order to estimate the drift of the spectroscopy laser, we record four iodine spectra within a 2.5 hour interval that encompasses the  $^{87}\text{Sr } ^1S_0$  ( $F = 9/2$ ) -  $^3P_2$  ( $F' = 7/2$ ) frequency measurement. The maximum change of the relative frequency between the iodine laser and the iodine lines is 250 kHz. Since the iodine line frequency is expected to change much less than that we attribute this frequency shift mainly to the lock of the spectroscopy laser to the reference cavity. Table 4.2 lists the fitted central frequency values of the iodine transitions, where each value is an averaged result from the fits to four measured spectra. Using the a8 frequency calculated by IODINESPEC5 we obtain 446 648 775(30) MHz for the  $^{87}\text{Sr } ^1S_0$  ( $F = 9/2$ ) -  $^3P_2$  ( $F' = 7/2$ ) transition frequency, which is consistent with the frequency determined by the wavemeter.

The frequency of the  $^1S_0 - ^3P_2$  ( $F' = 5/2, 13/2$ ) M2 transitions can be determined from the previous measurement and the  $^3P_2$  hyperfine splittings. Guided by this calculation we observe the  $^1S_0 - ^3P_2$  ( $F' = 5/2$ ) transition by direct optical excitation.

<sup>3</sup>Here,  $J''$  and  $\nu''$  denote the lower rotational and vibrational levels respectively, and  $J', \nu'$  denote the upper level. The symbols {a8, a9, a10, a11} label the hyperfine states [168]. The common designation for these rovibrational transitions is P(33) (9-9).

Transition	frequency (MHz)
a8	0.00(3)
a9	25.88(3)
a10	34.17(5)
a11	48.39(4)
$^1S_0 - ^3P_2 (F' = 7/2)$	93.27(25)

**Table 4.2:** Measured frequencies of the iodine transitions {a8, a9, a10, a11} within the manifold P(33) (9-9) and the  $^1S_0 - ^3P_2 (F' = 7/2)$  transition frequency. The frequencies are reported with respect to the measured frequency of the a8 transition. The iodine transition frequencies are given for our conditions of the iodine cell (see text) and are shifted by  $-100(15)$  kHz with respect to iodine lines at zero pressure and temperature. The error of the Sr transition is dominated by drifts of the reference resonator.

Since it is an M2 transition it is expected to be much weaker than the HFM-E1 lines, and we indeed must use about 10 times larger intensity and a 20 times longer illumination time to induce observable atom loss on this transition compared to the case of the dipole transitions. Fig. 4.6 shows a spectrum of this line recorded with a spectroscopy beam power of 4.5 mW and an illumination time of 10 s.

Based on our measurement of the  $^1S_0 - ^3P_2$  transition and the previously reported results for the  $^1S_0 - ^3P_1$  and  $^3P_1 - ^3S_1$  transition frequencies and hyperfine splittings of all mentioned states [177, 181], we can also give a more accurate value for the  $^3P_2(F = 7/2) - ^3S_1(F' = 7/2)$  repumping transition frequency, which evaluates to 423914969(30) MHz. The corresponding values involving any other hyperfine states can be easily calculated from the known hyperfine splittings [177, 181].

### 4.3.3 Error analysis

We measure absolute frequencies in two ways, using the wavemeter or using iodine lines as reference [168]. Both methods have an uncertainty of 30 MHz, which dominates all other sources of error. We also determine the relative frequency between the Sr transitions and the iodine lines. The error in the relative frequency is much smaller than the absolute error and will be discussed in the following.

The error in the relative frequency measurement has statistical and systematic components. Statistical errors arise from the drifts of the Fabry-Perot resonator to which the laser is locked, from errors in the fits used to determine the center

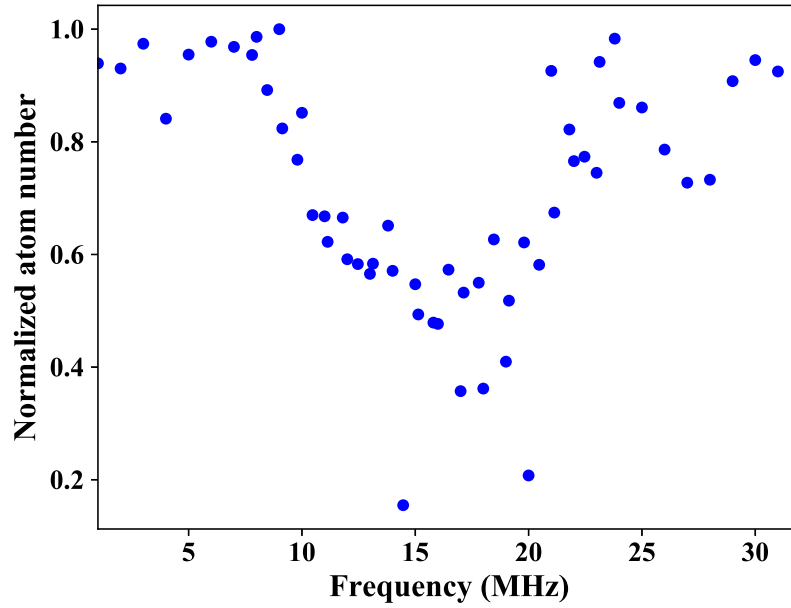


**Figure 4.6:** Spectrum of the  $^1S_0 (F = 9/2) - ^3P_2 (F' = 5/2)$  M2 transition with a spectroscopy beam power of 4.5 mW. The zero of the frequency axis is chosen arbitrarily.

of spectral lines, and from iodine line shifts by iodine temperature and pressure changes<sup>4</sup> [184]. Systematic errors are the collisional shifts of the iodine lines, which effectively move our frequency reference point from its literature value [184], and the ac Stark shift of the Sr transitions by the dipole trap light.

The dominant contribution to the statistical error comes from changes of the cavity resonance to which the spectroscopy laser is locked while the measurements are performed. This error is estimated by recording iodine spectra several times before, during, and after the one-hour timespan during which the Sr spectra are recorded, and then analyzing the drift of the relative frequency between the cavity resonance and the iodine lines. We assume that the iodine lines do not change significantly over this timespan (the validity of that assumption will be analyzed below), therefore the drift is due to changes of the resonator frequency. The maximum drift we observe is 250 kHz.

Errors also originate from pressure and temperature shifts of the iodine lines. Compared to a zero temperature and pressure gas the iodine lines are shifted by  $\delta f_{I_2} = \alpha_S P_2 T^{-7/10}$  at pressure  $P$  and temperature  $T$ , where  $\alpha_S = -400(60)$  kHz K<sup>7/10</sup>/Pa is an empirically determined proportionality constant [184].  $P_2$  is set by the cold finger temperature, and the relevant iodine vapor pressure equation is given in

<sup>4</sup>The AOM frequency uncertainty is negligible compared to other error sources as it is driven by a direct digital synthesizer synchronized to a rubidium atomic clock.

Ref. [173], whereas  $T$  is set by the iodine cell body temperature. Statistical errors arise from uncertainties in  $P$  and  $T$ . The cold finger temperature uncertainty of 0.3 K translates into a pressure uncertainty below 1 Pa. The body temperature has an uncertainty below 20 K. These uncertainties lead to a statistical error of 3 kHz in the iodine line frequency. The systematic shift of the iodine lines is  $\delta f_{I_2} = -100(15)$  kHz, where the dominant contribution to the error arises from uncertainties in  $\alpha_S$ . The values reported in Table 4.2 are given in presence of this shift.

Another source of error is the light shift induced on the Sr transition by the ODT. We obtain an upper limit for this shift by recording spectra using ODT depths up to a factor two higher or lower than the depth used usually. We do not observe a correlation of the transition frequency with the ODT depth, which we attribute to drifts of the reference resonator during the few hours that we spent to record this data. We conclude that the light shifts are at the most on as large as the resonator drifts of 250 kHz, which is consistent with a calculation using the Sr transition strengths of [185]. Adding statistical and systematic errors we arrive at a total error of 0.5 MHz. The Sr spectroscopy lines are broadened by ODT light shifts, the Doppler effect, Zeeman shifts of the unresolved  $m_F$  levels, and collisional effects.

## 4.4 Conclusion

We have determined the frequency of the  $^{87}\text{Sr } ^1S_0 - ^3P_2$  transition with an accuracy of 30 MHz and the frequency difference of that transition to molecular iodine lines with an accuracy of 0.5 MHz. This knowledge enables the use of simple iodine spectroscopy to find the  $^{87}\text{Sr } ^1S_0 - ^3P_2$  transition frequency or to lock a Sr  $^1S_0 - ^3P_2$  laser. Our work prepares the use of this Sr transition for applications, such as quantum simulation or computation.

# Chapter 5

## Towards quantum gas microscopy

The pioneering research on quantum gas microscopy enriched ultracold quantum gas experiments with a new powerful tool, capable of controlling an atomic sample down to the level of single atoms. An essential part of quantum gas microscope experiments is the high resolution imaging system, allowing to reliably manipulate and detect atoms loaded into an optical lattice. A similar technology is employed in optical tweezer experiments to create an array of sub-micron sized dipole traps. Tweezers are a powerful approach to work with single atoms, which allows to assemble quantum systems from the bottom up. Recently several groups have demonstrated the implementation of optical tweezers filled with alkaline-earth-like elements, enhancing the tweezer research field with new species [30–32, 40]. Adding microscope objectives to ultracold atom and quantum gas experiments is one of the most promising ways forward to address challenges in the fields of quantum simulation and computation, and already a number of outstanding results have been achieved [41, 42, 134].

To enrich the toolbox of our experiment and to pursue the field of quantum gas microscopy we designed, assembled and characterized a new microscope objective, which is the crucial part of a high resolution imaging system. The design is tailored to the properties of Sr and our vacuum system, and it has a high enough resolution to enable the creation of optical tweezers or single atom detection in a quantum gas microscope. Our tests show that the objective is constructed according to specifications and works as desired. We have written a manuscript that describes the details of the design, subtleties of the manufacturing process and characterization of the developed objective [186]. Here I will briefly summarize the most important results.

As first experiments with the constructed objective we decided to create opti-

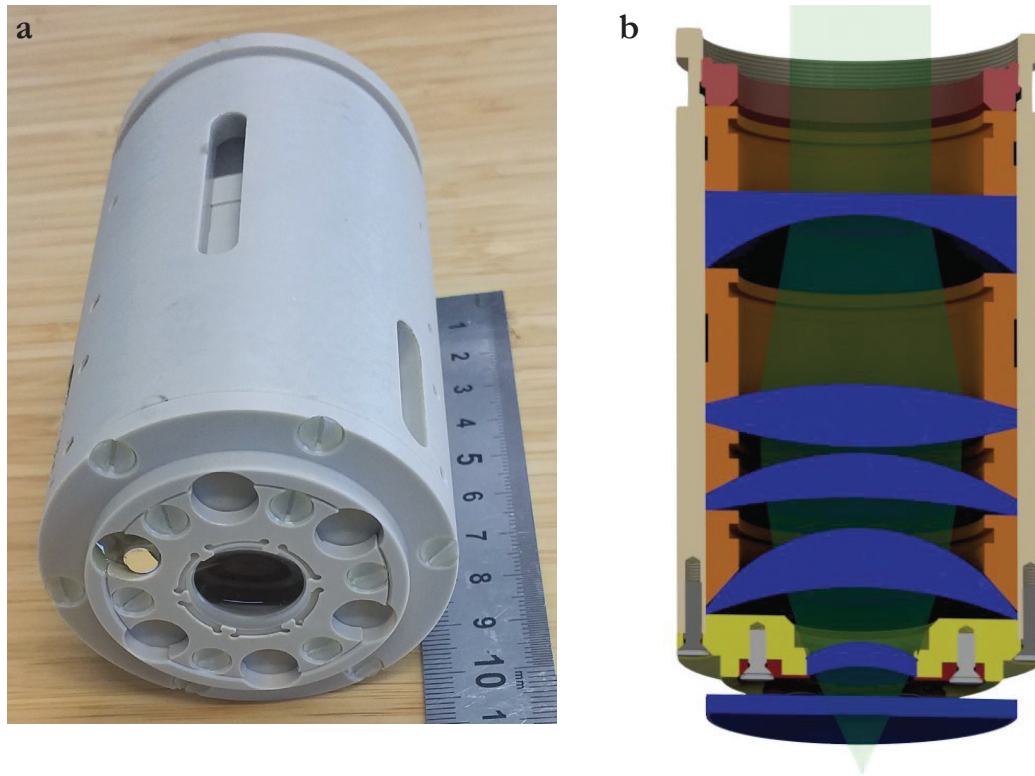


**Figure 5.1: Constructed microscope objective (a) and CAD, shown in a cutaway view (b).**

cal tweezers. Following this direction allows us to characterize the performance of the objective and to train ourselves at the detection of single Sr atoms held in tweezers, which is a stepping stone towards the detection of individual atoms in an optical lattice as usually needed for quantum gas microscopy. The creation of optical tweezers holding single strontium atoms is an ongoing project in our group and in this chapter I will discuss the results accomplished during my time in the lab.

### **Designing and manufacturing the objective**

The first challenge to address on the way to single atoms in tweezers and quantum gas microscopy is to reach high resolution imaging despite the fact that the atoms have to be inside a vacuum chamber, accessible only through a glass window that is typically several millimeters thick. A range of solutions have been developed, such as placing a large-numerical-aperture aspheric lens or microscope objective inside the vacuum system [187, 188], locating the atoms in the vicinity of the glass surface and using solid-immersion microscopy [189, 190] or using specially designed microscope objectives that compensate for the aberrations of the glass window [37]. We chose the latter path and designed our apparatus with two placement options

---

for an objective, the reentrant windows of the main or the science chambers. Placing the objective on the main chamber enables a quick transfer of the atoms into the microscope objective focus, but makes it difficult to use downwards propagating MOT beams. This is not an issue for the low atom numbers required for tweezers, but might be one if higher atom numbers are needed for evaporative cooling to a quantum gas. The second placement possibility does not hinder MOT loading, but requires transfer of the atoms from the main chamber to the science chamber, which will take a few seconds per experimental cycle. Either way, the objective has to operate through a vacuum viewport, which introduces aberrations. Another requirement is a long working distance such that the atoms can be kept a few millimeters away from the glass window, which enables access to the atoms with laser beams from the side. Our objective is designed to compensate for the 3.18 mm thick fused silica viewport of the reentrant window and has a working distance of 18.1 mm.<sup>1</sup> A secondary design goal is to create a relatively cheap objective, which can be easily reproduced and adapted to other experiments in our group. We managed to design our objective using only commercially available lenses.<sup>2</sup>

The objective is assembled with a simple and reliable stacking design (Figure 5.1). The lenses are placed inside a tube and separated by spacer rings. The size of the front lens is smaller compared to the other lenses and it is mounted on a special panel, serving also as a front cap for the assembly. The assembled lenses are fixed by tightening a locking ring, threaded into the housing. The objective is manufactured from polyether ether ketone (PEEK), an engineering plastic that is readily machined and can be processed with the workshop infrastructure available at our faculty.

To address a single site of an optical lattice or to focus light into optical tweezers, the resolution of the objective needs to be on the sub- $\mu\text{m}$  level at the wavelength of interest. For fluorescence detection of individual Sr atoms, the strong  $^1S_0 - ^1P_1$  transition at 461 nm is used. To create the optical tweezers, light at 515 nm or 532 nm is used in the first version of the tweezer setup. The numerical aperture ( $NA$ ) of our objective is 0.44, leading to a resolution

$$R \approx \frac{0.61\lambda}{NA} = 639 \text{ nm},$$

according to the Rayleigh criterion for light with a wavelength  $\lambda = 461 \text{ nm}$ . The

---

<sup>1</sup>Including the longer optical path in the glass window of the viewport the "optical" working distance is 19.6 mm.

<sup>2</sup>The objective is constructed with the four lenses LC1315, KBX-151, LE1418, LE1076 from Thorlabs and the lens LAM-459 from Melles Griot.

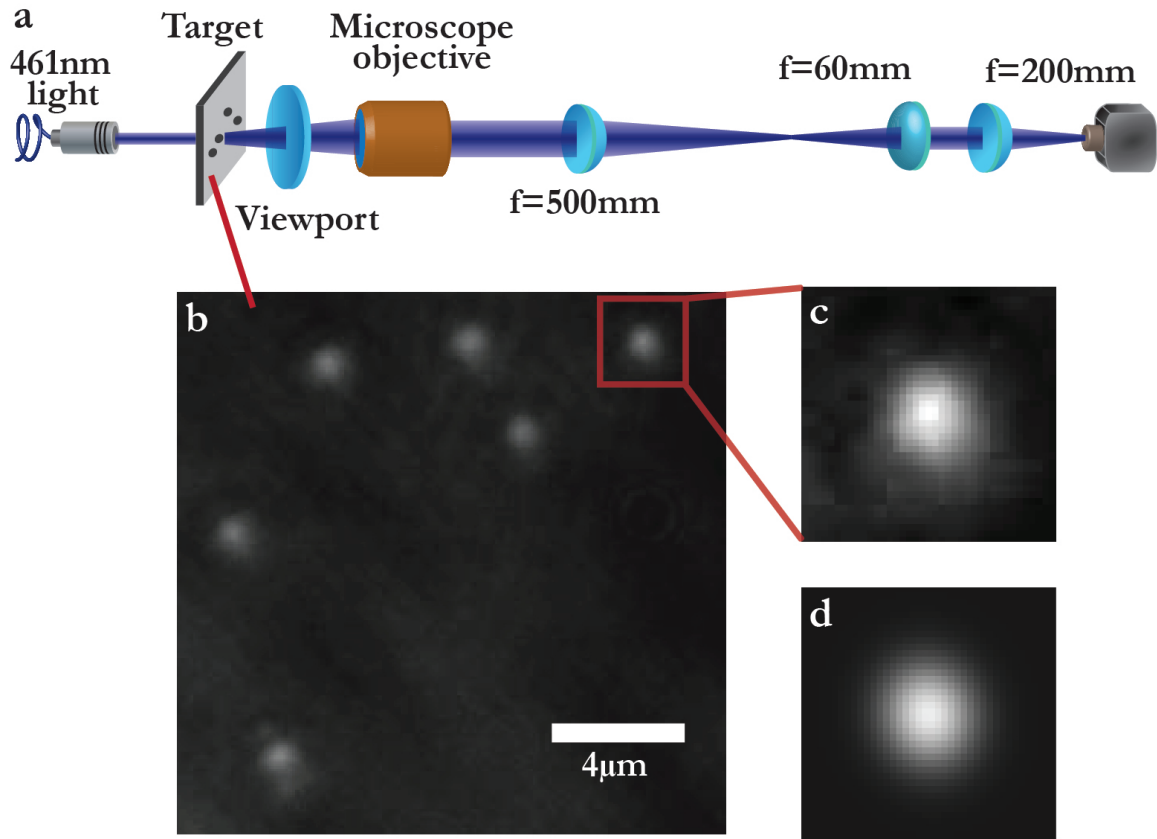


**Figure 5.2: Optical setup to characterize the performance of the objective.** **a**, Simplified layout of the optical setup. **b**, Image of six 200 nm pinholes. **c**, Magnified section of the image, showing one pinhole. **d**, Two-dimensional Gaussian fit to the image **c**. The width determined from the fit ( $\sigma$ ) is  $0.36\mu\text{m}$ . The grayscale used in **c** and **d** is changed with respect to the grayscale used in **b** for better visualization.

short wavelength of the strontium transition is beneficial to achieve a good resolution.

### Characterization of the objective

After assembling the objective we characterize its performance to verify that the required specifications are met. The crucial parameters to characterize are the point spread function (PSF), the field of view, the depth of field and the resolution at the different wavelengths relevant for the experiment. The full characterization of the objective is described in our manuscript [186] and here I will only discuss the procedure to measure the PSF at 461 nm and reference other results [191].

The PSF is measured using the optical setup shown in Figure 5.2 [192]. A set of light sources that are nearly point sources are imaged through the objective, a field

---

lens and a telescope onto a CCD camera. The light source of the setup is a nearly plane wave laser beam with 461 nm wavelength that is sent through sets of pinholes in a Cr-Pt-Pd film on a glass plate that have a diameter of 100 nm or 200 nm.<sup>3</sup> These diameters are significantly smaller than the wavelength such that each pinhole is approximately a point source. The pinholes in each set are distributed in a non-periodic manner to avoid the creation of artifacts. To substitute the viewport of the reentrant window a DN40CF viewport with similar glass thickness is used. The magnification of the optical system is calibrated by calculating the distances between the positions of the pinholes on the CCD image in pixels and comparing that to the distance between the pinholes provided by the manufacturer of the target. To estimate the resolution, the image of each pinhole is fit by the two-dimensional Gaussian [193]

$$n_{\text{Gauss}}(x, y) = A e^{-\frac{(x-x_0)^2}{2\sigma_x^2}} e^{-\frac{(y-y_0)^2}{2\sigma_y^2}} + b,$$

where  $A$  is the peak intensity,  $x_0$  and  $y_0$  are coordinates of the center,  $\sigma_x$  and  $\sigma_y$  are widths of the Gaussian and  $b$  is the background intensity.

Several other important parameters of the objective are determined using a similar setup (Figure 5.2). The depth of field is measured by recording the PSF for different positions of the lens. The measured depth of field meets the design goal of 2.1  $\mu\text{m}$ . The field of view is determined by recording the PSF while translating the target in a plane perpendicular to the optical axis. The measured field of view is about 100  $\mu\text{m}$ , which is smaller than the target value of about 200  $\mu\text{m}$  but still sufficient for our purposes. The resolution is also determined for different wavelengths by changing the light source illuminating the target. The measured resolution gradually worsens for longer wavelengths. The resolution for 461 nm, 532 nm, 635 nm and 671 nm light is measured to be 0.63  $\mu\text{m}$ , 0.75  $\mu\text{m}$ , 1.09  $\mu\text{m}$  and 1.05  $\mu\text{m}$  respectively.

### Preparation for experiments with optical tweezers

Optical tweezers are tightly focused ODTs, which can trap single atoms. In the following paragraphs I describe our first optical system used to produce just a single tweezer, which prepares the ground for future experiments and allows to further characterize our microscope objective.

The trapping potential of an optical tweezer is created by focusing a laser beam that is far-detuned from any strontium transition (see Section 3.4). To prepare laser

---

<sup>3</sup>The target with six sets of pinholes is prepared by ScopeM, ETH Zurich.

beams for tweezers a dedicated optical system is constructed (Figure 5.3). The shown system is a first, simple version, facilitating debugging and helping to establish the focusing procedure of the microscope that will be used once this optical system is installed on the vacuum system. The light source is simply a free running laser diode at 514 nm,<sup>4</sup> assembled analogously to the slave lasers used in our other laser systems (Figure 2.17). Ultimately we could build an ECDL at that wavelength to seed the slave, thereby creating a narrow linewidth beam of sufficient power for our application. However so far we use a free running slave laser with a broad spectrum. The output light of the slave is coupled to a fiber that brings light to the optical breadboard, mounted closely to the objective. An alternative light source is a diode-pumped solid state green laser module at 532 nm,<sup>5</sup> which can be used by swapping the input of the fiber leading to the optical breadboard. From the output collimator the laser beam is guided to an AOM. By driving the AOM with RF signals containing multiple frequencies several laser beams can be generated, allowing the creation of a one-dimensional array of optical tweezers. The outputs of four AOM drivers are combined on a mixer to generate an RF signal with four frequency components. In the next version of the optical system the AOM will be exchanged by a two-axis acousto-optic deflector (AOD),<sup>6</sup> allowing to create a two-dimensional array. To monitor the created pattern, the laser beams can be sent to an auxiliary camera using flip-mirrors. The fluorescence light is collected on an EMCCD camera,<sup>7</sup> which is located on a separate breadboard, positioned below the optical tweezer breadboard.

Overlapping the rMOT with the focal plane of the objective might be complicated when using only tweezers to capture atoms since this ODT has a very small waist and a short Rayleigh length. Therefore we also incorporate the option to produce an ODT with larger waist and longer Rayleigh length by focusing a collimated beam with smaller waist through the objective (Figure 5.3). The focal waist of a collimated beam focused by the lens is

$$w_{\text{foc}} = \frac{\lambda f}{\pi w_{\text{in}}} \frac{1}{\sqrt{1 + \left[ \frac{\lambda f}{\pi w_{\text{in}}^2} \right]^2}},$$

where  $\lambda$  is the wavelength of light,  $f$  is the focal length of the lens and  $w_{\text{in}}$  is the waist of the incoming collimated beam. To overlap the MOT with the tweezer we

---

<sup>4</sup>Nichia, NDG4716E.

<sup>5</sup>Thorlabs, DJ532-40.

<sup>6</sup>AA Opto-Electronic, DTSXY-400-800.

<sup>7</sup>Andor iXon 897.

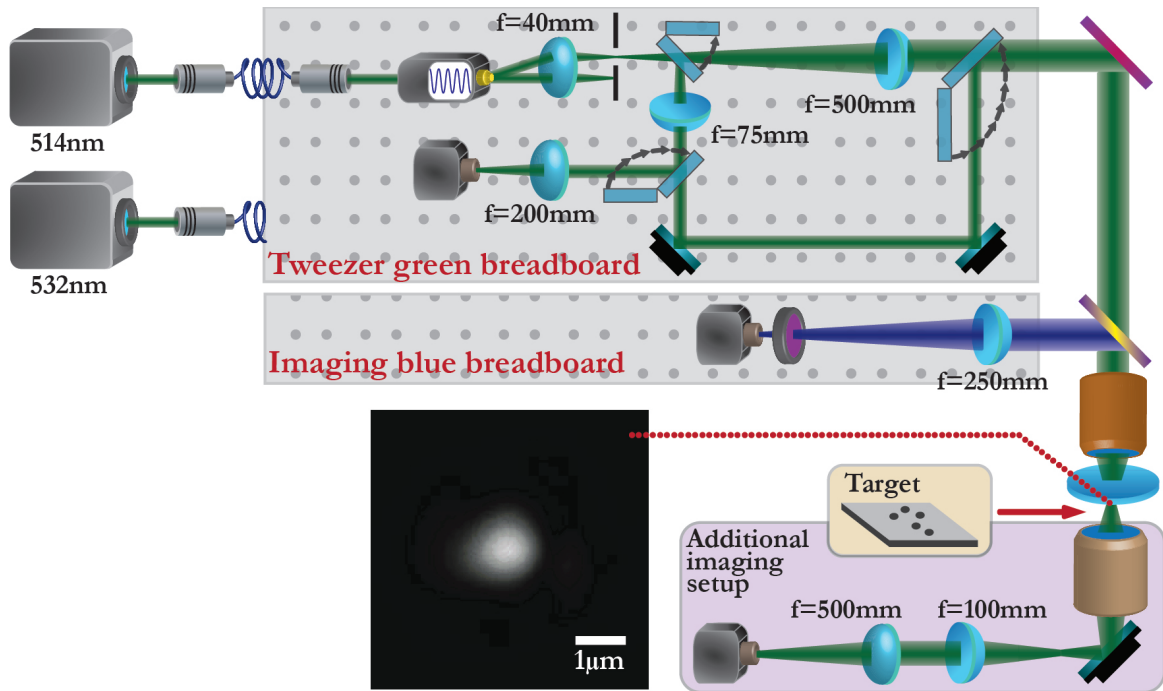


Figure 5.3: Simplified layout of the optical system for optical tweezers, which is characterized using the additional imaging setup calibrated with the target.

initially use the ODT with a large waist. Then we align the imaging system and switch over to the ODT with a small waist, the tweezer.

Before installing the optical system on the apparatus it is characterized on the test setup (Figure 5.3). The test setup imitates the optical system placed on the vacuum system. The objective is attached to a holder with two dichroic mirrors, combining the light at 461 nm used for fluorescence detection, the light at 515 or 532 nm used to create the trapping potential and the red light to address the  $^3P_J$  manifold at 671, 689 and 698 nm. Two optical breadboards for the green and blue light are mounted beside the objective and will eventually be attached to the top breadboard above the vacuum system. An additional imaging system is used to measure the waist of the focused laser beam, which determines the size of the tweezers. The additional imaging system is composed of a commercial microscope objective,<sup>8</sup> the magnifying telescope and the camera. The magnification of the imaging system is again calibrated using the target with small pinholes. We noticed that the smallest waist is achieved when the reflections from the vacuum viewport and from the input lens of the objective are overlapped with the incident laser beam.

After performing tests of the optical system the breadboards are moved to the

<sup>8</sup>Newport, M-40X.

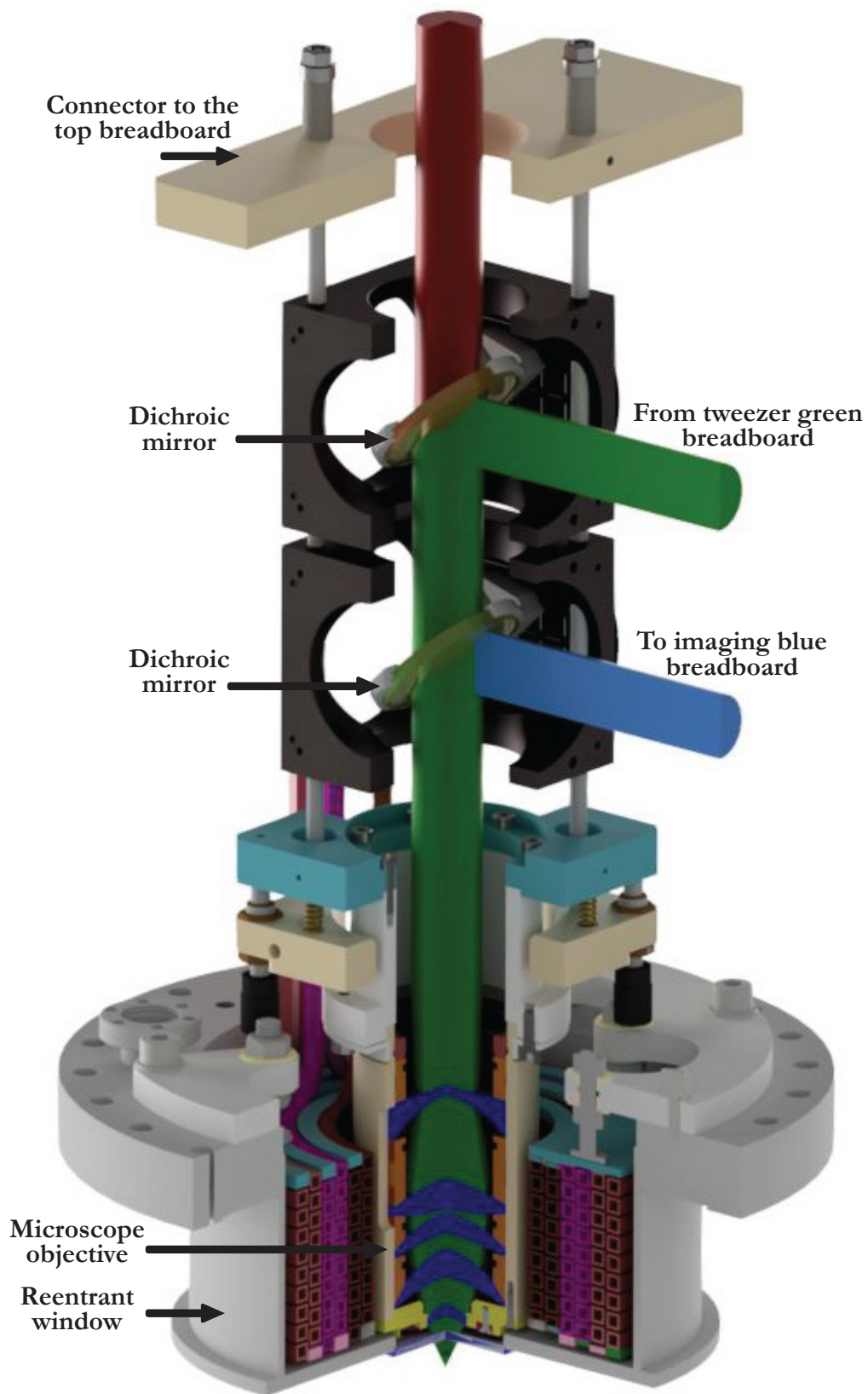


Figure 5.4: Microscope objective on the vacuum system, shown in three quarter cutaway view.

---

vacuum system and the objective is installed above the main chamber (Figure 5.4). This drastically changes the collimation of the downwards propagating MOT beams. For the bMOT we opted to remove both vertical MOT beams since it is difficult to combine the blue fluorescence imaging system with a vertical downwards propagating bMOT beam. The vertical upwards propagating bMOT beam alone would push atoms upwards out of the MOT and therefore it is removed as well. We then discovered that the loading of the  $^3P_2$  reservoir still works decently well with only the four horizontal bMOT beams. For the rMOT the role of the downwards propagating beam is partially taken over by the gravitational force, pulling atoms down to the location of the rMOT (see Section 3.3.2). An advantage when loading an optical tweezer is the significantly less stringent requirement on the number of atoms in the rMOT in comparison with loading crossed ODTs aiming at achieving degenerate quantum gases.

The focus of the microscope objective is located about 10 mm above the center of the main chamber. The atoms are moved from the center of the chamber to the focal plane during the rMOT stage. This is achieved by shifting the MOT quadrupole field center upwards by applying a vertical offset magnetic field with the coil attached to the top flange of the main chamber (see Figure 2.28). To accurately overlap the atomic cloud in all three dimensions with the tweezer focus the final position of the rMOT is adjusted using the low-field coils.

Overlapping the focus of the tweezer beam with the rMOT can be tedious therefore we developed a trick to simplify the task. From the imaging breadboard a laser beam at 461 nm, tuned to resonance, is sent through the objective, leading to weak fluorescence of the atoms entering the main chamber from the Zeeman slower. The divergence angle of the atomic beam is relatively large and the fluorescence signal outlines the pass of the tweezer laser beam in the vacuum chamber, showing the focus position. Then the rMOT can easily be superimposed with that position.

Enriching optical tweezer experiments with the unique properties of strontium atoms opens new perspectives for quantum-enhanced metrology, quantum computation and simulation. The preparation activities described in this chapter are the first steps towards optical tweezers with single strontium atoms undertaken with our experiment.

# Chapter 6

## Outlook

The thesis describes the construction of a new-generation ultracold Sr apparatus and two important technological developments. The primary goal of the endeavors is to create a new platform based on ultracold strontium to explore the field of quantum simulations. The accomplished work creates a foundation for those experiments and opens directions for future research to further push the technological envelop and reach the ambitious goal of quantum simulations with Sr. I briefly describe possible future activities along objectives that are appealing to us.

The first objective we are interested in is the study of quantum Hall physics and a promising technique for its realization is the use of optical flux lattices [23, 24, 44]. The plan for this objective is to work with fermionic strontium, exploiting ultranarrow transitions and the rich energy level structures provided by the large nuclear spin. The necessary coupling between different substates can be generated by two-photon Raman transitions created with the developed  $^1S_0 - ^3P_2$  laser system. Using the transition with narrow linewidth mitigates the problem of off-resonant scattering, improving the lifetime of the atomic sample under Raman coupling to the level of seconds. The linewidth of the prepared laser can be additionally narrowed by locking the laser to the high finesse cavity specially purchased for that purpose. To isolate atoms in a two-dimensional pancake an optical lattice can be added to the optical setup. Our IR laser system is already set up to provide enough optical paths and output power.

The second appealing objective relates to synthetic gauge fields with a primary focus on generating gauge fields using a finite lattice in a synthetic dimension in addition to a lattice in real space [45–47]. The periodic structure in real space can be engineered with optical lattices by extending the already prepared optical paths of the IR laser system. The idea for the synthetic dimension is to exploit the large

---

nuclear spin of the fermionic isotope, leading to a lattice dimension as large as ten. Similarly to the previous objective, two-photon Raman transitions can be used to couple different substates, which represents hopping along the synthetic dimension. To lift the degeneracy of the substates we can use a bias magnetic field of a few hundred Gauss, which can be easily achieved with our magnetic field coils. This field also strongly splits the  $^3P_2$  hyperfine states, such that nuclear spin state specific Raman coupling becomes possible using the  $^3P_2$  states as excited states. To accurately detect the population of different substates we can use a spin-selective imaging system, which is based on the optical Stern-Gerlach technique [95].

The third direction of our research is quantum gas microscopy, relying on using a newly constructed microscope objective [36–39]. The great inspiration to push particularly this direction comes from the recent achievements with strontium in optical tweezers. The researchers demonstrated a large two-dimensional array of optical tweezers with up to 121 sites [30–32]. Despite the lack of hyperfine structure in bosonic Sr, Sisyphus cooling was shown to be an effective technique in compensating heating while detecting individual atoms by fluorescence imaging. At the same time with the discovery of Sisyphus cooling in tweezers our group showed Sisyphus slowing and cooling of an atomic beam of Sr [194]. In addition to Sisyphus cooling, sideband cooling of Sr was realized in tweezers using magic wavelength conditions to obtain the same Stark shift in the  $^1S_0$  and  $^3P_1$  states. Sideband cooling enables to cool atoms to almost the motional ground state of the trapping potential. In order to detect single atoms, fluorescence imaging is the broadly used approach with its superior sensitivity compared to absorption imaging. For Sr efficient fluorescence is obtained by excitation on the broad, blue transition at 461 nm. However, an unwanted side effect is heating of the trapped atoms, which can gain sufficient energy to leave the tweezer potential. To counteract the heating, one of the two cooling methods mentioned above is implemented using the narrow, red transition at 689 nm. By using cooling simultaneously with imaging, fluorescence can be maintained long enough to determine the presence of an atom in a tweezer, providing high fidelity detection. This detection technique allows to take thousands of images of a single atom [134], which is useful for sorting atoms into a desired pattern [18, 19] or for using the same atomic sample multiple times [41, 42]. These pioneering works established a new platform for precision measurement and quantum simulation and computation.

Our original plan was to pursue the direction of quantum gas microscopy and the newly constructed apparatus was designed to work with degenerate quantum

gases. However the great potential for Sr tweezers and the capability to easily adapt our system to new research lines pushed us to deviate from the initial plan of developing a Sr quantum gas microscope and instead first implement tweezers.

# Chapter 7

## Summary

Quantum simulation is one of the fast growing fields of modern science, aiming at solving difficult problems in quantum physics and bringing our understanding of it to new levels. A powerful platform for quantum simulation are ultracold quantum gases, which allow to mimic exotic quantum states of solid state materials and provide us with the unique possibility to control quantum systems down to the level of a single atom. This control starts with the detailed initialization of the quantum system in all degrees of freedom of the atoms, includes the spatio-temporal control of external potentials, atomic states and interactions, and finishes in an accurate observation of relevant aspects of the final state. Experiments with ultracold alkaline-earth elements open promising avenues to address important quantum simulation challenges, such as the creation of long-lived systems with artificial gauge fields and synthetic dimensions, the study of  $SU(N)$  magnetism, or the study of many-body physics influencing the precision and accuracy of optical clocks.

This thesis describes the process of building a new ultracold strontium apparatus and developing new techniques paving the way to future research. The building process starts from empty optical tables and gradually moves through stages of designing, assembling and characterizing the new apparatus. These stages comprise constructing the vacuum system and attaining ultra-high vacuum, building the laser systems and implementing methods and techniques to bring the thermal atoms to quantum degeneracy. These methods include transverse cooling, Zeeman slowing, magneto-optical trapping on the broad and narrow transitions, dipole trapping and evaporative cooling to Bose-Einstein condensation and Fermi degeneracy. The prepared degenerate quantum gases are a foundation for future research, aiming at exploiting the unique properties of strontium for quantum simulations. To implement the quantum simulations of interest to us several additional exper-

imental techniques are required and within this thesis two of these developments have been accomplished. The first one is measuring the frequency of the ultranarrow  $^1S_0 - ^3P_2$  transition in fermionic strontium. This transition should allow nuclear spin-state specific Raman coupling or light shifting without much off-resonant scattering of photons, which is useful to implement artificial gauge fields or synthetic dimensions while keeping the system long-lived. The second development is the construction of a microscope objective for a high-resolution imaging system that allows the manipulation and detection of single atoms trapped in an optical lattice or in optical tweezers.

An important objective for the design of our new apparatus was flexibility, which is a valuable capability allowing to pursue various goals. We envision to use the apparatus for a broad range of goals, for instance studying quantum gases in a bulk or lattice environment, realizing optical flux lattice to mimic effects of a strong magnetic field on charged particles, implementing techniques to detect and manipulate individual atoms trapped in optical tweezers and more. The apparatus allows to easily accommodate new technological developments or to implement novel theoretical proposals and therefore the research direction can easily turn to a new appealing opportunity. The progress achieved during this thesis paves new ways towards quantum simulation with ultracold strontium.

# Samenvatting

Quantumsimulatie is een snel groeiend onderwerp binnen de moderne wetenschap. Het heeft tot doel om lastige vraagstukken in de quantumfysica op te lossen en ons begrip ervan tot grotere hoogten op te stuwten. Een krachtig platform voor quantumsimulatie wordt geboden door ultrakoude gassen die het mogelijk maken om bijvoorbeeld exotische quantumtoestanden van vaste-stof materialen na te bootsen. Deze quantumgassen bieden de unieke mogelijkheid om quantumsystemen te beheersen tot op het niveau van afzonderlijke atomen. De beheersing en manipulatie van zo'n quantumstelsel begint met het initialiseren van alle vrijheidsgraden van de atomen. Vervolgens moeten alle externe potentialen, atomaire toestanden en interacties in ruimte en tijd worden gecontroleerd. Tenslotte worden relevante eigenschappen van de eindtoestand gemeten. Experimenten met ultrakoude aardalkali-atomen openen veelbelovende routes om belangrijke quantumsimulatie-uitdagingen aan te pakken, zoals het creëren van langlevende systemen met kunstmatige ijkvelden en synthetische dimensies, het bestuderen van  $SU(N)$  magnetisme of de studie van veel-deeltjesfysica die de nauwkeurigheid van optische klokken beïnvloedt.

Dit proefschrift beschrijft de opbouw van een nieuwe opstelling voor ultrakoud strontium, en de ontwikkeling van nieuwe technieken die de weg bereiden voor toekomstig onderzoek. Beginnend vanaf lege optische tafels gaat het opbouwproces via verschillende fasen van ontwerp en assemblage tot het karakteriseren van de nieuwe opstelling. Deze fasen bestaan uit de constructie van het vacuumsysteem en het bereiken van ultrahoogvacuum, de opbouw van de lasersystemen, en het implementeren van methoden en technieken om de thermische atomen tot quantumontaarding te brengen. Deze methoden omvatten transversale koeling, Zeeman afremming, magneto-optische invang gebruikmakend van zowel brede als nauwe overgangen, dipoolvallen en verdampingskoelen tot Bose-Einstein condensatie en Fermi ontaarding. De aldus geprepareerde ontaarde quantumgassen vormen het vertrekpunt voor verder toekomstig onderzoek, dat profiteert van de

unieke geschiktheid van strontium voor quantumsimulaties.

Om de beoogde quantumsimulaties te kunnen implementeren, zijn nog verschillende aanvullende experimentele technieken nodig. Binnen het kader van dit proefschrift zijn twee van deze ontwikkelingen gelukt. De eerste is het meten van de frequentie van de ultrasnelle  $1S_0$ - $3P_2$  overgang in fermionisch strontium. Deze overgang moet Raman koppelingen mogelijk maken tussen specifieke kernspintoe-standen. Tevens wordt het hiermee mogelijk om energieniveaus te verschuiven met behulp van licht, zonder al te veel verstorende off-resonante verstrooiing van fotonen. Dit laatste is nuttig om kunstmatige ijkvelden te implementeren, of synthetische dimensies in een langlevend systeem. De tweede ontwikkeling is de constructie van een microscoopobjectief voor hoge-resolutie afbeeldingen die het manipuleren en detecteren van afzonderlijke atomen mogelijk maakt, terwijl ze worden vastgehouden in een optisch rooster of in optische pincetten.

Een belangrijk doel bij het ontwerp van de nieuwe opstelling was flexibiliteit, teneinde de mogelijkheid open te laten om een scala van verschillende doelen na te kunnen streven. Het doel is dan ook om de opstelling voor een scala aan experimenten te gebruiken. Dit omvat onder meer de studie van quantumgassen in bulk of in een roosteromgeving, de realisatie van een optisch fluxrooster om de effecten van een sterk magneetveld op geladen deeltjes na te bootsen, het implementeren van technieken voor het manipuleren en detecteren van individuele atomen in optische pincetten. Met een flexibele opstelling kunnen eenvoudig nieuwe technologische ontwikkelingen worden geaccomodeerd, en kunnen nieuwe theoretische voorstellen worden geïmplementeerd. Zo kan het onderzoek eenvoudig inspelen op nieuwe kansen als die zich voordoen. De voortgang die in dit proefschrift is bereikt, opent zo nieuwe wegen voor quantumsimulatie met ultrakoud strontium.

# List of publications

## **Published article:**

Oleksiy Onishchenko, Sergey Pyatchenkov, Alexander Urech, Chun-Chia Chen, Shayne Bennetts, Georgios A. Siviloglou, and Florian Schreck, "Frequency of the ultranarrow  $^1S_0 - ^3P_2$  transition in  $^{87}\text{Sr}$ ", [Phys. Rev. A \*\*99\*\*, 052503 \(2019\)](#).

*Contribution:* major contribution to designing, assembling and characterizing the new ultracold strontium apparatus used to perform the experiment; contribution to planning and carrying out the experiment; evaluating and analyzing the obtained data; discussing the results and commenting on the manuscript.

## **Submitted for publication:**

Ivo Knottnerus, Sergey Pyatchenkov, Oleksiy Onishchenko, Alexander Urech, Georgios A. Siviloglou, Florian Schreck, "Microscope objective for imaging atomic strontium with 0.63 micrometer resolution", [arXiv:1906.07167 \(2019\)](#).

*Contribution:* contribution to devising the microscopy part of our apparatus and the characterization scheme for the objective; testing the constructed microscope objective and updating the existing experimental apparatus; carrying out the primary experiments aimed at quantum gas microscopy.

# Acknowledgments

Constructing a new apparatus from empty optical tables to a level of conducting first experiments is a challenging task requiring substantial efforts and time. Working on setting up the new experiment helped me to deepen my knowledge and master my skills along with bringing the memorable moments of joy and happiness for the attained achievements and successes. I would like to thank my supervisor, colleagues, friends and family for their help and support during these years.

Florian Schreck, thank you very much for providing me the opportunity to work on the engaging experiment with a team of great researchers. All experiments performed in your group are the outstanding combinations of fundamental physics and sophisticated engineering, pushing the frontiers of science and technology. Your extensive knowledge and infinite expertise about any detail in the lab always helped us to materialize challenging ideas and to successfully overcome the confronted obstacles. Your passion for physics and dedication to the experimental work always inspire me and give a perfect example of the professional and competent researcher. Your vision for the research directions and intuition for the exciting open questions in the field of quantum gases guided the experiment to pursue the most important unsolved problems accessible with our new apparatus. I especially grateful for your patience and countless advices during the writing of this manuscript.

The SrMic team, thank you for all the efforts, time and energy which we put into a complicated and involving process of setting up the new experiment. Georgios Siviloglou, your professional attitude and ability to address versatile issues guided the team to construct a state-of-the-art apparatus. You were always calmly pushing the project forward and efficiently managing the team. I admire your ability to find the way to achieve the desired results even with limited resources. I learned a lot from our fruitful discussions while designing, constructing and operating the machine. Robert Spreuw, thank you for the engaging discussions and useful advices. You always carefully organize and analyze the data so the team can understand the status of the experiment clearly and develop the required improvements. Oleksiy

---

Onishchenko and Alex Urech, thank you guys for all the working days and weekends in the lab. Alex, people around you can always count on your infinite enthusiasm and energy in any time of a day, regardless of the experiencing difficulties. I will always remember your bursts of energy and little dances after our achievements and successes, even after the small ones. I wish you luck to successfully overcome the impending challenges and to bring the experiment to the new level, providing the desired results. Ivo Knottnerus, you nicely fit into a group and your talents and engineering skills productively enriched the team. The infrastructure constructed by you helped to establish a new research direction and to faster move forward to the pursued goals. Thies Plassmann, I wish you luck in your endeavors on assembling a new equipment for the experiment.

I was lucky to share the laboratory room with the SrPAL team, a group of extraordinary physicists and skillful engineers. You are the most hardworking and dedicated people I have met. I am grateful for the friendly and collaborative atmosphere you created in the lab during these years. Thank you for all productive conversations during days and nights, working days and weekends. Shayne Bennetts, your insane work ethic and incredible range of skills set an outstanding example for others to look up. I always admire your dedication to carefully measure, characterize and understand every aspect of the situation to make a professional conclusion. Somehow you know and deeply understand everything about literally any challenge in a lab and humbly share your great knowledge and expertise with others. Chun-Chia Chen, I always appreciate your ability to stay calm and motivated to find a way to continue perusing the outlined goals against all odds. Benjamin Pasquiou, your extremely valuable power of solving problems and wise advices helped many times to overcome difficult situations and achieve the desired results. I highly appreciate your efforts and time to methodically improve the lab environment for all members of the group. Rodrigo Gonzalez Escudero, your optimism brings cheerfulness to any occasion and you are genuinely a nice colleague who always offers help.

It has been a great pleasure to work at the Strontium quantum gas group with talented researchers from the RbSr team, Vincent Barbe, Lukas Reichsollner, Alessio Ciamei, Premjith Thekkeppat, Alex Bayerle, Severin Charpignon, newly established iqClock team, Francesca Fama and Sheng Zhou, and great theorists Denis Kurlov and Jiri Minar. Thank you for the constructive advices and creating collaborative environment in the group.

I thank members of other quantum gases groups at the University of Amsterdam, Henning Furst, Thomas Feldker, Norman Ewald, David Davtyan, Carla Sanna,

Maarten Soudijn, Arthur La Rooij. Thank you for sharing your experience and expertise, for broadening my scientific views and enriching my knowledge about various aspects of physics.

I want to acknowledge Technological Center at the University of Amsterdam for the help and support in constructing a complicated research apparatus. I am especially grateful to Hans Ellermeijer, whose professionalism and technical expertise played a significant role in constructing and establishing a properly working experiment.

A great help in solving administrative issues and the assistance on various administrative occasions came from Joost van Mameren, Anne-Marieke Crommentuijn, Astrid Harryson, Klaartje Wartenbergh. I want to especially thank Jirina Salkova for your help during the last phase of my PhD.

I would like to thank my parents, Valentina and Vasiliy Piatchenkov, for your endless support, encouragement and faithful believe in me and my decisions.

# Bibliography

- [1] S. Stellmer, M. K. Tey, B. Huang, R. Grimm, and F. Schreck, “Bose-Einstein condensation of strontium”, *Phys. Rev. Lett.* **103**, 200401 (2009).
- [2] Y. N. M. de Escobar, P. G. Mickelson, M. Yan, B. J. DeSalvo, S. B. Nagel, and T. C. Killian, “Bose-Einstein condensation of  $^{84}\text{Sr}$ ”, *Phys. Rev. Lett.* **103**, 200402 (2009).
- [3] B. J. DeSalvo, M. Yan, P. G. Mickelson, Y. N. Martinez de Escobar, and T. C. Killian, “Degenerate Fermi gas of  $^{87}\text{Sr}$ ”, *Phys. Rev. Lett.* **105**, 030402 (2010).
- [4] M. K. Tey, S. Stellmer, R. Grimm, and F. Schreck, “Double-degenerate Bose-Fermi mixture of strontium”, *Phys. Rev. A* **82**, 011608 (2010).
- [5] S. Stellmer, F. Schreck, and T. C. Killian, “Degenerate quantum gases of strontium”, *Annual Review of Cold Atoms and Molecules*, **1** (2014).
- [6] X. Xu, T. H. Loftus, J. L. Hall, A. Gallagher, and J. Ye, “Cooling and trapping of atomic strontium”, *J. Opt. Soc. Am. B* **20**, 968 (2003).
- [7] T. H. Loftus, T. Ido, M. M. Boyd, A. D. Ludlow, and J. Ye, “Narrow line cooling and momentum-space crystals”, *Phys. Rev. A* **70**, 063413 (2004).
- [8] C. He, E. Hājīyev, Z. Ren, B. Song, and G.-B. Jo, “Recent progresses of ultracold two-electron atoms”, *J. Phys. B* **52**, 102001 (2019).
- [9] C. Gross and I. Bloch, “Quantum simulations with ultracold atoms in optical lattices”, *Science* **357**, 995 (2017).
- [10] I. Bloch, J. Dalibard, and S. Nascimbène, “Quantum simulations with ultracold quantum gases”, *Nature Physics* **8**, 267 (2012).
- [11] W. Hofstetter and T. Qin, “Quantum simulation of strongly correlated condensed matter systems”, *J. Phys. B* **51**, 082001 (2018).
- [12] I. Bloch, J. Dalibard, and W. Zwerger, “Many-body physics with ultracold gases”, *Rev. Mod. Phys.* **80**, 885 (2008).

- [13] C. Chin, R. Grimm, P. Julienne, and E. Tiesinga, “Feshbach resonances in ultracold gases”, *Rev. Mod. Phys.* **82**, 1225 (2010).
- [14] J. Lim, H.-g. Lee, and J. Ahn, “Review of cold Rydberg atoms and their applications”, *J. Korean Phys. Soc.* **63**, 867 (2013).
- [15] C. Menotti, M. Lewenstein, T. Lahaye, and T. Pfau, “Dipolar interaction in ultracold atomic gases”, *AIP Conf. Proc.* **970**, 332 (2008).
- [16] M. Aidelsburger, S. Nascimbene, and N. Goldman, “Artificial gauge fields in materials and engineered systems”, *Comptes Rendus Physique* **19**, 394 (2018).
- [17] J. Dalibard, F. Gerbier, and P. Öhberg, “Colloquium: artificial gauge potentials for neutral atoms”, *Rev. Mod. Phys.* **83**, 1523 (2011).
- [18] D. Barredo, V. Lienhard, S. de Léséleuc, T. Lahaye, and A. Browaeys, “Synthetic three-dimensional atomic structures assembled atom by atom”, *Nature* **561**, 79 (2018).
- [19] M. Endres, H. Bernien, A. Keesling, H. Levine, E. R. Anschuetz, A. Krajenbrink, C. Senko, V. Vuletic, M. Greiner, and M. D. Lukin, “Atom-by-atom assembly of defect-free one-dimensional cold atom arrays”, *Science* **354**, 1024 (2016).
- [20] A. V. Gorshkov, M. Hermele, V. Gurarie, C. Xu, P. S. Julienne, J. Ye, P. Zoller, E. Demler, M. D. Lukin, and A. M. Rey, “Two-orbital SU(N) magnetism with ultracold alkaline-earth atoms”, *Nature Physics* **6**, 289 (2010).
- [21] M. A. Cazalilla and A. M. Rey, “Ultracold Fermi gases with emergent SU(N) symmetry”, *Rep. Prog. Phys.* **77**, 124401 (2014).
- [22] M. Nakagawa, N. Kawakami, and M. Ueda, “Non-Hermitian Kondo effect in ultracold alkaline-earth atoms”, *Phys. Rev. Lett.* **121**, 203001 (2018).
- [23] N. R. Cooper, “Optical flux lattices for ultracold atomic gases”, *Phys. Rev. Lett.* **106**, 175301 (2011).
- [24] N. R. Cooper and J. Dalibard, “Reaching fractional quantum Hall states with optical flux lattices”, *Phys. Rev. Lett.* **110**, 185301 (2013).
- [25] A. J. Daley, M. M. Boyd, J. Ye, and P. Zoller, “Quantum computing with alkaline-earth-metal atoms”, *Phys. Rev. Lett.* **101**, 170504 (2008).
- [26] A. J. Daley, “Quantum computing and quantum simulation with group-II atoms”, *Quantum Inf. Process.* **10**, 865 (2011).

- [27] G. Pagano, F. Scazza, and M. Foss-Feig, “Fast and scalable quantum information processing with two-electron atoms in optical tweezer arrays”, *Adv. Quantum Technol.* **2**, 1800067 (2019).
- [28] S. Bennetts, C.-C. Chen, B. Pasquiou, and F. Schreck, “Steady-state magneto-optical trap with 100-fold improved phase-space density”, *Phys. Rev. Lett.* **119**, 223202 (2017).
- [29] iqClock, *Integrated quantum clock*, (iqclock.eu) <https://www.iqclock.eu/> (visited on 01/10/2019).
- [30] A. Cooper, J. P. Covey, I. S. Madjarov, S. G. Porsev, M. S. Safronova, and M. Endres, “Alkaline-earth atoms in optical tweezers”, *Phys. Rev. X* **8**, 041055 (2018).
- [31] M. A. Norcia, A. W. Young, and A. M. Kaufman, “Microscopic control and detection of ultracold strontium in optical-tweezer arrays”, *Phys. Rev. X* **8**, 041054 (2018).
- [32] N. C. Jackson, R. K. Hanley, M. Hill, C. S. Adams, and M. P. A. Jones, "Number-resolved imaging of  $^{88}\text{Sr}$  atoms in a long working distance optical tweezer", arXiv: 1904.03233 (2019).
- [33] S. Campbell, "A Fermi-degenerate three-dimensional optical lattice clock", University of Colorado (2017).
- [34] Ultracold Strontium Lab, MPQ, (ultracold.sr) <http://ultracold.sr/> (visited on 01/10/2019).
- [35] Ultracold Strontium Lab, UC San Diego, (barreiolab.com) <https://barreiolab.com/> (visited on 01/10/2019).
- [36] W. S. Bakr, J. I. Gillen, A. Peng, S. Fölling, and M. Greiner, “A quantum gas microscope for detecting single atoms in a Hubbard-regime optical lattice”, *Nature* **462**, 74 (2009).
- [37] J. F. Sherson, C. Weitenberg, M. Endres, M. Cheneau, I. Bloch, and S. Kuhr, “Single-atom-resolved fluorescence imaging of an atomic Mott insulator”, *Nature* **467**, 68 (2010).
- [38] S. Kuhr, “Quantum-gas microscopes: a new tool for cold-atom quantum simulators”, *Natl. Sci. Rev.* **3**, 170 (2016).
- [39] H. Ott, “Single atom detection in ultracold quantum gases: a review of current progress”, *Rep. Prog. Phys.* **79**, 054401 (2016).

- [40] S. Saskin, J. T. Wilson, B. Grinkemeyer, and J. D. Thompson, “Narrow-line cooling and imaging of ytterbium atoms in an optical tweezer array”, [Phys. Rev. Lett. 122, 143002 \(2019\)](#).
- [41] I. S. Madjarov, A. Cooper, A. L. Shaw, J. P. Covey, V. Schkolnik, T. H. Yoon, J. R. Williams, and M. Endres, "An atomic array optical clock with single-atom readout", arXiv: 1908.05619 (2019).
- [42] M. A. Norcia, A. W. Young, W. J. Eckner, E. Oelker, J. Ye, and A. M. Kaufman, "Seconds-scale coherence in a tweezer-array optical clock", arXiv: 1904.10934 (2019).
- [43] V. Galitski, G. Juzeliūnas, and I. B. Spielman, "Artificial gauge fields with ultracold atoms", arXiv: 1904.03233 (2019).
- [44] N. R. Cooper and J. Dalibard, “Optical flux lattices for two-photon dressed states”, [EPL 95, 66004 \(2011\)](#).
- [45] M. Mancini, G. Pagano, G. Cappellini, L. Livi, M. Rider, J. Catani, C. Sias, P. Zoller, M. Inguscio, M. Dalmonte, and L. Fallani, “Observation of chiral edge states with neutral fermions in synthetic Hall ribbons”, [Science 349, 1510 \(2015\)](#).
- [46] A. Celi, P. Massignan, J. Ruseckas, N. Goldman, I. B. Spielman, and M. Lewenstein, “Synthetic gauge fields in synthetic dimensions”, [Phys. Rev. Lett. 112, 043001 \(2014\)](#).
- [47] B. K. Stuhl, H.-I. Lu, L. M. Ayccock, D. Genkina, and I. B. Spielman, “Visualizing edge states with an atomic Bose gas in the quantum Hall regime”, [Science 349, 1514 \(2015\)](#).
- [48] H. M. Price, O. Zilberberg, T. Ozawa, I. Carusotto, and N. Goldman, “Four-dimensional quantum Hall effect with ultracold atoms”, [Phys. Rev. Lett. 115, 195303 \(2015\)](#).
- [49] M. Lohse, C. Schweizer, H. M. Price, O. Zilberberg, and I. Bloch, “Exploring 4D quantum Hall physics with a 2D topological charge pump”, [Nature 553, 55 EP \(2018\)](#).
- [50] C. S Adams, J. D Pritchard, and J. P Shaffer, "Rydberg atom quantum technologies", arXiv:1907.09231 (2019).
- [51] M. Saffman, T. G. Walker, and K. Mølmer, “Quantum information with Rydberg atoms”, [Rev. Mod. Phys. 82, 2313 \(2010\)](#).

- 
- [52] E. Guardado-Sanchez, P. T. Brown, D. Mitra, T. Devakul, D. A. Huse, P. Schauß, and W. S. Bakr, “Probing the quench dynamics of antiferromagnetic correlations in a 2D quantum Ising spin system”, [Phys. Rev. X \*\*8\*\*, 021069 \(2018\)](#).
- [53] M. Saffman and T. G. Walker, “Creating single-atom and single-photon sources from entangled atomic ensembles”, [Phys. Rev. A \*\*66\*\*, 065403 \(2002\)](#).
- [54] D. Maxwell, D. J. Szwer, D. Paredes-Barato, H. Busche, J. D. Pritchard, A. Gauguet, K. J. Weatherill, M. P. A. Jones, and C. S. Adams, “Storage and control of optical photons using Rydberg polaritons”, [Phys. Rev. Lett. \*\*110\*\*, 103001 \(2013\)](#).
- [55] F. Nogrette, H. Labuhn, S. Ravets, D. Barredo, L. Béguin, A. Vernier, T. Lahaye, and A. Browaeys, “Single-atom trapping in holographic 2D arrays of microtraps with arbitrary geometries”, [Phys. Rev. X \*\*4\*\*, 021034 \(2014\)](#).
- [56] H. Bernien, S. Schwartz, A. Keesling, H. Levine, A. Omran, H. Pichler, S. Choi, A. S. Zibrov, M. Endres, M. Greiner, V. Vuletic, and M. D. Lukin, “Probing many-body dynamics on a 51-atom quantum simulator”, [Nature \*\*551\*\*, 579 EP \(2017\)](#).
- [57] D. Barredo, S. de Léséleuc, V. Lienhard, T. Lahaye, and A. Browaeys, “An atom-by-atom assembler of defect-free arbitrary two-dimensional atomic arrays”, [Science \*\*354\*\*, 1021 \(2016\)](#).
- [58] L. R. Liu, J. D. Hood, Y. Yu, J. T. Zhang, N. R. Hutzler, T. Rosenband, and K.-K. Ni, “Building one molecule from a reservoir of two atoms”, [Science \*\*360\*\*, 900 \(2018\)](#).
- [59] V. Lienhard, S. de Léséleuc, D. Barredo, T. Lahaye, A. Browaeys, M. Schuler, L.-P. Henry, and A. M. Läuchli, “Observing the space- and time-dependent growth of correlations in dynamically tuned synthetic Ising models with antiferromagnetic interactions”, [Phys. Rev. X \*\*8\*\*, 021070 \(2018\)](#).
- [60] S. de Léséleuc, V. Lienhard, P. Scholl, D. Barredo, S. Weber, N. Lang, H. P. Büchler, T. Lahaye, and A. Browaeys, “Observation of a symmetry-protected topological phase of interacting bosons with Rydberg atoms”, [Science \*\*365\*\*, 775 \(2019\)](#).
- [61] S. Weber, S. de Léséleuc, V. Lienhard, D. Barredo, T. Lahaye, A. Browaeys, and H. P. Büchler, “Topologically protected edge states in small Rydberg systems”, [Quantum Sci. Technol. \*\*3\*\*, 044001 \(2018\)](#).

- [62] H. Levine, A. Keesling, A. Omran, H. Bernien, S. Schwartz, A. S. Zibrov, M. Endres, M. Greiner, and M. D. Lukin, “High-fidelity control and entanglement of Rydberg-atom qubits”, *Phys. Rev. Lett.* **121**, 123603 (2018).
- [63] C. J. Picken, R. Legaie, K. McDonnell, and J. D. Pritchard, “Entanglement of neutral-atom qubits with long ground-Rydberg coherence times”, *Quantum Sci. Technol.* **4**, 015011 (2018).
- [64] A. V. Taichenachev, V. I. Yudin, C. W. Oates, C. W. Hoyt, Z. W. Barber, and L. Hollberg, “Magnetic field-induced spectroscopy of forbidden optical transitions with application to lattice-based optical atomic clocks”, *Phys. Rev. Lett.* **96**, 083001 (2006).
- [65] N. Poli, M. G. Tarallo, M. Schioppo, C. W. Oates, and G. M. Tino, “A simplified optical lattice clock”, *Appl. Phys. B* **97**, 27 (2009).
- [66] M. Asano and K. Kubo, “Vapor pressure of strontium below 660K”, *Nucl. Sci. Tech.* **15**, 765 (1978).
- [67] C. B. Alcock, V. P. Itkin, and M. K. Horrigan, “Vapour pressure equations for the metallic elements: 298-2500K”, *Can. Metall. Q.* **23**, 309 (1984).
- [68] G. D. Maria and V. Piacente, “Vapor pressures of calcium and strontium by transpiration method”, *J. Chem. Thermodyn.* **6**, 1 (1974).
- [69] I. Courtillot, A. Quessada, R. P. Kovacich, J.-J. Zondy, A. Landragin, A. Clairon, and P. Lemonde, “Efficient cooling and trapping of strontium atoms”, *Opt. Lett.* **28**, 468 (2003).
- [70] S. Stellmer, "Degenerate quantum gases of strontium", University of Innsbruck (2013).
- [71] R. Senaratne, S. V. Rajagopal, Z. A. Geiger, K. M. Fujiwara, V. Lebedev, and D. M. Weld, “Effusive atomic oven nozzle design using an aligned microcapillary array”, *Rev. Sci. Instrum* **86**, 023105 (2015).
- [72] M. Schioppo, N. Poli, M. Prevedelli, S. Falke, C. Lisdat, U. Sterr, and G. M. Tino, “A compact and efficient strontium oven for laser-cooling experiments”, *Rev. Sci. Instrum.* **83**, 103101 (2012).
- [73] K. Jousten, "Handbook of vacuum technology", John Wiley & Sons (2016).
- [74] J. F. O’Hanlon, "A user’s guide to vacuum technology", John Wiley & Sons (2005).

- [75] J. Léonard, M. Lee, A. Morales, T. M. Karg, T. Esslinger, and T. Donner, "Optical transport and manipulation of an ultracold atomic cloud using focus-tunable lenses", *New J. Phys.* **16**, 093028 (2014).
- [76] E. Wille, "Preparation of an optically trapped Fermi-Fermi mixture of  ${}^6\text{Li}$  and  ${}^{40}\text{K}$  atoms and characterization of the interspecies interactions by Feshbach spectroscopy", University of Innsbruck (2009).
- [77] J. Huckans, W. Dubosclard, E. Maréchal, O. Gorceix, B. Laburthe-Tolra, and M. Robert-de Saint-Vincent, "Reflectance of mirrors exposed to a strontium beam", arXiv: 1802.08499 (2018).
- [78] R. Grinham and A. Chew, "A review of outgassing and methods for its reduction", *Appl. sci. convergence technol.* **26**, 95 (2017).
- [79] Y. T. Sasaki, "A survey of vacuum material cleaning procedures: a subcommittee report of the American Vacuum Society Recommended Practices Committee", *J. Vac. Sci. Technol.* **9**, 2025 (1991).
- [80] D. Garton, "Vacuum technology and vacuum design handbook for accelerator technicians", (2011).
- [81] E. S. Turner, CAS CERN "Accelerator School vacuum technology", (1999).
- [82] The National Institute of Standards and Technology, : (NIST) <http://www.nist.gov/> (visited on 2019).
- [83] A. Arias, S. Helmrich, C. Schweiger, L. Ardizzone, G. Lohead, and S. Whitlock, "Versatile, high-power 460 nm laser system for Rydberg excitation of ultracold potassium", *Opt. Express* **25**, 14829 (2017).
- [84] N. Savage, "Optical parametric oscillators", *Nature Photonics* **4**, 124 (2010).
- [85] Y. Shimada, Y. Chida, N. Ohtsubo, T. Aoki, M. Takeuchi, T. Kuga, and Y. Torii, "A simplified 461-nm laser system using blue laser diodes and a hollow cathode lamp for laser cooling of Sr", *Rev. Sci. Instrum.* **84**, 063101 (2013).
- [86] T. Hosoya, M. Miranda, R. Inoue, and M. Kozuma, "Injection locking of a high power ultraviolet laser diode for laser cooling of ytterbium atoms", *Rev. Sci. Instrum.* **86**, 073110 (2015).
- [87] T. Pyragius, "Developing and building an absorption imaging system for ultracold atoms", arXiv: 1209.3408 (2012).
- [88] W. Ketterle, D. S. Durfee, and D. Stamper-Kurn, "Making, probing and understanding Bose-Einstein condensates", arXiv: cond-mat/9904034 (1999).

- [89] W. Ketterle and M. W. Zwierlein, "Making, probing and understanding ultracold Fermi gases", arXiv: 0801.2500 (2008).
- [90] C.-C. Chen, "An atomic marble run to unity phase-space density", Universiteit van Amsterdam (2019).
- [91] V. Schkolnik, O. Fartmann, and M. Krutzik, "An extended-cavity diode laser at 497 nm for laser cooling and trapping of neutral strontium", [Laser Physics 29, 035802 \(2019\)](#).
- [92] S. Stellmer and F. Schreck, "Reservoir spectroscopy of  $5s5p\ ^3P_2-5snd\ ^3D_{1,2,3}$  transitions in strontium", [Phys. Rev. A 90, 022512 \(2014\)](#).
- [93] J. M. Robinson, E. Oelker, W. R. Milner, W. Zhang, T. Legero, D. G. Matei, F. Riehle, U. Sterr, and J. Ye, "Crystalline optical cavity at 4K with thermal-noise-limited instability and ultralow drift", [Optica 6, 240 \(2019\)](#).
- [94] S. Stellmer, R. Grimm, and F. Schreck, "Production of quantum-degenerate strontium gases", [Phys. Rev. A 87, 013611 \(2013\)](#).
- [95] S. Stellmer, R. Grimm, and F. Schreck, "Detection and manipulation of nuclear spin states in fermionic strontium", [Phys. Rev. A 84, 043611 \(2011\)](#).
- [96] B. Ohayon and G. Ron, "New approaches in designing a Zeeman slower", [J. Instrum. 8, P02016 \(2013\)](#).
- [97] C. J. Dedman, J. Nes, T. M. Hanna, R. G. Dall, K. G. H. Baldwin, and A. G. Truscott, "Optimum design and construction of a Zeeman slower for use with a magneto-optic trap", [Rev. Sci. Instrum. 75, 5136 \(2004\)](#).
- [98] S. Aubin, M. H. T. Extavour, S. Myrskog, L. J. LeBlanc, J. Estève, S. Singh, P. Scrutton, D. McKay, R. McKenzie, I. D. Leroux, A. Stummer, and J. H. Thywissen, "Trapping fermionic  $^{40}\text{K}$  and bosonic  $^{87}\text{Rb}$  on a chip", [J. Low Temp. Phys. 140, 377 \(2005\)](#).
- [99] M. Extavour, "Fermions and bosons on an atom chip", University of Toronto (2009).
- [100] X. Xu, T. H. Loftus, J. W. Dunn, C. H. Greene, J. L. Hall, A. Gallagher, and J. Ye, "Single-stage sub-Doppler cooling of alkaline earth atoms", [Phys. Rev. Lett. 90, 193002 \(2003\)](#).
- [101] H. Katori, T. Ido, Y. Isoya, and M. Kuwata-Gonokami, "Magneto-optical trapping and cooling of strontium atoms down to the photon recoil temperature", [Phys. Rev. Lett. 82, 1116 \(1999\)](#).

- 
- [102] H. J. Metcalf and P. van der Straten, "Laser cooling and trapping of neutral atoms", Wiley Online Library (2007).
- [103] Y. Castin, H. Wallis, and J. Dalibard, "Limit of doppler cooling", *J. Opt. Soc. Am. B* **6**, 2046 (1989).
- [104] T. H. Loftus, T. Ido, A. D. Ludlow, M. M. Boyd, and J. Ye, "Narrow line cooling: finite photon recoil dynamics", *Phys. Rev. Lett.* **93**, 073003 (2004).
- [105] T. Chanelière, L. He, R. Kaiser, and D. Wilkowski, "Three dimensional cooling and trapping with a narrow line", *Eur. Phys. J. D* **46**, 507 (2008).
- [106] R. K. Hanley, P. Huillery, N. C. Keegan, A. D. Bounds, D. Boddy, R. Faoro, and M. P. A. Jones, "Quantitative simulation of a magneto-optical trap operating near the photon recoil limit", *J. Mod. Opt.* **65**, 667 (2018).
- [107] O. N. Prudnikov, R. Y. Il'enkov, A. V. Taichenachev, and V. I. Yudin, "Scaling law in laser cooling on narrow-line optical transitions", *Phys. Rev. A* **99**, 023427 (2019).
- [108] T. Mukaiyama, H. Katori, T. Ido, Y. Li, and M. Kuwata-Gonokami, "Recoil-limited laser cooling of  $^{87}\text{Sr}$  atoms near the Fermi temperature", *Phys. Rev. Lett.* **90**, 113002 (2003).
- [109] P Bouyer, P Lemonde, M. B. Dahan, A Michaud, C Salomon, and J Dalibard, "An atom trap relying on optical pumping", *EPL* **27**, 569 (1994).
- [110] J. A. Muniz, M. A. Norcia, J. R. Cline, and J. K. Thompson, "A robust narrow-line magneto-optical trap using adiabatic transfer", arXiv:1806.00838 (2018).
- [111] G.-B. Liao, K.-S. Wu, C.-Y. Shih, Y.-H. Cheng, L.-A. Sun, Y.-J. Lin, and M.-S. Chang, "Optimization of a crossed optical dipole trap for loading and confining laser-cooled atoms", *J. Opt. Soc. Am. B* **34**, 869 (2017).
- [112] S. Stringari, "Collective excitations of a trapped Bose-condensed gas", *Phys. Rev. Lett.* **77**, 2360 (1996).
- [113] F. Dalfovo, S. Giorgini, M. Guilleumas, L. Pitaevskii, and S. Stringari, "Collective and single-particle excitations of a trapped Bose gas", *Phys. Rev. A* **56**, 3840 (1997).
- [114] M.-O. Mewes, M. R. Andrews, N. J. van Druten, D. M. Kurn, D. S. Durfee, C. G. Townsend, and W. Ketterle, "Collective excitations of a Bose-Einstein condensate in a magnetic trap", *Phys. Rev. Lett.* **77**, 988 (1996).

- [115] S. Stellmer, B. Pasquiou, R. Grimm, and F. Schreck, “Laser cooling to quantum degeneracy”, *Phys. Rev. Lett.* **110**, 263003 (2013).
- [116] S. Stellmer, M. K. Tey, R. Grimm, and F. Schreck, “Bose-Einstein condensation of  $^{86}\text{Sr}$ ”, *Phys. Rev. A* **82**, 041602 (2010).
- [117] P. G. Mickelson, Y. N. Martinez de Escobar, M. Yan, B. J. DeSalvo, and T. C. Killian, “Bose-Einstein condensation of  $^{88}\text{Sr}$  through sympathetic cooling with  $^{87}\text{Sr}$ ”, *Phys. Rev. A* **81**, 051601 (2010).
- [118] E. A. Donley, N. R. Claussen, S. L. Cornish, J. L. Roberts, E. A. Cornell, and C. E. Wieman, “Dynamics of collapsing and exploding Bose-Einstein condensates”, *Nature* **412**, 295 (2001).
- [119] J Szczepkowski, R Gartman, M Witkowski, L Tracewski, M Zawada, and W Gawlik, “Analysis and calibration of absorptive images of Bose–Einstein condensate at nonzero temperatures”, *Rev. Sci. Instrum.* **80**, 053103 (2009).
- [120] U Ernst, J Schuster, F Schreck, A Marte, A Kuhn, and G Rempe, “Free expansion of a Bose-Einstein condensate from an Ioffe–Pritchard magnetic trap”, *Appl. Phys. B* **67**, 719 (1998).
- [121] Y. Kagan, E. L. Surkov, and G. V. Shlyapnikov, “Evolution of a Bose gas in anisotropic time-dependent traps”, *Phys. Rev. A* **55**, R18 (1997).
- [122] M. H. Anderson, J. R. Ensher, M. R. Matthews, C. E. Wieman, and E. A. Cornell, “Observation of Bose-Einstein condensation in a dilute atomic vapor”, *Science* **269**, 198 (1995).
- [123] M. Holland and J. Cooper, “Expansion of a Bose-Einstein condensate in a harmonic potential”, *Phys. Rev. A* **53**, R1954 (1996).
- [124] S. Giorgini, L. P. Pitaevskii, and S. Stringari, “Theory of ultracold atomic Fermi gases”, *Rev. Mod. Phys.* **80**, 1215 (2008).
- [125] A. V. Taichenachev, V. I. Yudin, C. W. Oates, C. W. Hoyt, Z. W. Barber, and L. Hollberg, “Magnetic field-induced spectroscopy of forbidden optical transitions with application to lattice-based optical atomic clocks”, *Phys. Rev. Lett.* **96**, 083001 (2006).
- [126] M. M. Boyd, T. Zelevinsky, A. D. Ludlow, S. Blatt, T. Zanon-Willette, S. M. Foreman, and J. Ye, “Nuclear spin effects in optical lattice clocks”, *Phys. Rev. A* **76**, 022510 (2007).

- [127] S. G. Porsev and A. Derevianko, “Hyperfine quenching of the metastable  $^3P_{0,2}$  states in divalent atoms”, *Phys. Rev. A* **69**, 042506 (2004).
- [128] B. DeMarco, “Quantum behavior of an atomic Fermi gas”, University of Colorado (2017).
- [129] A. D. Ludlow, M. M. Boyd, J. Ye, E. Peik, and P. O. Schmidt, “Optical atomic clocks”, *Rev. Mod. Phys.* **87**, 637 (2015).
- [130] M. J. Martin, M. Bishof, M. D. Swallows, X. Zhang, C. Benko, J. von Stecher, A. V. Gorshkov, A. M. Rey, and J. Ye, “A quantum many-body spin system in an optical lattice clock”, *Science* **341**, 632 (2013).
- [131] L. F. Livi, G. Cappellini, M. Diem, L. Franchi, C. Clivati, M. Frittelli, F. Levi, D. Calonico, J. Catani, M. Inguscio, and L. Fallani, “Synthetic dimensions and spin-orbit coupling with an optical clock transition”, *Phys. Rev. Lett.* **117**, 220401 (2016).
- [132] S. L. Bromley, S. Kolkowitz, T. Bothwell, D. Kedar, A. Safavi-Naini, M. L. Wall, C. Salomon, A. M. Rey, and J. Ye, “Dynamics of interacting fermions under spin-orbit coupling in an optical lattice clock”, *Nat. Phys.* **14**, 399 (2018).
- [133] N. R. Cooper and A. M. Rey, “Adiabatic control of atomic dressed states for transport and sensing”, *Phys. Rev. A* **92**, 021401 (2015).
- [134] J. P. Covey, I. S. Madjarov, A. Cooper, and M. Endres, “2000-times repeated imaging of strontium atoms in clock-magic tweezer arrays”, *Phys. Rev. Lett.* **122**, 173201 (2019).
- [135] K. Shibata, S. Kato, A. Yamaguchi, S. Uetake, and Y. Takahashi, “A scalable quantum computer with ultranarrow optical transition of ultracold neutral atoms in an optical lattice”, *Appl. Phys. B* **97**, 753 (2009).
- [136] A. V. Gorshkov, A. M. Rey, A. J. Daley, M. M. Boyd, J. Ye, P. Zoller, and M. D. Lukin, “Alkaline-earth-metal atoms as few-qubit quantum registers”, *Phys. Rev. Lett.* **102**, 110503 (2009).
- [137] N. Yu and M. Tinto, “Gravitational wave detection with single-laser atom interferometers”, *Gen. Relativ. Gravit.* **43**, 1943 (2011).
- [138] P. W. Graham, J. M. Hogan, M. A. Kasevich, and S. Rajendran, “New method for gravitational wave detection with atomic sensors”, *Phys. Rev. Lett.* **110**, 171102 (2013).

- [139] S. Kolkowitz, I. Pikovski, N. Langellier, M. D. Lukin, R. L. Walsworth, and J. Ye, “Gravitational wave detection with optical lattice atomic clocks”, *Phys. Rev. D* **94**, 124043 (2016).
- [140] S. Kato, K. Shibata, R. Yamamoto, Y. Yoshikawa, and Y. Takahashi, “Optical magnetic resonance imaging with an ultra-narrow optical transition”, *Appl. Phys. B* **108**, 31 (2012).
- [141] K. Shibata, R. Yamamoto, Y. Seki, and Y. Takahashi, “Optical spectral imaging of a single layer of a quantum gas with an ultranarrow optical transition”, *Phys. Rev. A* **89**, 031601 (2014).
- [142] N. Goldman, G. Juzeliunas, P. Ohberg, and I. B. Spielman, “Light-induced gauge fields for ultracold atoms”, *Rep. Prog. Phys.* **77**, 126401 (2014).
- [143] Y.-J. Lin, R. L. Compton, A. R. Perry, W. D. Phillips, J. V. Porto, and I. B. Spielman, “Bose-Einstein condensate in a uniform light-induced vector potential”, *Phys. Rev. Lett.* **102**, 130401 (2009).
- [144] B. Song, L. Zhang, C. He, T. F. J. Poon, E. Hajiyevev, S. Zhang, X.-J. Liu, and G.-B. Jo, “Observation of symmetry-protected topological band with ultracold fermions”, *Sci. Adv.* **4**, 123603 (2018).
- [145] F. Leroux, K. Pandey, R. Rehbi, F. Chevy, C. Miniatura, B. Grémaud, and D. Wilkowski, “Non-Abelian adiabatic geometric transformations in a cold strontium gas”, *Nat. Comm.* **9**, 3580 (2018).
- [146] F. Gerbier and J. Dalibard, “Gauge fields for ultracold atoms in optical superlattices”, *New J. Phys.* **12**, 033007 (2010).
- [147] S. Kato, S. Sugawa, K. Shibata, R. Yamamoto, and Y. Takahashi, “Control of resonant interaction between electronic ground and excited states”, *Phys. Rev. Lett.* **110**, 173201 (2013).
- [148] D. G. Green, C. L. Vaillant, M. D. Frye, M. Morita, and J. M. Hutson, “Quantum chaos in ultracold collisions between  $\text{Yb}(^1S_0)$  and  $\text{Yb}(^3P_2)$ ”, *Phys. Rev. A* **93**, 022703 (2016).
- [149] S. Taie, S. Watanabe, T. Ichinose, and Y. Takahashi, “Feshbach-resonance-enhanced coherent atom-molecule conversion with ultranarrow photoassociation resonance”, *Phys. Rev. Lett.* **116**, 043202 (2016).

- [150] Y. Takasu, Y. Fukushima, Y. Nakamura, and Y. Takahashi, “Magnetoassociation of a Feshbach molecule and spin-orbit interaction between the ground and electronically excited states”, *Phys. Rev. A* **96**, 023602 (2017).
- [151] A. Khramov, A. Hansen, W. Dowd, R. J. Roy, C. Makrides, A. Petrov, S. Kotochigova, and S. Gupta, “Ultracold heteronuclear mixture of ground and excited state atoms”, *Phys. Rev. Lett.* **112**, 033201 (2014).
- [152] H. Hara, H. Konishi, S. Nakajima, Y. Takasu, and Y. Takahashi, “A three-dimensional optical lattice of ytterbium and lithium atomic gas mixture”, *J. Phys. Soc. Jpn.* **83**, 014003 (2014).
- [153] W. Dowd, R. J. Roy, R. K. Shrestha, A. Petrov, C. Makrides, S. Kotochigova, and S. Gupta, “Magnetic field dependent interactions in an ultracold Li-Yb( $^3P_2$ ) mixture”, *New J. Phys.* **17**, 055007 (2015).
- [154] H. Konishi, F. Schaefer, S. Ueda, and Y. Takahashi, “Collisional stability of localized Yb( $^3P_2$ ) atoms immersed in a Fermi sea of Li”, *New J. Phys.* **18**, 103009 (2016).
- [155] M. L. Gonzalez-Martinez and J. M. Hutson, “Magnetically tunable Feshbach resonances in Li+Yb( $^3P_j$ )”, *Phys. Rev. A* **88**, 020701 (2013).
- [156] A. Petrov, C. Makrides, and S. Kotochigova, “Magnetic control of ultra-cold  $^6\text{Li}$  and  $^{174}\text{Yb}(^3P_2)$  atom mixtures with Feshbach resonances”, *New J. Phys.* **17**, 045010 (2015).
- [157] T. Chen, C. Zhang, X. Li, J. Qian, and Y. Wang, “Anisotropy induced Feshbach resonances in mixture of  $^6\text{Li}(^2S) + ^{171}\text{Yb}(^3P_2)$ ”, *New J. Phys.* **17**, 103036 (2015).
- [158] A. Derevianko, “Feasibility of cooling and trapping metastable alkaline-earth atoms”, *Phys. Rev. Lett.* **87**, 023002 (2001).
- [159] R. Santra, K. V. Christ, and C. H. Greene, “Properties of metastable alkaline-earth-metal atoms calculated using an accurate effective core potential”, *Phys. Rev. A* **69**, 042510 (2004).
- [160] S. G. Bhongale, L. Mathey, E. Zhao, S. F. Yelin, and M. Lemesko, “Quantum phases of quadrupolar Fermi gases in optical lattices”, *Phys. Rev. Lett.* **110**, 155301 (2013).

- [161] M. Lahrz, M. Leshko, K. Sengstock, C. Becker, and L. Mathey, “Detecting quadrupole interactions in ultracold Fermi gases”, *Phys. Rev. A* **89**, 043616 (2014).
- [162] W.-M. Huang, M. Lahrz, and L. Mathey, “Quantum phases of quadrupolar Fermi gases in coupled one-dimensional systems”, *Phys. Rev. A* **89**, 013604 (2014).
- [163] Y. Takasu, K. Maki, K. Komori, T. Takano, K. Honda, M. Kumakura, T. Yabuzaki, and Y. Takahashi, “Spin-singlet Bose-Einstein condensation of two-electron atoms”, *Phys. Rev. Lett.* **91**, 040404 (2003).
- [164] S. Kraft, F. Vogt, O. Appel, F. Riehle, and U. Sterr, “Bose-Einstein condensation of alkaline earth atoms:  $^{40}\text{Ca}$ ”, *Phys. Rev. Lett.* **103**, 130401 (2009).
- [165] S. Taie, R. Yamazaki, S. Sugawa, and Y. Takahashi, “An SU(6) Mott insulator of an atomic Fermi gas realized by large-spin Pomeranchuk cooling”, *Nat. Phys.* **8**, 825 (2012).
- [166] H. Ozawa, S. Taie, Y. Takasu, and Y. Takahashi, “Antiferromagnetic spin correlation of SU(N) Fermi gas in an optical superlattice”, *Phys. Rev. Lett.* **121**, 225303 (2018).
- [167] O. Boada, A. Celi, J. I. Latorre, and M. Lewenstein, “Quantum simulation of an extra dimension”, *Phys. Rev. Lett.* **108**, 133001 (2012).
- [168] H. Knockel and E. Tiemann, *Program IodineSpec5: Version for strontium quantum gas group University of Amsterdam feb. 2017*, Institute of Quantum Optics, Leibniz University, Hannover, Germany.
- [169] E. D. Black, “An introduction to Pound-Drever-Hall laser frequency stabilization”, *Am. J. Phys.* **69**, 79 (2001).
- [170] G. Ferrari, P. Cancio, R. Drullinger, G. Giusfredi, N. Poli, M. Prevedelli, C. Toninelli, and G. M. Tino, “Precision frequency measurement of visible intercombination lines of strontium”, *Phys. Rev. Lett.* **91**, 243002 (2003).
- [171] J. R. De Laeter et al., “Atomic weights of the elements. Review 2000 (IUPAC Technical Report)”, *Pure Appl. Chem.* **75**, 683 (2003).
- [172] T. W. Hänsch, I. S. Shahin, and A. L. Schawlow, “High-resolution saturation spectroscopy of the sodium *D* lines with a pulsed tunable dye laser”, *Phys. Rev. Lett.* **27**, 707 (1971).

- [173] Y.-C. Huang, H.-C. Chen, S.-E. Chen, J.-T. Shy, and L.-B. Wang, "Precise frequency measurements of iodine hyperfine transitions at 671 nm", *Appl. Opt.* **52**, 1448 (2013).
- [174] D. J. McCarron, S. A. King, and S. L. Cornish, "Modulation transfer spectroscopy in atomic rubidium", *Meas. Sci. Technol.* **19**, 105601 (2008).
- [175] A. Yamaguchi, "Metastable State of Ultracold and Quantum Degenerate Ytterbium Atoms: High-Resolution Spectroscopy and Cold Collisions", Kyoto University (2018).
- [176] J. E. Sansonetti and G. Nave, "Wavelengths, transition probabilities, and energy levels for the spectrum of neutral strontium (SrI)", *J. Phys. Chem. Ref. Data* **39**, 033103 (2010).
- [177] S. M. Heider and G. O. Brink, "Hyperfine structure of  $^{87}\text{Sr}$  in the  $^3P_2$  metastable state", *Phys. Rev. A* **16**, 1371 (1977).
- [178] D. Bender, H. Brand, and V. Pfeufer, "Isotope shifts in transitions between low-lying levels of Sr I by laser-atomic-beam spectroscopy", *Z. Phys* **318**, 291 (1984).
- [179] F. Buchinger, R. Coriveau, E. B. Ramsay, D. Berdichevsky, and D. W. L. Sprung, "Influence of the N=50 shell closure on mean square charge radii of strontium", *Phys. Rev. C* **32**, 2058 (1985).
- [180] T. Takano, R. Mizushima, and H. Katori, "Precise determination of the isotope shift of  $^{88}\text{Sr}$  -  $^{87}\text{Sr}$  optical lattice clock by sharing perturbations", *Appl. Phys. Express* **10**, 072801 (2017).
- [181] I. Courtillot, A. Quessada-Vial, A. Bruschi, D. Kolker, G. D. Rovera, and P. Lemonde, "Accurate spectroscopy of Sr atoms", *Eur. Phys. J. D* **33**, 161 (2005).
- [182] A Yamaguchi, S Uetake, S Kato, H Ito, and Y Takahashi, "High-resolution laser spectroscopy of a Bose-Einstein condensate using the ultranarrow magnetic quadrupole transition", *New J. Phys.* **12**, 103001 (2010).
- [183] S. Uetake, R. Murakami, J. M. Doyle, and Y. Takahashi, "Spin-dependent collision of ultracold metastable atoms", *Phys. Rev. A* **86**, 032712 (2012).
- [184] A. Dareau, M. Scholl, Q. Beaufils, D. Döring, J. Beugnon, and F. Gerbier, "Doppler spectroscopy of an ytterbium Bose-Einstein condensate on the clock transition", *Phys. Rev. A* **91**, 023626 (2015).

- [185] A. Kramida, Y. Ralchenko, J. Reader, and NIST ASD Team (2018), *Atomic Spectra Database (version 5.6.1)*, (NIST) <https://physics.nist.gov/asd> (visited on 10/23/2018).
- [186] I. Knottnerus, S. Pyatchenkov, O. Onishchenko, A. Urech, G. A. Siviloglou, and F. Schreck, "Microscope objective for imaging atomic strontium with 0.63 micrometer resolution", arXiv:1906.07167 (2019).
- [187] N. Schlosser, G. Reymond, I. Protsenko, and P. Grangier, "Sub-poissonian loading of single atoms in a microscopic dipole trap", *Nature* **411**, 1024 (2001).
- [188] Y. R. P. Sortais, H. Marion, C. Tuchendler, A. M. Lance, M. Lamare, P. Fournet, C. Armellin, R. Mercier, G. Messin, A. Browaeys, and P. Grangier, "Diffraction-limited optics for single-atom manipulation", *Phys. Rev. A* **75**, 013406 (2007).
- [189] W. S. Bakr, J. I. Gillen, A. Peng, S. Fölling, and M. Greiner, "A quantum gas microscope for detecting single atoms in a Hubbard-regime optical lattice", *Nature* **462**, 74 (2009).
- [190] L. W. Cheuk, M. A. Nichols, M. Okan, T. Gersdorf, V. V. Ramasesh, W. S. Bakr, T. Lompe, and M. W. Zwierlein, "Quantum-gas microscope for fermionic atoms", *Phys. Rev. Lett.* **114**, 193001 (2015).
- [191] I. Knottnerus, "Tweezer machine for Sr atoms using a homebuilt microscope objective from commercial lenses", University of Amsterdam (2018).
- [192] R. M. Parton and I. Davis, "Lifting the fog: image restoration by deconvolution", *Cell Biology (Third Edition)* (2006).
- [193] B. Zhang, J. Zerubia, and J.-C. Olivo-Marin, "Gaussian approximations of fluorescence microscope point-spread function models", *Appl. Opt.* **46**, 1819 (2007).
- [194] C.-C. Chen, S. Bennetts, R. González Escudero, F. Schreck, and B. Pasquiou, "Sisyphus optical lattice decelerator", *Phys. Rev. A* **100**, 023401 (2019).

